5-2007

Plastic Deformation and Annealing of Zr- and Cu- Based Bulk Metallic Glasses

Sujing Xie
University of Tennessee - Knoxville

To the Graduate Council:

I am submitting herewith a dissertation written by Sujing Xie entitled "Plastic Deformation and Annealing of Zr- and Cu- Based Bulk Metallic Glasses." I have examined the final electronic copy of this dissertation for form and content and recommend that it be accepted in partial fulfillment of the requirements for the degree of Doctor of Philosophy, with a major in Materials Science and Engineering.

Easo P. George, Major Professor

We have read this dissertation and recommend its acceptance:

George M. Pharr, James R. Morris, Dayakar Penumadu

Accepted for the Council:

Carolyn R. Hodges

Vice Provost and Dean of the Graduate School

(Original signatures are on file with official student records.)

To the Graduate Council:

I am submitting herewith a dissertation written by Sujing Xie entitled “Plastic deformation and annealing of Zr- and Cu-based metallic glasses”. I have examined the final electronic copy of this dissertation for form and content and recommend that it be accepted in partial fulfillment of the requirements for the degree of Doctor of Philosophy, with a major in Materials Science and Engineering.

Easo P. George
Major Professor

We have read this dissertation
and recommend its acceptance:

George M. Pharr

James R. Morris

Dayakar Penumadu

Accepted for the Council:

Carolyn Hodges
Dean of the Graduate School

(Original signatures are on file with official student records.)

Plastic Deformation and Annealing of Zr- and Cu-Based Bulk Metallic Glasses

A dissertation
Presented for the
Doctor of Philosophy Degree
The University of Tennessee, Knoxville

Sujing Xie

May 2007

DEDICATION

This dissertation is dedicated to my parents, Congzheng Xie and Huaxiu Li, great role models, my husband, Ming Zhang, and the rest of my families, for always believing in and encouraging me.

ACKNOWLEDGMENT

I would like to express my sincere appreciation to my advisor Prof. Easo P. George for his scientific guidance, patience and kindness throughout my Ph.D. study and completion of this dissertation. The encouragement and precious opportunities he gave me helped me to develop my academic capabilities. I would also like to thank my committee members Dr. George M. Pharr, Dr. James R. Morris, and Dr. Dayakar Penumadu for their constructive advice and enormous support. All of them, with their wisdom, experience and kindness, have been and will always be great mentors to me.

I am grateful to the staff members in the Department of Materials Science and Engineering, The University of Tennessee, Knoxville, and the Materials Science and Technology Division, Oak Ridge National Laboratory for the wonderful time we spent together.

I want to thank my parents and husband most. They have always been giving me love and encouragement throughout all these years. I am grateful to the support from my family and all my friends.

This research was sponsored by the Division of Materials Science and Engineering, Office of Basic Energy Sciences, U.S. Department of Energy under contract DE-AC05-00OR22725 with UT-Battelle, LLC.

ABSTRACT

Plastic deformation in crystalline metals occurs by the motion and multiplication of lattice defects called dislocations, resulting in strain hardening. Metallic glasses, in contrast, lack long-range order; therefore, dislocation-mediated plasticity is not possible in these materials. Metallic glasses undergo plastic deformation through the nucleation and propagation of defects called shear bands, which cause strain softening.

This strain softening can be recovered after annealing, i.e., annealing makes the plastically strained metallic glasses harder, in sharp contrast to the annealing-induced softening typically observed in crystalline metals. During annealing, hardness initially recovers more rapidly in heavily deformed specimens than in lightly deformed ones, at a rate that varies inversely as the shear band spacing. With increasing annealing time and temperature, hardness further increases, at the same rate whether pre-strained or not. If the deformed and annealed metallic glass is plastically deformed again, reversible softening is observed. To our knowledge, this is the first time that such reversible softening in metallic glasses has been reported.

These hardness changes were correlated with shear band patterns around/underneath a Vickers indent. Shear bands produced during indentation of as-cast glass were semi-circular and radial, consistent with the maximum stress distribution beneath the indenter. In contrast, shear bands in the pre-strained glass were irregular and convoluted, and appeared to be a mixture of shear bands produced during the preceding compression and those in as-cast glass. This indicates that shear band regions are softer than the surrounding undeformed matrix and act as preferred sites for subsequent deformation during indentation, consistent with the macroscopic strain softening

observed after plastic deformation. After annealing, shear bands tend to recover the originally semi-circular and radial shapes associated with the hardness increase.

TABLE OF CONTENTS

Chapter **Page**

List of Tables

Table **Page**

List of Figures

Figure **Page**

1 INTRODUCTION

Metallic glasses lack the long-range atomic order of conventional crystalline metals and have attracted much attention in the past decades due to their unique properties such as high strength, elastic limit (~ 2%), fracture toughness, and corrosion resistance (*1-4*). However, the high strength of metallic glasses is often accompanied by remarkably little plastic deformation (< 2%) at temperatures much lower than the glass transition temperature (T_g). The available experimental results show that metallic glasses undergo plastic deformation through the nucleation and propagation of shear bands (*5*). In uniaxial tension and compression, once a few shear bands are formed, plastic deformation remains highly localized in these bands, which prevents the generation of new shear bands and makes the existing shear bands rapidly propagate through the samples, resulting in catastrophic failure (*5-7*). In contrast, plastic deformation of crystalline metals occurs by formation and movement of dislocations: barriers to dislocation motion cause the deformed regions to become harder than the undeformed regions (i.e. strain hardening), which makes plastic deformation spread to the softer regions, and finally throughout the whole sample, i.e., homogeneous deformation (*8*).

The difficulties in obtaining plastic deformation at temperatures much lower than the glass transition temperature (T_g), limit our understanding of deformation mechanisms in bulk metallic glasses. Therefore, it is important to find methods to plastically deform metallic glasses without failure.

1.1 Plastic deformation of metallic glasses

As is well known, monolithic metallic glasses exhibit limited plastic deformation under conventional tensile and compressive conditions. However, under certain constrained conditions such as bending, indenting and rolling, greater amounts of plastic deformation can be obtained in metallic glasses. In all these cases, shear band propagation is constrained by the surrounding less severely deformed material or the contact roller, which activates the generation of multiple new shear bands to accommodate plastic deformation.

1.1.1 Bending induced plastic deformation in metallic glasses

Since Ast and Krenisky (*9*) found that thin $Fe_{40}Ni_{40}P_{14}B_6$ metallic glass ribbons could be deformed as an ideal elastic-plastic solid in 1980, bending ductility has been widely observed (*10-12*). Zielinski and Ast observed multiple shear bands on the bent $Ni_{75}Si_8B_{17}$ wires, in contrast to a single shear band during uniaxial tension. Recently, Conner et al.(*11, 12*) also clearly observed multiple shear bands on both the inside (compression) and outside (tension) surfaces of a bent $Zr_{57}Cu_{15.4}Ni_{12.6}Al_{10}Nb_5$ thin plate, with the bands stopping at the neutral axis in the center, as shown in Figure 1-1. Therefore, the ductility observed during bending is related to the existence of a zero-stress region in the center, which makes it possible to form multiple shear bands to accommodate the plastic strain.

Inoue et al. (*13*) found that significant bending ductility can be obtained only if the sample size is below a critical value. Conner et al. (*11, 12*) reported a strong dependence of plastic strain to failure on sample size (thickness of plates or

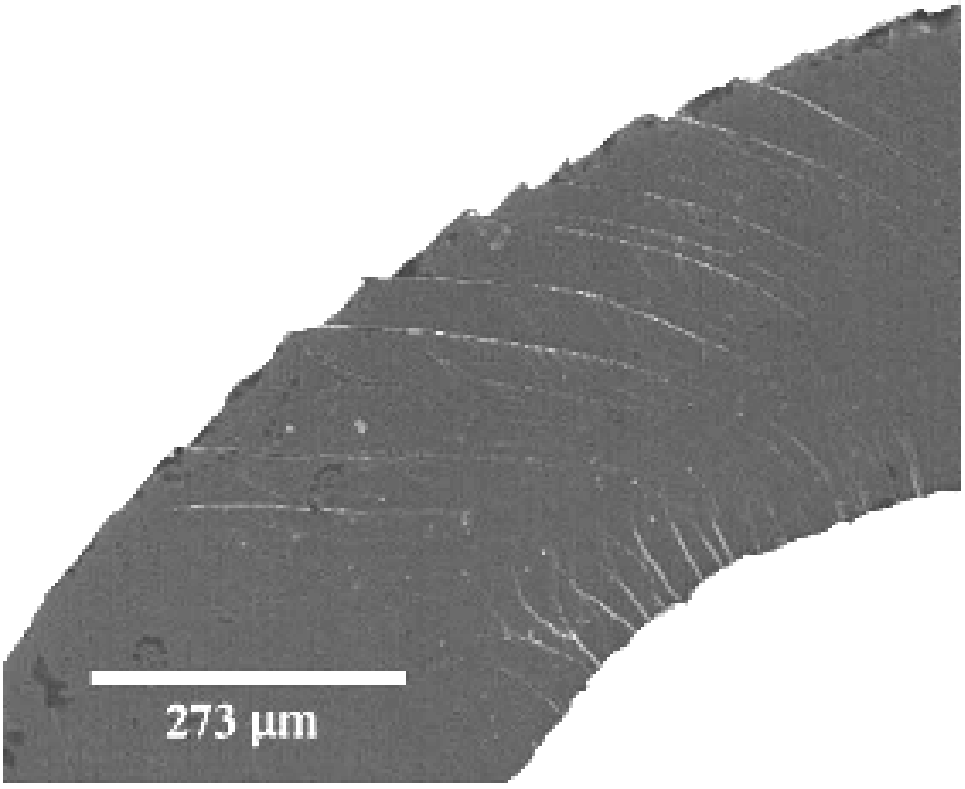

Figure 1-1.SEM image showing shear bands in 0.58 mm thick melt-spun ribbon of Vitreloy 106 bent over a mandrel with a radius of 1mm (*11, 12*).

diameter of wires), i.e., the fracture strain increases with decreasing sample size below a thickness of ~ 1mm and varies approximately inversely with sample size, as shown in Figure 1-2. It was also noticed that shear band spacing increases linearly with sample size, which means a higher shear band density, and therefore, a larger plastic strain to failure, in thinner samples.

So the question is whether plastic strain can be obtained only in thin ribbons and wires, or whether it can also be obtained in thicker (> 1mm) metallic glasses.

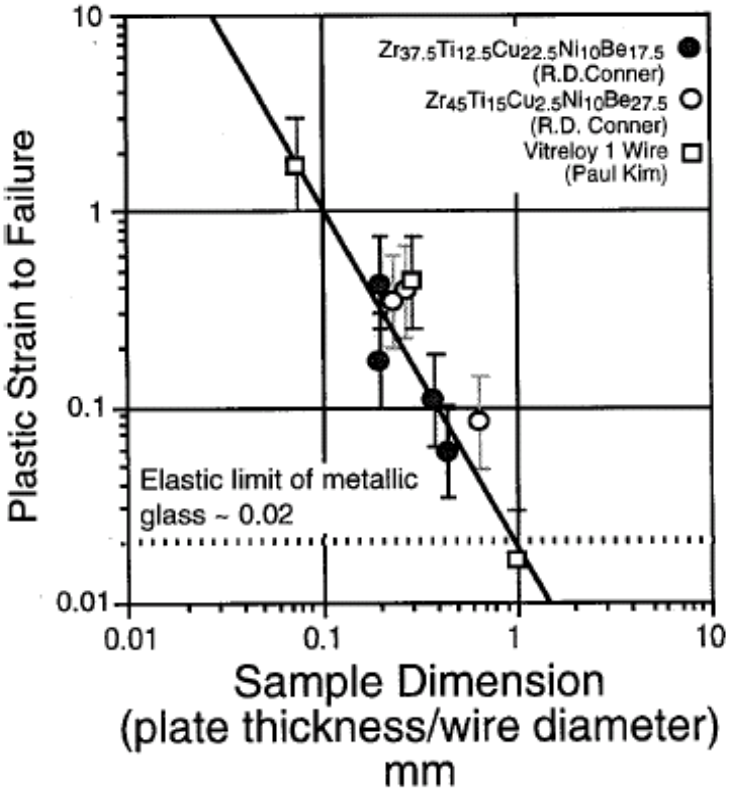

Figure 1-2. Bending fracture strain vs. sample dimension for various metallic glasses (*11, 12*).

1.1.2 Indentation induced plastic deformation in metallic glasses

Indentation tests can locally confine plastic deformation by the surrounding elastic material, and is therefore, another way to study plastic flow in metallic glasses. Since the 1970s, Vickers indenter has been used to study the mechanical behavior of metallic glasses (*14, 15*). With the development of displacement sensing indentation techniques as well as high-resolution surface characterization techniques (e.g. atomic force microscope), the indentation behavior of metallic glasses has been investigated in more detail. For example, a few small and isolated pop-in events in the indentation loading curves were observed by Wang et al. in a Zr-based glass (*16*), and pop-in events have since been identified in other metallic glasses (*17-21*) [as shown in Figure 1-3], although their density and character vary from alloy to alloy. Pile-ups and shear bands were also widely observed around the perimeters of Vickers, Berkovich (*22-24*) and spherical (*15, 25*) indents. The appearance of shear bands is assumed to be related to pop-in events in the $P-h$ curve given the inhomogeneous deformation in metallic glasses, but the exact correspondence between them is lacking.

The plastic deformation underneath the indents was also studied and first reported by Donovan (*15*) in $Pd_{40}Ni_{40}P_{20}$ metallic glass, with samples prepared by cutting the specimens as sections perpendicular to the original surface followed by polishing and etching. Due to the preferred etching of shear bands, the plastic zone and shear band morphology were observed, which was mainly characterized by radial incipient cracks and curved Hartmann lines. Recently, researchers began to study the plastic deformation underneath the indents again (*26-29*), using the bonded interface technique. Several sets of shear bands underneath a Vickers indent were

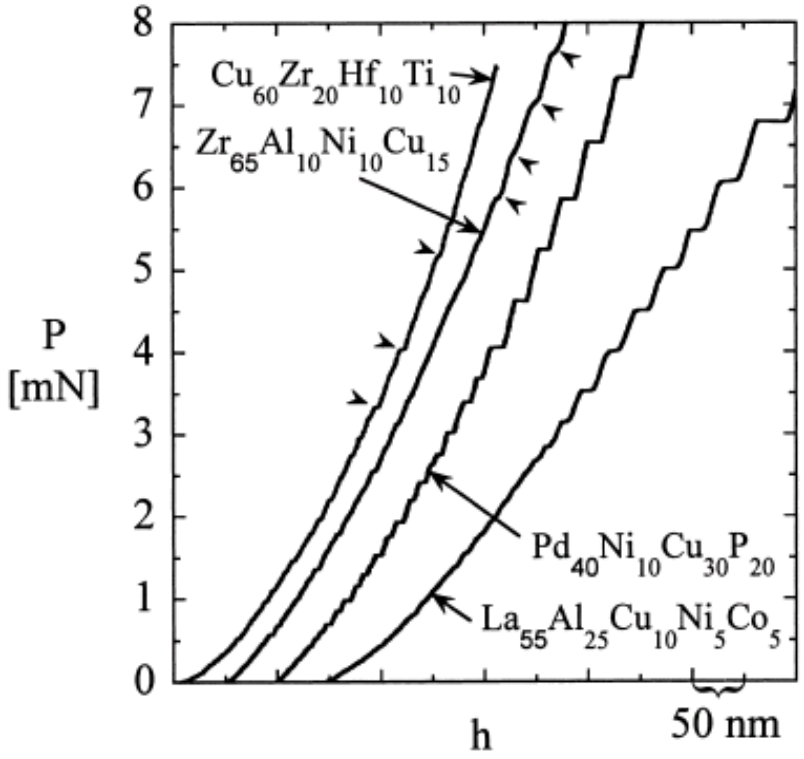

Figure 1-3. Indentation loading (P-h) curves for a variety of metallic glasses (*17-21*).

observed, with the radial bands akin to the slip-line field patterns in plasticity theory, as shown in Figure 1-4 (*26*). However, the large semi-circular slip-steps observed in experiments cannot be predicted by the slip-line theory. This limitation may be due to the complex stress state underneath the indent as opposed to the plane-strain condition presumed in the slip-line theory and the presence of a free top surface and the discontinuous interface between the two halves. Due to the limitation of slip-line theory in interpreting shear band patterns underneath the indent, Ramamurty et al. (*27*) and Zhang et al. (*28*) proposed to use the expanding cavity model to characterize the plastic deformation beneath the Vickers indent. They found that the semi-circular shear bands and the hemispherical plastic zone shape [Figure 1-5], as well as the square root relation between plastic zone size and indentation load are consistent with the prediction of the expanding cavity model. However, the appearance of secondary and tertiary radial bands was still difficult to explain due to the complex stress states at the bonded interface. In contrast to previous studies, Su and Anand (*29*) used a cylindrical indenter tip to conduct plane strain indentation on a Zr-based metallic glass. Nearly symmetrical spiral shear bands were observed, which was consistent with the results of finite element numerical simulation.

Plastic deformation induced by indentation is limited to small regions (e.g. ~ 45 μm at a load of 1000gf), and it is difficult to control the plastic strain. So the question remains whether it is possible to obtain severe plastic deformation throughout the whole bulk-metallic-glass specimen (thickness > 1mm) and control the amount of plastic deformation. The achievement of severe plastic deformation would make it possible to better understand deformation mechanisms in metallic glasses.

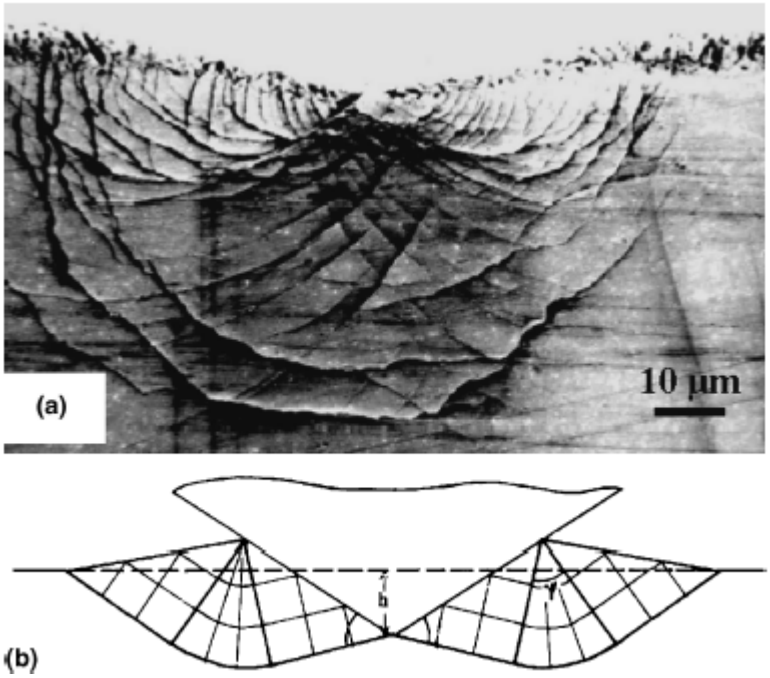

Figure 1-4. (a) The plastic flow beneath a sharp indenter in a Zr-based glass, observed using the bonded interface technique, (b) the expected plastic flow pattern from slip-line field theory for a perfectly plastic material deforming on the planes of maximum shear, in plane-strain mode beneath a wedge indenter (*26*).

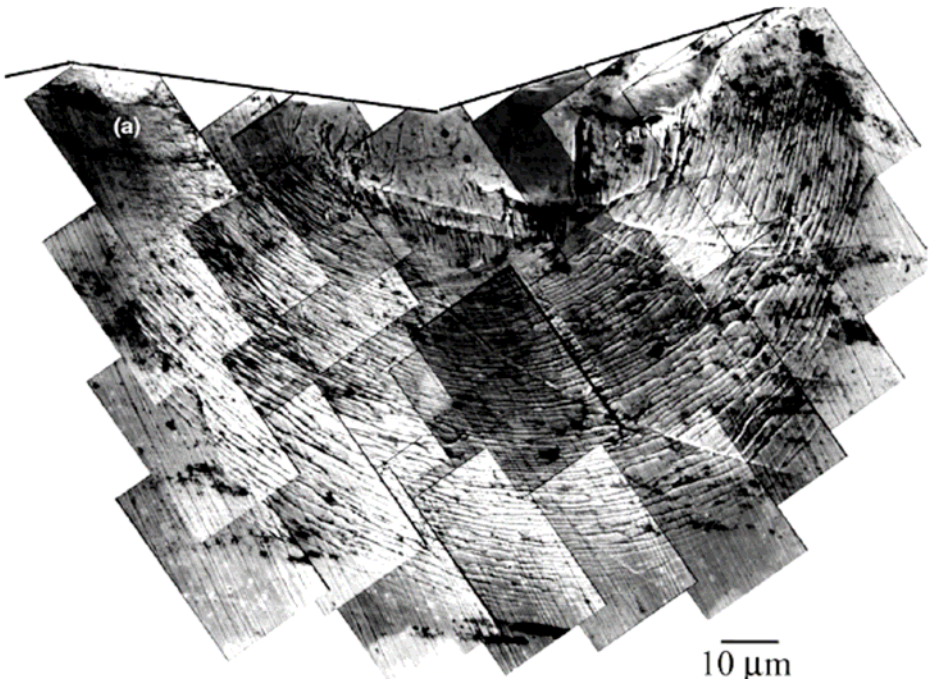

Figure 1-5. Plan view of SEM image from the subsurface deformation zone in as-cast $Pd_{40}Ni_{40}P_{20}$ glass indented with a Vickers indenter ($P = 5000g$), observed using the bonded interface technique, highlighting the shear band morphology underneath the indenter (*27*).

1.1.3 Cold rolling of metallic glasses

In the 1970s, several researchers found that plastic deformation in metallic glasses could be obtained by cold rolling. For example, in thin glassy ribbons (~50 μm), Chen (*30-32*) achieved ~ 40% thickness reduction in $Pd_{77.5}Cu_6Si_{16.5}$, and ~ 25% in $Ni_{75}P_{16}B_6Al_3$ and $Fe_{75}P_{16}Si_6Al_3$. Since then, cold rolling has been used to obtain plastic deformation in other thin (~50 μm) amorphous ribbons such as $Fe_{74}Co_{10}B_{16}$ (*33*), $Cu_{50}Zr_{50}$ (*34*), $Ti_{45}Zr_{16}Cu_{10}Ni_9$ (*35*), $Al_{88}Y_7Fe_5$ (*36*), $Al_{86.8}Ni_{3.7}Y_{9.5}$ (*37*), $Ni_{36}Fe_{32}Cr_{14}P_{12}B_6$ and $Ni_{40}Fe_{40}P_{14}B_6$ (*38*). Even if at cryogenic temperatures (150K), up to 97% reduction in thickness could be in $Cu_{60}Zr_{20}Ti_{20}$ metallic glass. Recently, plastic deformation by cold rolling has also been obtained in $Zr_{50}Cu_{30}Ni_{10}Al_{10}$ (*39*) and $Zr_{41.2}Ti_{13.8}Cu_{12.5}$ $Ni_{10}Be_{22.5}$ (*40*) amorphous plates with a thickness of 4 ~ 5mm. Multiple shear bands were observed on the side surfaces of the cold rolled metallic glass and the number of shear bands increased with increasing thickness reduction.

1.2 Effect of plastic deformation on metallic glasses

The attainment of a certain amount of plastic strain by constrained deformation makes it possible for us to study the responses of metallic glasses to plastic deformation. As is well known, dislocations nucleate and multiply during the plastic deformation of crystalline metals, which makes crystalline metals stronger and harder. However, there is no long-range ordering, therefore, no dislocations to accommodate the plastic deformation in metallic glasses. What happens within metallic glasses when they are deformed? In the following section, the currently available results on changes in the structural and mechanical properties of deformed metallic glasses are reviewed.

1.2.1 Structural changes associated with plastic deformation

Several different techniques have been used to characterize the structural changes induced by plastic deformation in metallic glasses. For example, Chen (*31*) first utilized DSC to investigate the stored energy in the glassy state, and found that the total stored energy increased linearly with cold rolling strain, as show in Figure 1-6. He proposed that the volume near a shear band is locally heated to T_g or above during plastic flow and then quenched to room temperature immediately after deformation. This would lead to a "frozen-in" structure within the shear bands similar to that in rapidly quenched glass. In agreement with Chen's DSC results, Stergioudis et al. (*34*) showed that the energy released from deformed $Cu_{50}Zr_{50}$ specimens was larger than that from non-deformed ones. Akhtar et al. (*33*) reported that the released energy in the 20% cold rolled $Fe_{74}Co_{10}B_{16}$ alloy was more than 8 times of the as-quenched one. Jin et al. (*41*) reported a drastic reduction of T_g induced by shear in a $Zr_{46.75}Ti_{8.25}Cu_{7.5}Ni_{10}Be_{27.5}$ bulk metallic glass, which was attributed to a large activation volume of relaxation under shear stress. Kulik (*42*) found a plastic deformation-caused decrease in the crystallization temperature, indicative of the destabilizing effect of plastic deformation. The structure change caused by plastic deformation, involves an increase in its disorder, i.e. a destruction of short-range order similar to that found in crystalline materials. The deformation induced structural disordering is consistent with the studies on the diffusion coefficient and stress relaxation in metallic glasses: the more the structure of a given glass departs from a fully relaxed structure, the higher the diffusion coefficient (*43-46*).

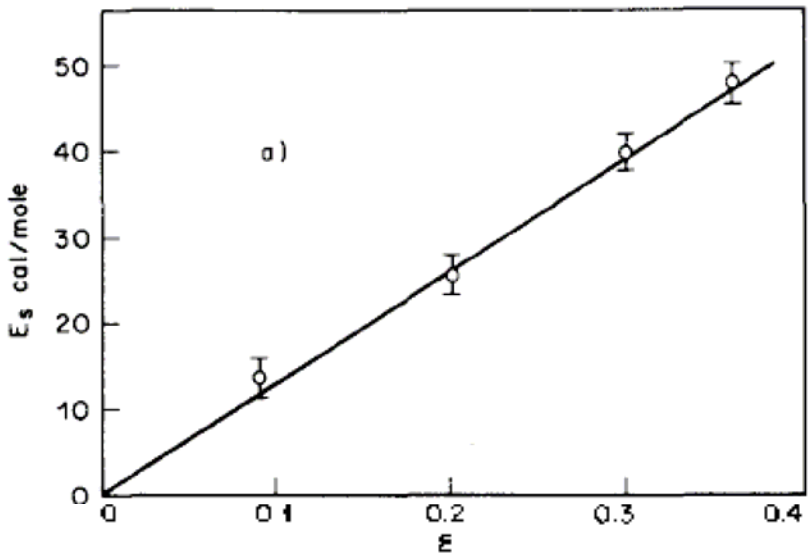

Figure 1-6. Stored energy E_s versus the plastic strain in $Pd_{77.5}Cu_6Si_{16.5}$ glass (*31*).

Optical microscope examination of plastically deformed specimen found that shear bands were susceptible to preferential etching (*47*) [Figure 1-7(a)]. A similar preferential etching of shear bands was also observed using TEM [Figure 1-7(b)] (*37, 48*), indicative of a structure change within these bands. However, what kind of structural change or disordering occurs in deformed specimens or in deformation induced shear bands is still unknown.

Chen and Chuang (*32*) studied the structure of cold rolled $Pd_{77.5}Cu_6Si_{16.5}$ metallic glass using positron annihilation methods. Based on the slight change in both the positron lifetime and angular correlation of the glass upon cold rolling, they concluded that cold rolling of the metallic glass induces no vacancy-like defects, and that plastic deformation in metallic glasses is accompanied by atomic regroupings somewhat analogous to the viscous flow of liquids. In contrast to this conclusion, Flores et al. (*49*), using position annihilation spectroscopy technique, observed a slight increase in free volume associated with plastic strain (plastic strain was obtained by making an array of Vickers indents on the sample surface), indicative of an increase in open volume positron annihilation sites. A similar free volume increase was also observed in cold-rolled Cu- and Zr-based metallic glasses, consistent with the differential scanning calorimetry (DSC) results which showed that the deformed glass exhibited structural relaxation at a lower temperature, and had a higher initial free volume (*50*). Hajlaoui et al. (*51*), using synchrotron diffraction technique, detected up to 37% free volume increase in $Zr_{65}Ni_{10}Cu_{15}Al_{10}$ sample with ball indents. In addition, the mass density measurement showed that 30 ~ 40% rolling led to a density reduction of ~ 0.14% in Pd-based metallic

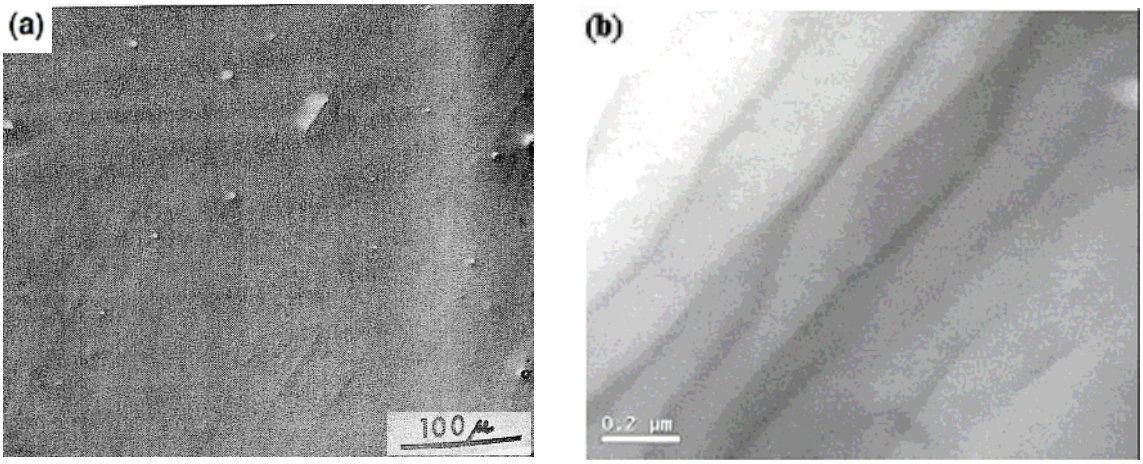

Figure 1-7. Selective etching of shear bands (a) optical microscopic image (*47*), and (b) TEM image (*37, 48*).

glasses (*52*). Similar density changes were observed by several other researchers (*53-55*). These results all indicate the presence of increased open volume in the plastically deformed glass.

Recently, Wright et al. (*56*) investigated the possibility of void nucleation from the coalescence of excess free volume during deformation of metallic glasses using free energy calculations, and found that any free volume generated in the shear band during deformation is unstable. They predicted that voids form spontaneously from the coalescence of free volume. Li et al. (*48*), using a quantitative high-resolution TEM method, studied shear bands in bulk Zr-based metallic glasses and found that they contained a higher concentration of nanometer-scale voids than undeformed regions. Jiang et al. (*37*) also found a great number of nanovoids in the interior of shear bands in cold rolled glassy ribbons, in agreement with the free energy calculation.

In contrast to the above results of increased free volume or short-range disordering in deformed metallic glasses, Chen et al. (*57*) found nanocrystals within the shear bands of some Al-based metallic glasses after bending. A similar nanocrystallization was also observed using TEM and X-ray diffraction in $Al_{90}Fe_5Gd_5$ amorphous ribbons after ball milling, however, no such ball milling-induced crystallization appeared in other metallic glasses, indicating that the mechanical deformation-induced structural changes may be sensitive to the chemical composition and thus the atomic structure and the bonding nature of the metallic glasses (*58*). Since then, several researchers have claimed to observe similar plastic deformation-induced crystallization in metallic glasses. For instance, Kim et al. (*59*) reported nanoindentation induced nanocrystallization in a Zr-based metallic glass, using TEM technique. Saida et

al. (*60*) reported compressive deformation-induced nanocrystallization in multistep shear bands of the $Zr_{65}Al_{7.5}Ni_{10}Pd_{17.5}$ metallic glass. Boucharat et al. (*36*) observed nanocrystals in both cold rolled and high pressure torsion-strained amorphous $Al_{88}Y_7Fe_5$ alloys: nanocrystals were observed predominantly within the shear bands or in the amorphous matrix surrounding the shear bands after cold rolling, whereas a homogeneous dispersion of nanocrystals at an extremely high number density were observed after high pressure torsion-straining. In contrast, Krishnanand and Cahn (*61*) did not observe any signs of crystallization in 30% cold rolled Ni/Nb alloy glass. Similarly, no crystallization was observed in the $Cu_{60}Zr_{20}Ti_{20}$ metallic glass severely rolled at cryogenic temperature, but phase separation was triggered by severe plastic deformation (up to 97% reduction in thickness) (*62*).

1.2.2 Mechanical property changes associated with plastic deformation

Besides the observed structural changes, a few investigations have reported on the effect of deformation on mechanical properties of metallic glasses. In the 1970s, Chen (*30*) found that cold rolling caused the Young's modulus of metallic glasses ($Pd_{77.5}Cu_6Si_{16.5}$, $Ni_{75}P_{16}B_6Al_3$, and $Fe_{15}P_{16}Si_6Al_3$) at room temperature to decrease by 1 ~ 2% upon ~ 30% reduction in thickness. Harms et al. (*53*) found that plastic deformation below the glass transition temperature reduced the shear modulus of glassy $Pd_{40}Ni_{10}Cu_{30}P_{20}$.

Due to the highly localized plastic deformation in shear bands, it is generally believed that strain induced softening occurs in metallic glasses. Unfortunately, it is not easy to verify this because it is difficult to measure hardness directly on narrow shear bands (even by nanoindentation). Furthermore, to make accurate measurements, the

surface steps associated with shear bands have to be removed by polishing to create a flat surface. Once that is done, the shear bands are erased and it becomes difficult to determine the location of a hardness indent relative to a shear band. There are only a few papers in the literature dealing with deformation-induced softening of metallic glasses. The first is a review paper by Masumoto and Maddin (*44*) where unpublished results of Masumoto and Koiwa are reported that show a decrease in the hardness of an amorphous $Pd_{80}Si_{20}$ ribbon after 40% reduction in thickness by cold rolling. The next is a paper by Tang et al. (*63*) in which the hardness of a Zr-based BMG was measured by nanoindentation after it had been indented with a 200-μm sphere. Hardness was reported to be lower near the spherical indent, where shear bands were present, than far away in the undeformed glass. However, since the surface was not polished after spherical indentation, the subsequent nanoindentation measurements may have been influenced by the presence of surface steps at shear bands. The last paper is that of Jiang et al. (*37*)who showed that the hardness of a 22-μm-thick Al-Ni-Y amorphous ribbon decreased from 3.89 to 3.48 GPa after cold rolling reduced its thickness by 45.5%.

However, none of these investigations systematically studied the relation between plastic strain and degree of softening perhaps due to the difficulties in controlling the amount of plastic strain in metallic glasses. Therefore, one purpose of our work is to provide direct experimental evidence showing the deformation-induced softening and to explore the relation between plastic strain and degree of softening.

1.3 Deformation mechanisms of metallic glasses

There exist two main theories to describe the deformation mechanisms of metallic

glasses. (I) Speapen proposed a theory based on the free volume created by external stress and its annihilation by diffusion (*64*), which was further modified by Steif and coworkers to analyze shear localization in metallic glasses (*65*). (II) Argon developed a model based on the idealization of two deformation modes, namely diffuse shear transformation and dislocation loop formation, to analyze the boundary between homogeneous and inhomogeneous flow of Pd-Si metallic glass (*66-68*). Speapen's free volume based theory seems to be more widely cited to interpret the deformation behavior of metallic glasses.

1.3.1 Free volume model

In the free volume model (*64*), it is assumed that macroscopic flow occurs as a result of a number of individual atomic jumps, as illustrated in Figure 1-8(a). In order for an atom to jump, it must have a favorable nearest neighbor environment, i.e., there must be open volume big enough to accommodate the atomic volume, υ^*. It is reasonable to assume that the atomic positions before and after a jump are relatively stable, i.e., they are at local energy minima. To make the atom jump, there must be some activation energy. If no external stress is present, the activation energies for atoms to jump forward and backward are provided by the thermal fluctuation, as shown in Figure 1-8(b); therefore, the activation energies and the number of atoms crossing the energy barriers in the two directions are the same. This is the basic microscopic mechanism for diffusion. When an external stress (τ) is applied, the activation energy for jumping along the stress direction will be lower [Figure 1-8(c)], which causes the number of atoms jumping along that direction (forward) to be larger than the number jumping backward. This results in a net forward atomic flow and forms the basic mechanism of flow. The quantitative description

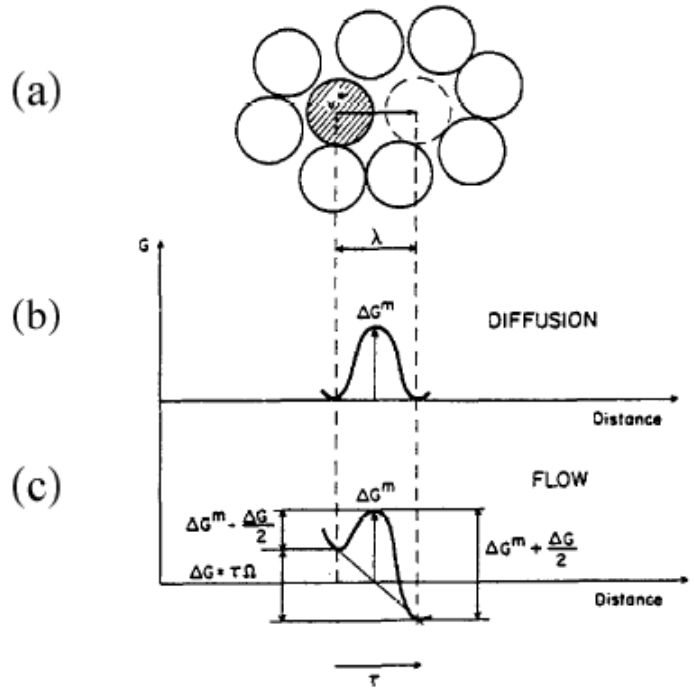

Figure 1-8. Illustration of an individual atomic jump, the basic step for macroscopic diffusion and flow.

is as follows.

The shear strain rate $\dot{\gamma}$ = fraction of atoms that make forward jumps per second

$$= \begin{array}{l}(\text{fraction of potential jump sites}) \times \\ (\text{net number of forward jumps on the potential jump sites per sec})\end{array} \quad (1\text{-}1).$$

The fraction of potential jump sites is calculated by the free volume theory of Turnbull and Cohen (*71*). The free volume of an atom is defined as that part of its nearest neighbor cage in which an atom can move around without an energy change. In Cohen and Turnbull's (*71*) theory, the probability to find a free volume between υ and υ+dυ is given by:

$$p(\upsilon)d\upsilon = \frac{\gamma}{\upsilon_f}\exp(-\frac{\gamma\upsilon}{\upsilon_f})d\upsilon \quad (1\text{-}2),$$

Where γ is a geometrical factor between 1 and ½, and υ_f is the average free volume of an atom. In order for an atom to jump, its free volume should be larger than the atomic size, υ^*. The probability that an atom is located on a potential jump site is

$$\int_{\upsilon^*}^{\infty}\frac{\gamma}{\upsilon_f}\exp(-\frac{\gamma\upsilon}{\upsilon_f})d\upsilon = \exp(-\frac{\gamma\upsilon^*}{\upsilon_f}) \quad (1\text{-}3).$$

It is also necessary to include a factor Δf, the fraction of the sample volume in which potential jump sites can be found. In homogeneous flow, the total volume contributes to flow, i.e., $\Delta f = 1$; in inhomogeneous flow, everything happens in a few very thin bands, and $\Delta f \le 1$. Therefore, the fraction of potential jump sites is

$$\Delta f \exp\left(-\frac{\gamma\upsilon^*}{\upsilon_f}\right) \quad (1\text{-}4).$$

The net number of forward jumps on the potential jump sites per second is

$$\nu\left[\exp\left(-\frac{\Delta G^m-\tau\Omega/2}{kT}\right)-\exp\left(-\frac{\Delta G^m+\tau\Omega/2}{kT}\right)\right] \qquad (1\text{-}5).$$

where ν is the frequency of atomic vibration (~ Debye frequency); ΔG^m is the activation energy required for an atom to overcome the barrier; Ω is the atomic volume; k is Boltzmann and T is absolute temperature. Substituting (1-4) and (1-5) into 1-1) gives

$$\dot{\gamma}=\Delta f\exp\left(-\frac{\gamma\upsilon^*}{\upsilon_f}\right)2\nu\sinh\left(\frac{\tau\Omega}{2kT}\right)\exp\left(-\frac{\Delta G^m}{kT}\right) \qquad (1\text{-}6).$$

During inhomogeneous flow, the material in the shear bands undergoes some structural change that leads to a local lowering of the viscosity. Polk and Turnbull (*72*) proposed that the structural change is the result of competition between two processes: a shear-induced disordering and diffusion-induced reordering. In Spaepen's free volume model, the free volume was chosen as the order parameter. Therefore, if there is a local lower viscosity in shear bands, there must be an increase of free volume. The two competing processes can be expressed as the creation of extra free volume induced by the external stress, and the annihilation of extra free volume by diffusion.

The amount of free volume created per second was expressed as:

$$\Delta^+\upsilon_f=\frac{\gamma\upsilon^*}{\upsilon_f}\frac{2kT}{S}\left[\cosh\left(\frac{\tau\Omega}{2kT}\right)-1\right]N\nu\exp\left(-\frac{\Delta G^m}{kT}\right)\exp\left(-\frac{\gamma\upsilon^*}{\upsilon_f}\right) \qquad (1\text{-}7),$$

where N is the total number of atoms and $S=\frac{2}{3}\mu\frac{1+\upsilon_p}{1-\upsilon_p}$ (μ is shear modulus and υ_p is Poisson's ratio). The amount of free volume annihilated per second was expressed as,

$$\Delta^-\upsilon_f=\frac{\upsilon^*}{n_D}N\nu\exp\left(-\frac{\Delta G^m}{kT}\right)\exp\left(-\frac{\gamma\upsilon^*}{\upsilon_f}\right) \qquad (1\text{-}8).$$

In the steady state, the amount of free volume created is equal to the amount of free volume annihilated, i.e.,

$$\Delta^{+}\upsilon_f = \Delta^{-}\upsilon_f, \text{ or } \frac{\gamma\upsilon^*}{\upsilon_f} = \frac{\upsilon^*}{n_D}\frac{S}{2kT}\left[\cosh\left(\frac{\pi\Omega}{2kT}\right)-1\right]^{-1} \qquad (1\text{-}9).$$

At low stress, the extra free volume created by the applied shear stress can be annihilated by diffusion, so the free volume stays at the initial value. When the shear stress exceeds a critical value, the created free volume is more than can be annihilated by diffusion. Therefore, the free volume will increase.

Based on Spaepen's free volume model, Steif et al. (*65*) carried out strain localization analysis for inhomogeneous deformation in amorphous metals. Their analysis shows that the onset stress of catastrophic softening in a uniformly shearing body, analogous to homogeneous deformation in metallic glasses, coincides with the stress at the onset of strain localization in an identical sample with a thin band of slightly weaker material, analogous to inhomogeneous deformation in metallic glasses by the formation of shear bands. Techniques such as positron annihilation spectroscopy (PAS) (*49*), differential scanning calorimetry (DSC) (*62*) and synchrotron diffraction technique (*51, 73*), have been used to characterize the change in free volume induced by plastic deformation, which provides some experimental evidence for the free volume theory (*74-76*). For example, a slight increase in positron lifetime associated with plastic strain has been observed, indicating an increase in open volume (*77*). De Hey et al. (*78*) observed a large strain softening when amorphous $Pd_{40}Ni_{40}P_{20}$ was deformed at temperatures close to T_g. Their measurements of free volume with DSC indicated that the strain softening is caused by the creation of additional free volume during deformation, and the material

reaches a new, strain-rate dependent equilibrium state. De Hey et al. (*78-80*) applied the same idea to temperature induced structural evolution of some metallic glasses, leading to the conclusion that additional free volume is created due to plastic deformation. This observation was consistent with the free volume theory.

1.3.2 Shear transformation model

In 1979, Argon (*66*) proposed another plastic deformation mechanism in metallic glasses, in which some ideas of the free volume theory have been used. In the shear transformation model, strain is produced by local shear transformations nucleated under the applied stress with the assistance of thermal fluctuations in regions around free volume sites of the glassy structure. It is assumed that there is a distribution of free volume sites with different local coordinations, corresponding to the distribution of free energies for free volume rearrangement to produce shear strain under a small shear stress in a metallic glass, as shown in Figure 1-9, where υ_f represents the free volume of a specific local site and Ω is the average hard sphere volume.

At high temperature, the shear transformation is a diffuse rearrangement producing a relatively small local shear strain in a roughly spherical region. At low temperature, the transformation is in a narrow disk region and resembles closely the nucleation of a dislocation loop.

1.3.2.1 High temperature low stress mechanism (transition state theory)

At a temperature below T_g, the free volume state of the structure remains largely frozen-in at its state at T_g. In this temperature range, the deformation is isoconfigurational, and large-strain plastic flow is governed by the kinetics of the rearrangement of atoms in

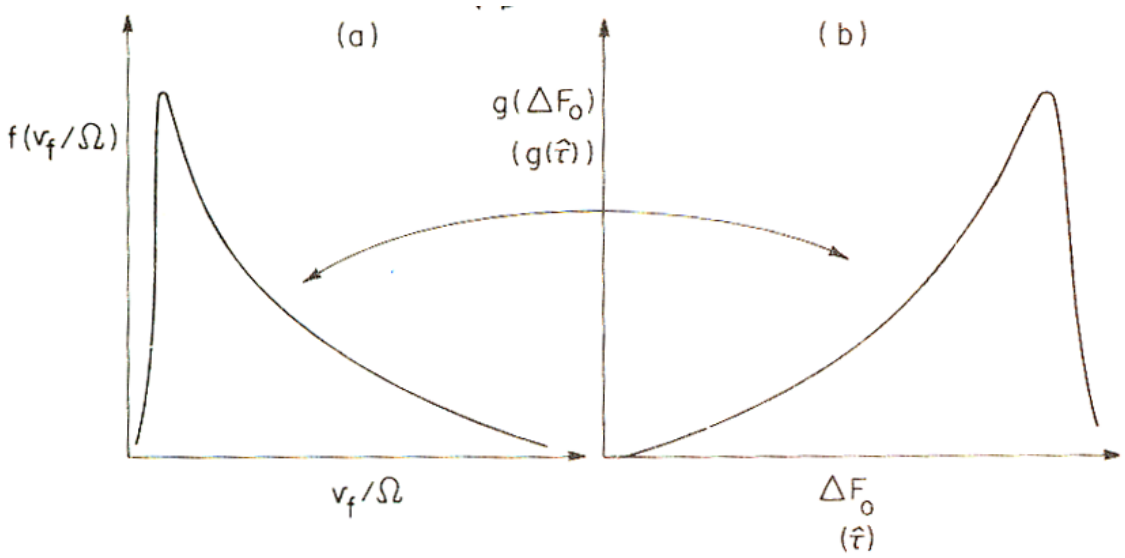

Figure 1-9. (a) Schematic representation of the distribution of free volume, and (b) the corresponding distribution of free energies for their rearrangement to produce shear strain under a small shear stress in a metallic glass (*66*).

regions around free volume sites. It is assumed that the shear resistance of the structure across a plane resembles that of a close packed metal. Argon took as a flow unit a region of volume Ω_f consisting of a free volume site and its immediate surroundings and assumed that under an applied shear stress a relatively diffuse internal arrangement of atoms around the free volume site occurs as depicted in Figure 1-10(a) and results in a local shear strain of γ_0 in this region. Based on Eshelby's discussion, a shear transformation of this type in a spherical region of size Ω_f results in an increment of elastic strain energy stored partly inside and partly outside the region and has a magnitude

$$\Delta\varepsilon = \frac{7-5\nu}{30(1-\nu)}\mu\gamma_0{}^2\Omega_f \qquad (1\text{-}10),$$

where ν is Poisson's ratio and μ is shear modulus (interlayer shear resistance). It is assumed that this elastic strain energy increment is short lived and that it will be dissipated soon after the transformation by other surrounding transformations resulting in loss of memory for the initial state in the first region. The shear strain rate at low stress is given by

$$\dot{\gamma} = \alpha\gamma_0\nu_G \exp(-\frac{\Delta\varepsilon + \gamma_0\hat{\tau}\Omega_f}{kT})\sinh\left(\frac{\sigma\gamma_0\Omega_f}{kT}\right) \qquad (1\text{-}11),$$

which incorporates also the effect of a "back flux" of reverse transformations against the applied stress giving rise to the hyperbolic sine dependence on stress. In the above equation, ν_G is the normal mode frequency of the flow unit along the activation path; α incorporates numerical constants and the steady state volume fraction of flow units

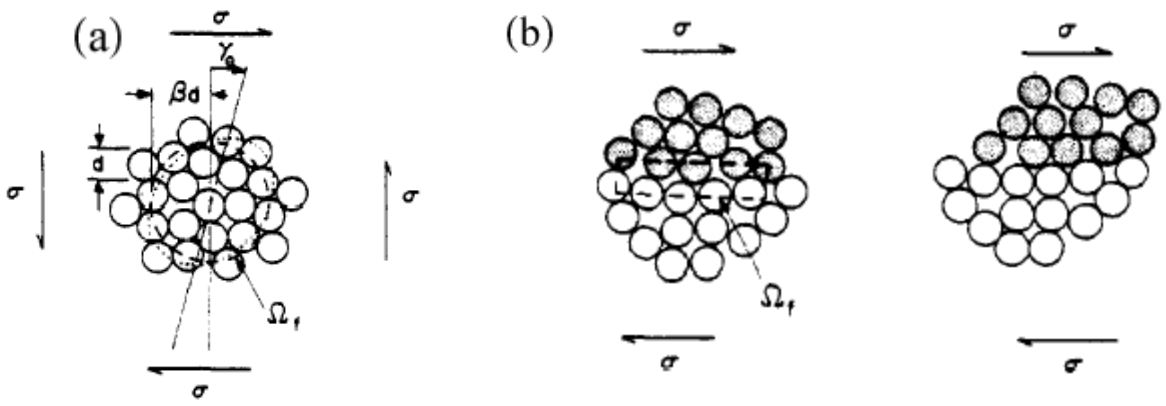

Figure 1-10. (a) A diffuse shear transformation of magnitude γ_0 inside a spherical volume element is favored at high temperatures ($T > 0.68\ T_g$); (b) a more intense shear transformation of magnitude γ_0 inside a disk shaped volume element is favored at low temperature (*66*).

contributing to plastic flow; σ is the applied shear stress; and $\hat{\tau}$ is the threshold stress for shear transformation.

1.3.2.2 Low temperature mechanism (dislocation loop theory)

According to the Bragg experiment (*81, 82*) and computer simulation of the shearing of a hard sphere glass, the shear transformation at high stresses becomes more intense but narrows down to a region between two short rows of 4~6 atoms around a free volume site. This process, depicted in Figure 1-10(b), closely resembles the nucleation of a dislocation loop that does not expand. Such a local shear transformation is consistent with the results of Eshelby from which it can be expected that the energetically favored transformation configuration is in the shape of a thin disk containing the shear transformation direction in its plane. In the limit (shear transformation occurs only between two layers of atoms) this gives a dislocation loop. The elastic strain energy increment due to the transformation is that of a circular dislocation loop of radius R,

$$\Delta\varepsilon = \frac{\mu(\Delta x)^2 R(2-\nu)}{4(1-\nu)}\left(\ln\left(\frac{4\alpha R}{d}\right)-2\right) \qquad (1\text{-}12),$$

where Δx is the relative shear displacement across the plane of the loop between a stable and an unstable equilibrium position of the configuration under the combined effect of the applied stress and the shear resistance of the structure, d is the nearest neighbor distance in the glass, and α (~ 1.0 for the type of bonding appropriate for close packed metals) is a core cut-off parameter. In the stress range $0.5 < \sigma/\tau < 1.0$ where the rate of the reverse reaction against the applied stress makes a negligible contribution, the plastic deformation rate becomes

$$\dot{\gamma} = \dot{\gamma}_G \exp\left(-\frac{\Delta G^*}{kT}\right) \qquad (1\text{-}13),$$

where ΔG^* is the activation free energy under large applied shear stresses, $\dot{\gamma}_G$ has a very similar composition and magnitude as the preexponential term in the equation for the high temperature mechanism.

Combining to the two mechanisms discussed above, the temperature dependence of the flow stress can be obtained, as shown in Figure 1-11. The use of Equation (1-11) for the high temperature mechanism gives the steeply slanted curve in Figure 1-11, rising from the glass transition temperature. On the other hand, use of Equation (1-13) for the low temperature mechanism gives the more gently slanted curve joining the normalized stress axis at unity on the left of Figure 1-11. As can be seen, the two curves intersect at a normalized temperature of about 0.68. Since these two mechanisms offer two alternatives utilizing the same defect structure of free volume sites, we must choose the easier of the two processes in any range. This led to the conclusion that the homogeneous temperature $T_h = (0.65 \sim 0.70)T_g$ controls the flow mode change: at $T < T_h$, the flow is inhomogeneous while homogeneous deformation at higher temperatures is observed. This viewpoint became widely accepted despite the lack of direct experimental confirmations.

1.3.2.3 Shear localization

In normally strain hardening materials, the basic cause of shear localization is a plastic shear strain induced reduction of deformation resistance, the actual mechanisms of which can be varied. In metallic glasses in which shear strain normally results in no important structure change (compared with phase transformations and dislocation

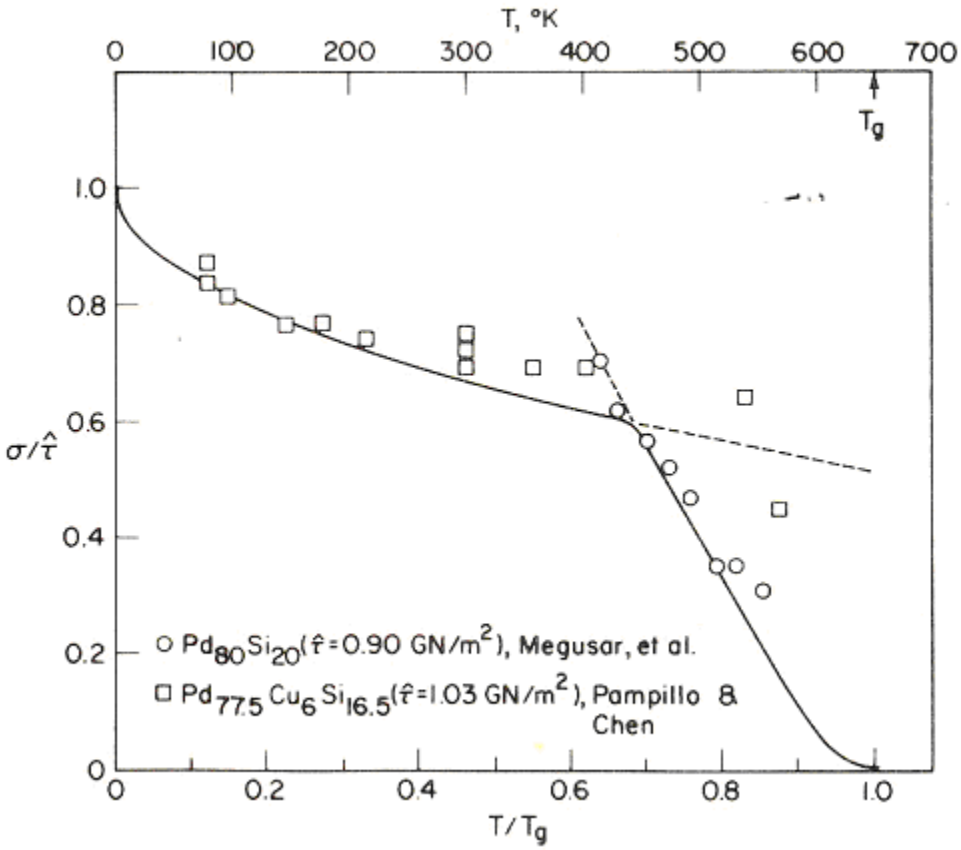

Figure 1-11. Dependence of the flow stress on temperature with low temperature data for Pd-Cu-Si, Pampillo and Chen [10], and high temperature data for Pd-Si, Megusar (*66*).

formation in crystalline materials), the only important mechanism must be the process of flow induced dilatation. If there are ranges of stress and temperature in which significant dilatations can be retained in the structure, the glass should be prone to shear localization from any flow perturbation resulting from surface imperfections or accidental internal clustering of free volume in certain regions.

1.4 Effect of sub-Tg annealing on metallic glasses

1.4.1 Structural relaxation

During the rapid quench that produces the glass from the melt, in the high temperature region, the kinetics of free volume annihilation are fast enough for equilibrium to be maintained. At lower temperatures, an excess amount of free volume is frozen in. Therefore, as-cast metallic glasses are thermodynamically unstable: they will lower their free energy continuously by a series of structural changes toward the metastable equilibrium configuration. This phenomenon is called “structural relaxation”, and is manifested by continuous changes in all physical properties, such as density (*83*), shear viscosity, and atomic diffusivity. Most measurements of the effect of relaxation on the viscosity have so far been made at temperatures well below the glass transition temperature to avoid crystallization. At these low temperatures, where the glass is far from equilibrium, the viscosity has been observed to increase linearly with time (*84, 85*). However, when the structure of the glass approaches its equilibrium configuration, the rate of the viscosity rise decreases, since the viscosity must arrive at a unique, finite, equilibrium value. Another way to study the structural relaxation is DSC (*56, 76, 86*). When the unstable metallic glass is put into a DSC and warmed up at a constant heating

rate, the excess free volume anneals out. This yields a release of energy and the process is often called topological short range ordering (TSRO), which is part of the structural relaxation of the glass. The free volume annihilation can be indirectly characterized through the released energy (*51, 56, 76, 86*). In addition, the free volume annihilation or relaxation were also characterized using real-time diffraction with synchrotron radiation (*51, 73*), and positron annihilation spectroscopy (*49*).

1.4.2 Mechanical property changes caused by structural relaxation

The structure relaxation caused by annealing, below the glass transition temperature, makes glasses exhibit different properties compared to quenched glasses. For example, the Young's modulus E of metallic glasses increases by ~ 7% and the density increases by ~ 0.5% upon annealing near the glass transition temperature (*87*). A similar Young's modulus change has also been observed by Harms et al. (*53*) and Yokoyama (*88*). Micro-hardness increased slowly (*88, 89*) and the Charpy impact toughness decreased with increasing annealing time or temperature (*88, 90, 91*). The Charpy impact values were found to follow a linear relationship with the relative amount of excess free volume, which correspond to the volume change ratio caused by the full structural relaxation (*88*). Spaepen and co-workers (*92-95*) who have conducted extensive experimental and theoretical studies on this argue that structural relaxation, characterized by the reduction in free volume and hence increased viscosity, is the primary cause for the embrittlement. Much of their work was focused on the brittle to ductile transition evident both in the morphology of fracture surfaces (from ductile vein-like morphology to a cleavage-dominant fracture mode) and the fracture stress and strain (*96*).

Most studies of the annealing effect on mechanical properties have been focused on as-cast metallic glasses. The effect of annealing on the mechanical properties of pre-deformed BMGs is quite limited. To our knowledge, there are only two related papers. One was by Krishnanand and Cahn (*61*) who rolled Ni/Nb glassy foils to about 30% reduction, annealed them at 573K for 5 hours (causing no crystallization), and then were able to roll the foils to a total reduction in the range 60 ~ 70%, without any sign of incipient cracking. They concluded that not only did the annealing restore ductility, but that the recovered ductility is greater than that of the virgin alloy glass. Their examination of shear bands indicated that annealing restored the short-range order in the deformation-induced shear bands and those bands were no longer favored sites for subsequent shear. The other paper was published by Jiang et al.(*37*) who showed that the hardness of 45.5% cold rolled Al-Ni-Y amorphous ribbon (22 μm in thickness) increases from 3.48 to 4.05 GPa after annealing at 110°C for 60 min.

What remains unknown despite these studies is whether there is any difference in the structural relaxation of shear bands compared to that of the undeformed matrix. Therefore, another purpose of our work is to systematically investigate the effect of annealing time and temperature on the hardness and structural recovery of shear bands in plastically $Zr_{52.5}Al_{10}Ti_5Cu_{17.9}Ni_{14.6}$ BMG.

1.4.3 Structural relaxation model

Based on the viscosity and released energy investigation, a bimolecular annihilation rate model has been proposed, as discussed below. In Spaepen's free volume model (*64*), the shear strain rate can be expressed as:

$$\dot{\gamma} = \Delta f \exp\left(-\frac{\gamma \upsilon^*}{\upsilon_f}\right) 2\nu \sinh\left(\frac{\pi\Omega}{2kT}\right) \exp\left(-\frac{\Delta G^m}{kT}\right) \qquad (1\text{-}14).$$

In the case of homogeneous deformation at low stress levels ($\pi\Omega << 2kT$), this leads to Newtonian viscous behavior. The viscosity (η) and free volume obey the following relation for Newtonian flow:

$$\eta = \frac{\tau}{\dot{\gamma}} = \frac{kT}{\Omega} \exp\left(\frac{\gamma \upsilon^*}{\upsilon_f}\right) \exp\left(\frac{\Delta G^m}{kT}\right) \qquad (1\text{-}15).$$

The defects in amorphous metals are often described by the free volume model, in which there are density fluctuations with volume greater than a critical value. The defect concentration is defined as:

$$c_f = \exp\left(-\frac{\gamma \nu^*}{\nu_f}\right) \qquad (1\text{-}16).$$

Therefore, the viscosity is inversely proportional to the defect concentration c_f. Based on the experimental measurements of viscosity by Tsao and Spaepen (*97*), and Taub and Spaepen (*84*), the viscosity increases linearly with time ($\frac{d\eta}{dt} = Const.$) during structural relaxation. So the annihilation rate of defects during structural relaxation can be described as

$$\left.\frac{dc_f}{dt}\right|^{-} = -kc_f^{\,2} \qquad (1\text{-}17).$$

Several researchers have shown that during isothermal annealing at temperatures close to the glass transition temperature the viscosity of amorphous metals reaches a saturation value (*97-100*). Since the viscosity is inversely proportional to the defect concentration, it

follows that the defect concentration also reaches a metastable equilibrium concentration c_{eq}. Duine, Sietsma, and van den Beukel (*100*) found from the fitting of viscosity to calorimetric data that the change of defect concentration towards equilibrium can best be described by an appropriately adapted bimolecular rate equation:

$$\left.\frac{dc_f}{dt}\right|^{-} = -kc_f(c_f - c_{eq}) \qquad (1\text{-}18).$$

Wen et al.(*101*) studied the structural relaxation occurring during annealing below the calorimetric glass transition temperature for different times and related DSC curves to the annihilation of the excess free volume by using the bimolecular rate equation.

1.5 Research objectives

The highly localized deformation in shear bands indicates that shear bands are softer than surrounding undeformed regions. However, there are only three papers in the literature dealing with deformation-induced softening of metallic glasses, none of which systematically studied the relation between plastic strain and degree of softening perhaps due to the difficulties in controlling the amount of plastic strain in metallic glasses. Therefore, one purpose of our work is to provide direct experimental evidence of deformation-induced softening and explore the relation between plastic strain and degree of softening.

It is generally accepted that extensive plastic deformation in metallic glasses is possible only by the multiplication of shear bands; however, the relation between plastic strain and shear band density (or spacing) is still quite limited. The average plastic deformation accommodated per shear band, which can be described as the average shear

offset per shear band is lacking. The only available data are those indirectly obtained by Conner et al. (*11, 12*) on the relation between the sample size and shear band spacing or shear offset in bending tests, and the dependence of plastic strain to failure on the sample size. We recently devised another way to severely deform BMGs with >5mm thickness up to 80% plastic strain without catastrophic failure by carefully controlling the sample's aspect ratio and strain rate during compression tests (*102*), which makes it possible to systematically study the behavior of shear bands during plastic deformation.

Although several researchers investigated shear band pattern underneath the indent using the bonded interface technique, clear shear band patterns are lacking, which makes it difficult to obtain detailed information about shear bands such as interaction between shear bands and the variation of shear band spacing and the height of shear band steps with distance away from indenter tip. In this work, the clamped interface technique is used to obtain clear shear band patterns, explore the interaction between shear bands, and systematically characterize shear band spacing and height of shear steps.

Although it is believed that shear bands are the weak links during deformation (*5, 23*) and that annealing can recover the structure of shear bands (*103, 104*), direct experimental evidence showing the role of pre-existing shear bands on subsequent deformation is still lacking. Therefore, we examined shear bands underneath the indents in pre-strained samples and compared them with those in the as-cast sample, to clarify the role of pre-existing bands in the subsequent deformation.

Similarly, little is known about the effect of annealing on the mechanical properties of pre-deformed BMGs. To our knowledge, the only available data are from Jiang et al.(*37*) who showed that the hardness of 45.5% cold rolled Al-Ni-Y amorphous

ribbon (22 μm in thickness) increases from 3.48 to 4.05 GPa after annealing at 110°C for 60 min. In addition, a detailed understanding of free volume annihilation in shear bands and undeformed matrix is still lacking. Therefore, we systematically investigated the effects of annealing time and temperature on the hardness of plastically deformed $Zr_{52.5}Al_{10}Ti_5Cu_{17.9}Ni_{14.6}$ BMG. The effect of sub-T_g annealing on the pre-existing shear bands was explored by examining shear band patterns underneath the indents in the deformed/annealed sample.

Most investigations on constrained plastic deformation are performed in Zr- and Pd-based metallic glasses due to their good glass forming ability. Here, we also study constrained plastic deformation in a Cu-based metallic glass to determine those features that may be common to BMGs in general.

References

1. W. L. Johnson, *MRS Bull.* **24**, 42 (1999).
2. A. Inoue, *Acta Mater.* **48**, 279 (2000).
3. P. Chaudhari, D. Turnbull, *Science* **199**, 11 (1978).
4. L. Greer, *Science* **267**, 1947 (1995).
5. C. A. Pampillo, *J. Mater. Sci.* **10**, 1194 (1975).
6. C. T. Liu, et al. *Metall. Mater. Trans.* **29A**, 1811 (1998).
7. G. J. Shiflet, Y. He, S. J. Poon, *J. Appl. Phys.* **64**, 6863 (1988).
8. G. E. Dieter, Mechanical Metallurgy (McGraw-Hill, New York, 1986).
9. D. G. Ast, D. J. Krenitsky, *Mater. Sci. Eng.* **43**, 241-246 (1980).
10. P. G. Zielinski, D. G. Ast, *Phil Mag.* **48A**, 811-824 (1983).
11. R. D. Conner, Y. Li, W. D. Nix, W. L. Johnson, *Acta Mater.* **52**, 2429-2434 (2004).
12. R. D. Conner, W. L. Johnson, N. E. Paton, W. D. Nix, *J. Appl. Phys.* **94**, 904-911 (2003).
13. A. Inoue, A. Katuya, K. Amiya, T. Masumoto, *Mater. Trans. JIM* **36**, 802-809 (1995).
14. L. A. Davis, *Scripta Metall.* **9**, 431-436 (1975).
15. P. E. Donovan, *J. Mater. Sci.* **24**, 523 (1989).
16. J. G. Wang, B. W. Choi, T. G. Nieh, C. T. Liu, *J. Mater. Res.* **15**, 798 (2000).
17. C. A. Schuh, T. G. Nieh, *J. Mater. Res.* **19**, 46-57 (2003).
18. C. A. Schuh, T. G. Nieh, *Acta Mater.* **51**, 87 (2003).

19. Y. I. Golovin, V. I. Ivolgin, V. Z. Khonik, K. Kitagawa, A. I. Tyurin, *Scripta Mater.* **45**, 947 (2001).

20. A. L. Greer, I. T. Walker, *Mater. Sci. Forum* **386-388**, 77 (2002).

21. W. J. Wright, R. Saha, W. D. Nix, *Mater. Trans. JIM* **42**, 642-649 (2001).

22. J. J. Kim, Y. Choi, S. Suresh, A. S. Argon, *Science* **295**, 654 (2002).

23. W. H. Jiang, F. E. Pinkerton, M. Atzmon, *Acta Mater.* **53**, 3469-3477 (2005).

24. R. Vaidyanathan, M. Dao, G. Ravichandran, S. Suresh, *Acta Mater.* **49**, 3781-3789 (2001).

25. M. N. M. Patnaik, R. Narasimhan, U. Ramamurty, *Acta Mater.* **52**, 3335-3345 (2004).

26. S. Jana, U. Ramamurty, K. Chattopadhyay, Y. Kawamura, *Mater. Sci. Eng.* **A 375-377**, 1191-1195 (2004).

27. U. Ramamurty, S. Jana, Y. Kawamura, K. Chattopadhyay, *Acta Mater.* **53**, 705-717 (2005).

28. H. Zhang, X. Jing, G. Subhash, L. J. Kecskes, R. J. Dowding, *Acta Mater.* **53**, 3849-3859 (2005).

29. C. Su, L. Anand, *Acta Mater.* **54**, 179 (2006).

30. H. S. Chen, *Scripta Mater.* **9**, 411-416 (1975).

31. H. S. Chen, in *Appl. Phys. Lett.* **29**, 328-330 (1976).

32. H. S. Chen, S. Y. Chuang, *Appl. Phys. Lett.* **27**, 316-317 (1975).

33. D. Akhtar, R. P. Mathur, *Z. Metallkde* **78**, 738-739 (1987).

34. G. Stergioudis, P. Rentzeperis, *Z. Metallkde* **77**, 54-55 (1986).

35. J. M. Park *et al.*, *Mater. Sci. Forum* **475-479**, 3431-3434 (2005).

36. N. Boucharat, R. Hebert, H. Rosner, H. Valiev, G. Wilde, *Scripta Mater.* **53**, 823-828 (2005).

37. W. H. Jiang, F. E. Pinkerton, M. Atzmon, in *Acta Mater.* **53**, 3469-3477 (2005).

38. S. Takayama, *J. Mater. Sci.* **16**, 2411-2418 (1981).

39. Y. Yokoyama, in *J. Non-Crystalline Solids*. **316**, 104-113 (2003).

40. J. S. Park *et al.*, in *J. Mater. Sci.* **40**, 1937-1941 (2005).

41. H. J. Jin, J. Wen, K. Lu, *Acta Mater.* **53**, 3013 (2005).

42. T. Kulik, H. Matyia, *J. Mater. Sci.* **15**, 3169-3172 (1980).

43. H. S. Chen, L. C. Kimerling, J. M. Poate, W. L. Brown, *Appl. Phys. Lett.* **32**, 461 (1978).

44. T. Masumoto, R. Maddin, *Mater. Sci. Eng.* **19**, 1 (1975).

45. G. C. Chi, H. S. Chen, C. E. Miller, *J. Appl. Phys.* **49**, 1715 (1978).

46. R. S. William, T. Egami, *Trans. on Magnetics* **12**, 927 (1976).

47. C. A. Pampillo, H. S. Chen, in *Mater. Sci. Eng.* **13**, 181-188 (1974).

48. J. Li, Z. L. Wang, T. C. Hufnagel, *Phys. Rev. B* **65**, 144201 (2002).

49. K. M. Flores *et al.*, *J. Mater. Res.* **17**, 1153-1161 (2002).

50. B. P. Kanungo, S. C. Glade, P. A. Kumar, K. M. Flores, *Intermetallics* **12**, 1073-1080 (2004).

51. K. Hajlaoui, T. Benameur, G. Vaughan, A. R. Yavari, *Scripta Mater.* **51**, 843-848 (2004).

52. R. W. Cahn, N. A. Pratten, M. G. Scott, H. R. Sinning, L. Leonardsson, *Mat. Res. Soc. Symp. Proc.* **28**, 241-252 (1984).

53. U. Harms, O. Jin, R. B. Schwarz, *J. Non-Crystalline Solids* **317**, 200-205 (2003).

54. D. Deng, B. Lu, *Scripta Metall.* **17**, 515 (1983).

55. S. Takayama, *Mat. Res. Soc. Symp. Proc.* **8**, 267 (1982).

56. W. J. Wright, T. C. Hufnagel, W. D. Nix, *J. Appl. Phys.* **93**, 1432 (2003).

57. H. Chen, Y. He, G. J. Shiflet, S. J. Poon, *Nature*. **367**, 541 (1994).

58. Y. He, G. J. Shiflet, S. J. Poon, *Acta Metall. Mater.* **43**, 83-91 (1995).

59. J. J. Kim, Y. Choi, S. Suresh, A. S. Argon, *Science*. **295**, 654-657 (2002).

60. J. Saidai, A. D. H. Setyawan, H. Kato, A. Inoue, *App. Phys. Lett.* **87**, 151907 (2005).

61. K. D. Krishnanand, R. W. Cahn, *Scripta Mater.* **9**, 1259-1261 (1975).

62. Q. P. Cao, J. F. Li, Y. H. Zhou, A. Horsewell, J. Z. Jiang, *Appl. Phys. Lett.* **87**, 101901 (2005).

63. C. Tang, Y. Li, K. Zeng, *Mater. Sci. Eng. A* **384**, 215 (2004).

64. F. Spaepen, *Acta Metall.* **25**, 407-415 (1977).

65. P. S. Steif, F. Spaepen, J. W. Hutchinson, *Acta Metall.* **30**, 447 (1982).

66. A. S. Argon, *Acta Metall.* **27**, 47-58 (1979).

67. A. S. Argon, L. T. Shi, *Acta Mater.* **31**, 499-507 (1983).

68. J. Megusar, A. S. Argon, N. J. Grant, *Mater. Sci. Eng.* **38**, 63-72 (1979).

69. V. A. Khonik, A. T. Kosilov, V. A. Mikhailov, V. V. Sviridov, *Acta Mater.* **46**, 3399 (1998).

70. V. A. Khonik, V. A. Mikhailov, I. A. Safonov, *Scripta Mater.* **37**, 921 (1997).

71. M. H. Cohen, D. Turnbull, *J. Chem. Phys.* **31**, 1164 (1959).

72. D. E. Polk, D. Turnbull, *Acta Metall.* **20**, 493 (1972).

73. A. R. Yavari *et al.*, *Acta Mater.* **53**, 1611-1619 (2005).

74. F. Spaepen, *Acta Metall.* **25**, 407-415 (1975).

75. A. S. Argon, *Acta Mater.* **27**, 47-58 (1979).

76. P. S. Steif, F. Spaepen, J. W. Hutchinson, *Acta Mater.* **30**, 441 (1982).

77. K. M. Flores *et al.*, *J. Mater. Res.* **17**, 1153 -1161 (2002).

78. P. Dehey, J. Sietsma, A. Vandenbeukel, *Mater. Sci. Eng. A* **226**, 336-340 (1997).

79. G. Ruitenberg, P. Dehey, F. Sommer, J. Sietsma, *Phys. Rev. Lett.* **79**, 4830-4833 (1997).

80. B. Van Aken, P. Dehey, J. Sietsma, *Mater. Sci. Eng. A* **278**, 247-254 (2000).

81. L. Bragg, J. F. Nye, *Proc. R. Soc.* **A190**, 474 (1947).

82. L. Bragg, W. M. Lomer, *Proc. R. Soc.* **A196**, 171 (1949).

83. C. Nagel, K. Ratzke, E. Schmidtke, F. Faupel, W. Ulfert, *Phys. Rev. B* **60**, 9212 (1999).

84. A. I. Taub, F. Spaepen, *Acta Metall.* **28**, 1781 (1980).

85. A. I. Taub, F. E. Luborsky, *Acta Metall.* **29**, 1939-1948 (1981).

86. K. Kristiakova, P. Svec, J. Kristiak, O. Sausa, P. J. Duhaj, *J. Non-Crystalline Solids* **193**, 277 (1995).

87. H. S. Chen, *J. Appl. Phys.* **49**, 3289-3291 (1978).

88. Y. Yokoyama *et al.*, *Mater. Trans.* **46**, 2755-2761 (2005).

89. Z. Zhang, J. Xie, *Mater. Sci. Eng. A* **407**, 161 (2005).

90. U. Ramamurty, M. L. Lee, J. Basu, Y. Li, *Scripta Mater.* **47**, 107-111 (2002).

91. P. Murali, U. Ramamurty, *Acta Mater.* **53**, 1467 (2005).

92. F. Spaepen, S. S. Tsao, T. W. Wu, Proceedings of the EPRI-Acta Metallurgica Workshop on Amorphous Metals and Semiconductors, pp.365 (USA: Pergamon Press, 1986).

93. F. Spaepen, A. I. Taub, Amorphous metallic alloys, pp.231 (Butterworth, London, 1983).

94. T. W. Wu, F. Spaepen, Mechanical behavior of rapidly solidified metals, pp.293 (USA: The Metallurgical Society of AIME, 1986).

95. E. P. Barth, F. Spaepen, R. Bye, S. K. Das, *Acta Mater.* **45**, 423 (1997).

96. M. Yan, J. F. Sun, J. Shen, *J. Alloys Compounds* **381**, 86-90 (2004).

97. S. S. Tsao, F. Spaepen, *Acta Mater.* **33**, 881-891 (1985).

98. C. A. Volkert, F. Spaepen, *Mater. Sci. Eng.* **97**, 449 (1988).

99. C. A. Volkert, F. Spaepen, *Acta Metall.* **37**, 1355 (1989).

100. P. A. Duine, J. Sietsma, A. Vandenbeukel, *Acta Metall. Mater.* **40**, 743 (1992).

101. P. Wen, *et al.*, *Phys. Rev. B* **67**, 212201 (2003).

102. H. Bei, S. Xie, E. P. George, *Phys. Rev. Lett.* **96**, 105503 (2006).

103. P. S. Steif, F. Spaepen, J. W. Hutchinson, *Acta Mater.* **30**, 441 (1982).

104. W. J. Wright, T. C. Hufnagel, W. D. Nix, *J. Appl. Phys.* **93**, 1432 (2003).

2 EXPRIMENTAL PROCEDURES

2.1 Preparation of bulk metallic glasses and composites

2.1.1 $Zr_{52.5}Al_{10}Ti_5Cu_{17.9}Ni_{14.6}$ BMG

The bulk metallic glass Zr-10Al-5Ti-17.9Cu-14.6Ni (*1, 2*) was prepared by arc melting high purity Zr, Al, Ni, Cu and Ti in argon atmosphere, followed by drop casting into 6.7-mm-diameter by 7.2-cm-long Cu molds. The amorphous structure of the specimens was confirmed by means of X-ray diffraction (XRD) analysis and differential scanning calorimetry (DSC) at a heating rate of 20 K/min.

2.1.2 $Cu_{60}Zr_{30}Ti_{10}$ BMG

The bulk metallic glass Cu-30Zr-10Ti (*3*) was prepared by arc melting high purity Cu, Zr, and Ti in argon atmosphere, followed by drop casting into 3-mm-diameter by 7.2-cm-long Cu mold. The amorphous structure of the specimens was confirmed by means of X-ray diffraction (XRD) analysis.

2.1.3 $(Zr_{70}Ni_{10}Cu_{20})_{82}Ta_8Al_{10}$ BMG composite and its matrix

Master alloy ingots of $(Zr_{70}Ni_{10}Cu_{20})_{82}Ta_8Al_{10}$ (*4*) were prepared by arc melting on a water-cooled copper hearth under a Ti-gettered argon atmosphere in a two-step procedure. The first step was to make a Zr-Ta master alloy ingot. In equilibrium at room temperature, Zr-Ta binary alloys form a two-phase mixture of Zr- and Ta-rich solid solution. The second step was to arc melt such an ingot together with Cu, Ni and Al and produce an alloy ingot of the desired final composition. The composite samples were produced by drop casting into a 3-mm-diameter and 7.2-cm-long Cu mold. X-ray analysis

revealed sharp peaks from a Ta solid solution superimposed on a broad scattering peak characteristic of an amorphous phase.

For comparison, a metallic glass having the composition $(Zr_{70}Ni_{10}Cu_{20})_{90}Al_{10}$ of the matrix in the composite was also prepared by arc-melting and drop casting, using the same procedure as that described in 2.1.2 for the $Cu_{60}Zr_{30}Ti_{10}$ metallic glass.

2.2 Constrained compression of bulk metallic glasses

2.2.1 $Zr_{52.5}Al_{10}Ti_5Cu_{17.9}Ni_{14.6}$ BMG

Using electron-discharge machining (EDM), the drop-cast $Zr_{52.5}Al_{10}Ti_5Cu_{17.9}Ni_{14.6}$ BMG rods were cut into short rods with thickness of 3 ~ 13.4mm, corresponding to aspect ratios (A=height/diameter) of 0.45 ~ 2. These rods were compressed at room temperature using a MTS 8100 servo-hydraulic machine at strain rates from 1×10^{-6} s^{-1} to 5×10^{-1} s^{-1}. The specimen thickness before and after compression was measured to calculate the plastic strain which is defined as $\varepsilon_p = (l_0 - l)/l_0$, where l_0 and l are the specimen thickness before and after compression. X-ray diffraction analysis was performed on the severely deformed samples.

2.2.2 $Cu_{60}Zr_{30}Ti_{10}$ BMG, $(Zr_{70}Ni_{10}Cu_{20})_{90}Al_{10}$ BMG and $(Zr_{70}Ni_{10}Cu_{20})_{82}Ta_8Al_{10}$ composite

The drop-cast rods of the $Cu_{60}Zr_{30}Ti_{10}$ BMG, $(Zr_{70}Ni_{10}Cu_{20})_{90}Al_{10}$ BMG, and $(Zr_{70}Ni_{10}Cu_{20})_{82}Ta_8Al_{10}$ composite, were cut into discs 2.0 mm in thickness using electron-discharge machining (EDM) and compressed at room temperature using the MTS 8100 at a strain rate of 1×10^{-3} s^{-1}.

2.3 Examination of shear bands produced by compression

To reveal the shear deformation produced by constrained compression, the side surface of a few $Zr_{52.5}Al_{10}Ti_5Cu_{17.9}Ni_{14.6}$ rods with aspect ratio 0.5, were ground through 600 grit SiC and polished with 0.5 μm Al_2O_3 to a mirror finish. These specimens were compressed to different amounts of plastic strain (from 0% to 80%) by carefully controlling the reduction of specimen thickness. Scanning electron microscopy (SEM) and laser interferometry were used to examine shear bands on the free surfaces of various plastically deformed samples. Shear band spacing was measured by averaging the number of shear bands over the sample height. Shear offset was measured in two ways: the displacement produced by the intersection of shear bands and the height of shear steps out of the free surface.

A few $Cu_{60}Zr_{30}Ti_{10}$, $(Zr_{70}Ni_{10}Cu_{20})_{90}Al_{10}$ and $(Zr_{70}Ni_{10}Cu_{20})_{82}Ta_8Al_{10}$ rods with aspect ratio 0.67, were also ground through 600 grit SiC and polished with 0.5 μm Al_2O_3 to a mirror finish. These specimens were compressed to various plastic strains (from 0% to 50%) by carefully controlling the reduction of specimen thickness. Scanning electron microscopy (SEM) was used to examine shear bands on their free surfaces and the shear band spacing was measured by averaging the number of shear bands over the sample height.

2.4 Annealing and re-compression of $Zr_{52.5}Al_{10}Ti_5Cu_{17.9}Ni_{14.6}$ BMG

The as-cast and various pre-strained $Zr_{52.5}Al_{10}Ti_5Cu_{17.9}Ni_{14.6}$ BMG specimens were annealed in vacuum at 373K for 2, 16 and 24 hours, at 473K and 633K (lower than T_g) for 2 hours. For simplification, some samples were renamed and are listed in

Table 2-1. Sample identities based on processing history

Sample Name	Processing
as-cast	as-cast
D33	33% plastic strain
D50	50% plastic strain
D50A373	50% plastic strain + annealed at 373K for 2 hours
D50A473	50% plastic strain + annealed at 473K for 2 hours
D50A633	50% plastic strain + annealed at 633K for 2 hours
D33A373	33% plastic strain + annealed at 373K for 2 hours
D33A473	33% plastic strain + annealed at 473K for 2 hours
D33A373D	33% plastic strain + annealed at 373K for 2 hours + 33% plastic strain
D33A473D	33% plastic strain + annealed at 473K for 2 hours + 33% plastic strain

Table 2-1. The D50, D50A100, D50A200, and D50A360 samples were electrochemically etched (*5*) in order to explore the effect of sub-T_g annealing on the morphology of shear bands produced by the preceding compression. Two annealed samples (D33A100 and D33A200) were compressed again to 33% plastic strain, at room temperature using the MTS 8100 at a strain rate of 1×10^{-3} s^{-1}, in order to explore whether reversible softening occurred in metallic glasses.

2.5 Micro-hardness tests and examination of deformation zone around the indents

2.5.1 $Zr_{52.5}Al_{10}Ti_5Cu_{17.9}Ni_{14.6}$ BMG

The flat surfaces of strained $Zr_{52.5}Al_{10}Ti_5Cu_{17.9}Ni_{14.6}$ BMG (from 0% to 80%) and all samples listed in Table 2-1, were polished with 600 grit SiC paper and then 0.5 μm Al_2O_3 to mirror finish. Vickers hardness tests were conducted on them using a Buehler Micromet 2001 microhardness tester at a load of 1000g. The holding time at maximum load was 20s. The regions surrounding the Vickers indents were examined using laser interferometry and optical microscopy (OM).

For as-cast, D50, D50A100, D50A200, and D50A360 samples, two mirror-finish samples from each processing step were clamped together with the polished surfaces face-to-face using a specially designed vice. The entire assembly including samples and vice were cold-mounted in epoxy resin, ground through 600 grit SiC, and polished with 0.5 μm Al_2O_3 to mirror finish. Vickers indents (1000gf) were made at the interface with the indenter diagonal parallel to the interface or at 45° to the interface, as shown in Fig. 2-1.

After indenting, the epoxy resin and clamp were removed and the two halves

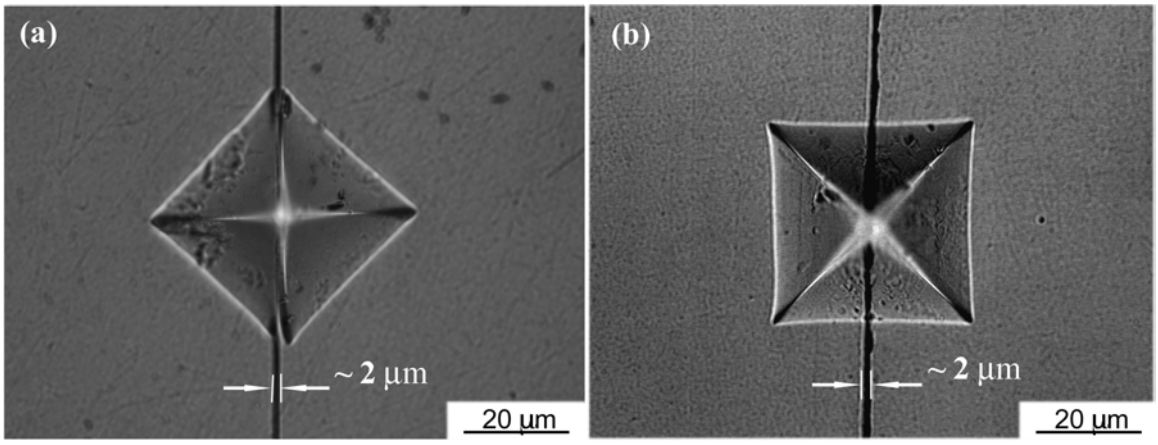

Figure 2-1. Typical Vickers indents at the interface between polished BMG surfaces (a) indenter diagonal parallel to the interface, and (b) indenter diagonal at 45° to the interface.

separated to reveal the deformation zone underneath the indent. The deformation zones beneath the interface indenters were examined by scanning electron microscope (SEM) and atomic force microscope (AFM). The extent of the plastic zone underneath the indent, defined as the distance between the indenter's first contact point on the surface and the farthest shear band, was measured as a function of the maximum load.

2.5.2 $Cu_{60}Zr_{30}Ti_{10}$, $(Zr_{70}Ni_{10}Cu_{20})_{90}Al_{10}$ BMGs and $(Zr_{70}Ni_{10}Cu_{20})_{82}Ta_8Al_{10}$ composite

The flat surfaces of various strained $Cu_{60}Zr_{30}Ti_{10}$ BMG (from 0% to 50%), were polished with 600 grit SiC paper and then 0.5 μm Al_2O_3 to mirror finish. Vickers hardness tests were conducted on them using a Buehler Micromet 2001 microhardness tester at a load of 1000g, following the same procedure as that described in section 2.5.1, except that only the parallel orientation shown in Fig. 2-1(a) was used.

For the as-cast $(Zr_{70}Ni_{10}Cu_{20})_{90}Al_{10}$ BMG and $(Zr_{70}Ni_{10}Cu_{20})_{82}Ta_8Al_{10}$ composite, the procedure was the same as that described above for $Cu_{60}Zr_{30}Ti_{10}$ BMG.

2.6 Nanoindentation test in the deformation zone underneath Vickers indents

Nanoindentation tests were performed using the MTS Nano-XP instrument in the plastic zone underneath the Vickers indent of $Zr_{52.5}Al_{10}Ti_5Cu_{17.9}Ni_{14.6}$ and $Cu_{60}Zr_{30}Ti_{10}$ samples as well as away from the plastic zone. A maximum load of 15mN at a strain rate of 0.05/s was applied and the holding time at maximum load was 20s. A 10 μm distance between two neighboring indents was maintained.

References

1. C. T. Liu *et al.*, *Metall. Mater. Trans.* **29A**, 1811-1820 (1999).

2. X. H. Lin, W. L. Johnson, W. K. Rhim, *Mater. Trans. JIM* **38**, 473 (1997).

3. A. Inoue, W. Zhang, T. Zhang, K. Kurosaka, *Acta Mater.* **49**, 2645 (2001).

4. C. Fan, R. T. Ott, T. C. Hufnagel, in *App. Phys. Lett.* **81**, 1020 (2002).

5. Y. Zhang, W. H. Wang, A. L. Greer, in *Nature Mater.* **5**, 857 (2006).

3 Profuse shear banding and softening induced by constrained deformation in $Zr_{52.5}Al_{10}Ti_5Cu_{17.9}Ni_{14.6}$ BMG

3.1 Shear banding and softening during uniaxial compression

3.1.1 Obtaining severe plastic deformation

Figure 3-1 (a) shows cylindrical specimens having an initial height and aspect ratio of 3.5 mm and 0.52, respectively, after various amounts of compression at an engineering strain rate of 1.7×10^{-3} s^{-1}. The compressed specimens were metallographically polished and examined in a scanning electron microscope. No micro-cracks were observed anywhere on the polished surface. Clearly, by geometrically constraining the shear bands ($A < 1$), extensive plastic deformation of the BMG is possible even at room temperature, which is a low temperature compared to its T_g of ~ 663K. The plastic strain (ε_p) achievable is 80% which is significantly higher than anything previously reported in relatively thick specimens of single-phase BMGs. X-ray diffraction revealed no evidence of crystallization, even in the most heavily deformed specimens.

When A is increased to 2, i.e., the physical constraint on the shear bands is removed, the BMG fractures in a brittle manner ($\varepsilon_p < 1.0\%$) at ~45° to the loading axis [Fig. 3-1 (b)], consistent with other reports [e.g., 9]. Interestingly, at high strain rates (e.g., $> 5 \times 10^{-1}$ s^{-1}), brittle fracture occurs regardless of the aspect ratio. Both parameters are therefore important in determining whether extensive plastic deformation is possible.

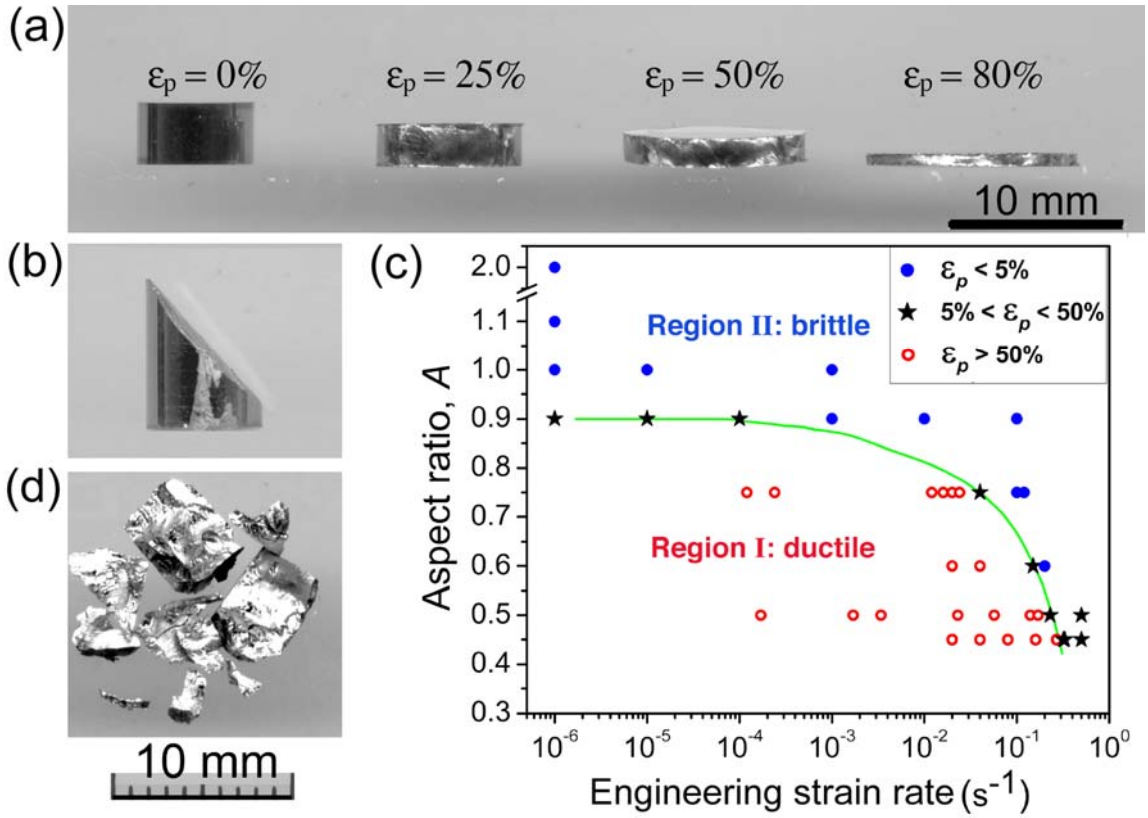

Figure 3-1. Room-temperature compression of a Zr-based metallic glass with T_g = 390°C. **(a)** Change in height of low-aspect-ratio specimens after plastic straining. **(b)** High-aspect-ratio specimen exhibiting brittle fracture at ~45° to the vertical loading axis. **(c)** "Deformation map" showing the effects of aspect ratio and strain rate on the plastic strain to failure. **(d)** At high strain rates brittle fracture occurs even in low-aspect-ratio specimens.

Figure 3-1 (c) is a "deformation map" for the Zr-based BMG showing the combined effects of aspect ratio and strain rate on plastic strain. There are two distinct regions: Region I, where aspect ratio and strain rate are low, is the ductile region; here, extensive plastic deformation ($\varepsilon_p > 50\%$) is possible without specimen fracture. Region II, with high aspect ratio and/or strain rate, is the brittle region ($\varepsilon_p < 5\%$). Previous compression tests on single-phase BMGs [e.g., 8, 9] generally fall within this second region.

The above results may be rationalized as follows. When the aspect ratio is greater than 1, the specimens shear off at ~45° to the loading axis [Fig. 3-1 (b)] as a result of a few highly localized shear bands propagating unrestricted through the specimen. In contrast, when $A < 1$, the compression platens block the 45° shear bands from going through the sample thereby forcing the nucleation of new shear bands to carry the plastic deformation. The resulting multiplication of shear bands redistributes plastic strain and helps prevent crack formation. The effect of the second parameter, strain rate, on plastic strain is the result of competition between stress build-up and relaxation. At low strain rates, there is enough time for the blocked shear bands to release the built-up stresses and avoid crack formation. At high strain rates, the tensile components of the built-up stresses do not have enough time to relax, which leads to brittle fracture and sometimes even shattering of the specimens [Fig. 3-1 (d)]. This is the first time that a strain rate effect on deformability has been reported in a BMG strained at a temperature significantly below T_g; usually, strain rate effects are observed only at temperatures close to T_g where BMGs exhibit viscous flow [18-20].

3.1.2 Shear bands produced by constrained compression

Macroscopically, the glass deforms homogenously, i.e., decreases in thickness uniformly. Microscopically, the mode of plastic deformation is inhomogeneous flow with multiple shear bands forming on the specimen surfaces. Figure 3-2 shows the typical shear band patterns on the samples' free surfaces parallel to the loading direction at various plastic strains, revealing multiple shear bands generated after the constrained compression. From these SEM images, it is found that not only does the number of shear bands increase with increasing plastic strain, but also the morphology of the shear band patterns changes. At $\varepsilon_p = 10\%$, most of the shear bands are parallel to each other and along ~ 45° to the loading direction, as shown in Fig. 3-2(a). At $\varepsilon_p = 25\%$ [Fig. 3-2(b)], two groups of shear bands appear: one is perpendicular to the loading direction on the observed free surface (arrowed by A); the other is along ~ 45° to the loading direction on the observed free surface (arrowed by B). The intersection between two groups of bands forms the net-like patterns. With a further increase of plastic strain, the number of both groups of shear bands increases. Their intersection is more frequent, resulting in a higher density of the net-like patterns, as shown in Fig. 3-2(c) and (d). A more detailed examination of the intersection between shear bands reveals that some shear bands are shifted (displaced) along the intersecting shear bands, causing shear offset, as indicated by rectangles in Fig. 3-2(b)-(d).

Figure 3-3 shows interference optical microscopy images at $\varepsilon_p = 10\%$ and $\varepsilon_p = 25\%$. It is found that all shear bands are displaced out of the free surfaces and form some steps on the free surfaces. The height of shear band steps (or shear offsets) suddenly

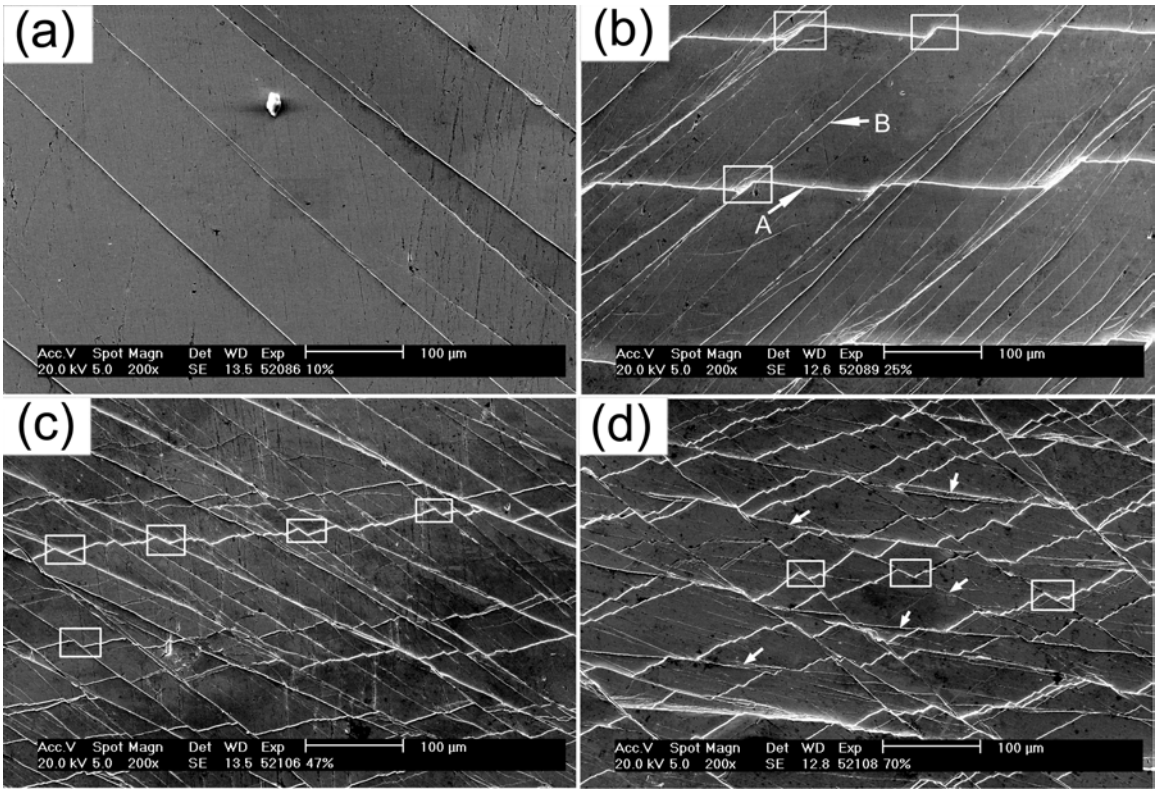

Figure 3-2. Typical shear band patterns on a free surface parallel to the loading direction after various plastic strains: (a) ε_p = 10%, (b) ε_p = 25 %, (c) ε_p = 47%, (d) ε_p = 70%. The rectangles indicate shear offset steps at the intersections of shear bands.

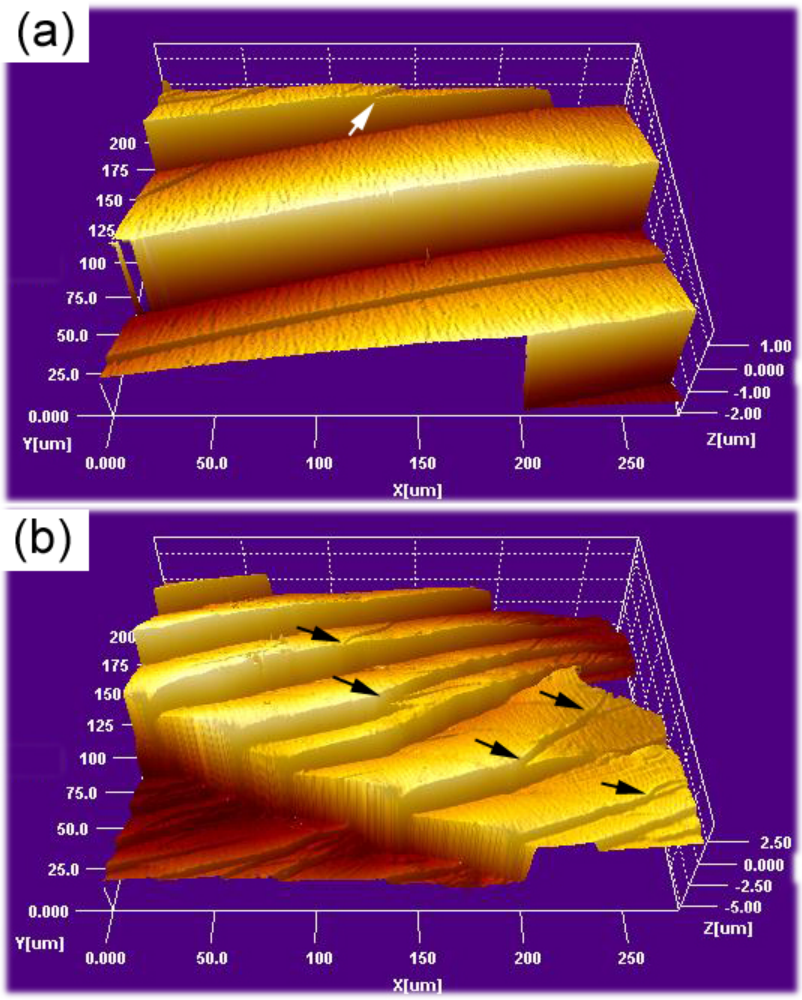

Figure 3-3. Shear offsets on a free surface that is parallel to the loading direction observed by laser interference microscopy: (a) ε_p = 10%, (b) ε_p = 25 %.

drops when one shear band branches into two or more bands, as pointed by arrows in Fig. 3-3, which indicates that the plastic strain accommodated by one shear band decreases when multiple shear bands contribute to the same total amount of plastic deformation. Therefore, it is possible to obtain severe plastic deformation without the catastrophic failure when a large number of shear bands are generated.

In order to better understand why shear bands are along two different directions and how they intersect each other, the shear band geometry is schematically illustrated in Fig. 3-4. It is known that BMGs shear approximately along the maximum shear stress plane in compressive tests. Two kinds of maximum shear stress planes are shown in Fig. 3-4(a). When shear planes along different 45° directions such as plane ABCD and AEFG intersect with the sample surfaces, two groups of shear bands are visible: one is perpendicular to the loading axis [band DC in Fig. 3-4(a)]; the other is along ~ 45° to the loading axis [band GF in Fig. 3(a)]. This is why there are two groups of shear bands along different directions in Fig. 3-2(b)-(d). Depending on the sequence in which they are generated, these two kinds of shear planes (bands) may be referred to primary and secondary shear planes (bands), with the former generated before the latter. The propagation of the secondary shear band cuts through the primary, resulting in a displacement (or shear offset) of the primary shear plane along the shear direction of the secondary, as illustrated in Fig. 3-4(b), analogous to the intersection of edge dislocations with Burgers vectors at right angles to each other in crystalline materials (*1*). The observed shear offsets in Fig. 3-2(b)-(d) are thus the results of the intersection between two different sets of shear planes.

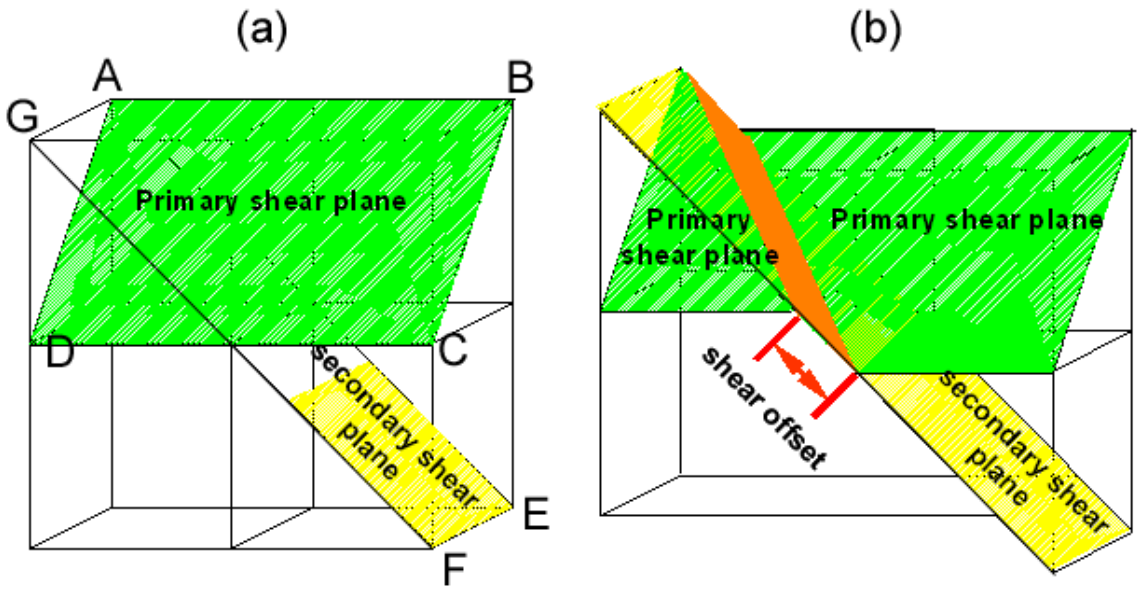

Figure 3-4. Schematic illustration of shear band intersection in a three-dimensional view: (a) two kinds of maximum shear stress planes; (b) propagation of the secondary shear plane through the primary shear plane forms a shear offset on the primary one along the secondary shear direction.

Fig. 3-5 shows the distribution of angles between two groups of shear bands at various plastic strains. It can be seen that the average angle decreases with increasing plastic strain. A possible reason for this is as follows. The shear bands rotate away from the maximum shear stress plane to accommodate further plastic deformation, as illustrated in Fig. 3-6(a) and (b). After rotation, the existing shear bands are no longer along the maximum shear stress planes, i.e., unfavorable for further shearing. New favorably oriented shear bands along the maximum shear stress planes are then generated, which intersect the existing bands. These new shear bands also undergo rotation to accommodate further plastic deformation, as illustrated in Fig. 3-6(c). Therefore, the average angle measured on the free surface becomes smaller. Shear band rotation is also reported in Ti-based nano-composites (*2*), however, the strong intersection and rotation of shear bands have not been reported in monolithic BMGs before, possibly because extensive plastic deformation in thick BMGs (>3mm)has not been obtained until now.

In order to relate the shear band multiplication to plastic deformation, the shear band density, ρ, (defined as the number of shear bands per unit length along the compressive direction) was measured and expressed as a function of the plastic strain, as shown in Fig. 3-7. From the plot, it can be seen that the shear band density increases linearly with increasing strain, i.e., the shear band spacing, d, (defined as the average distance between two nearest shear bands) is inversely proportional to plastic strain:

$$\rho = 0.14\,\varepsilon_P, \text{ or } d^{-1} = 0.14\,\varepsilon_P, \qquad (3\text{-}1)$$

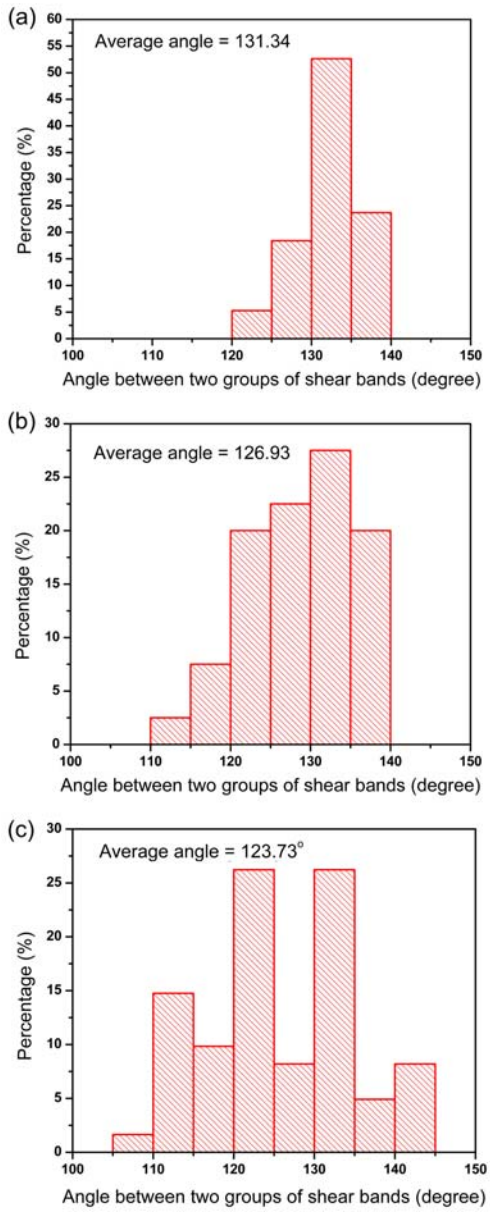

Figure 3-5. The distribution of angles between two groups of shear bands at various plastic strains: (a) ε_p = 25%, (b) ε_p = 47 %, (c) ε_p = 70%.

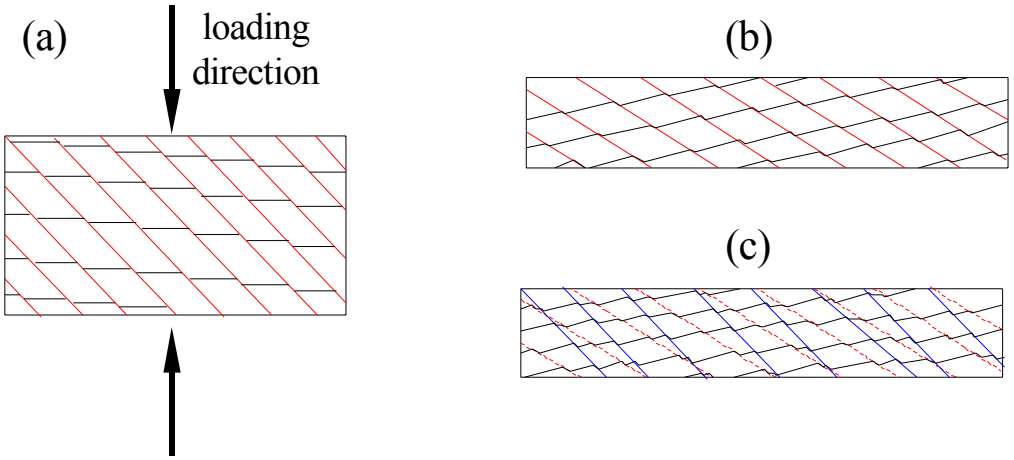

Figure 3-6. Schematic diagrams showing shear band rotation and new shear band generation: (a) Primary (black) and secondary (red) shear bands appearing on the sample surface, (b) rotation of shear bands away from the maximum shear plane to accommodate the compressive strain, (c) generation of new favorably oriented shear bands, which cut through the existing shear bands and form new shear offsets.

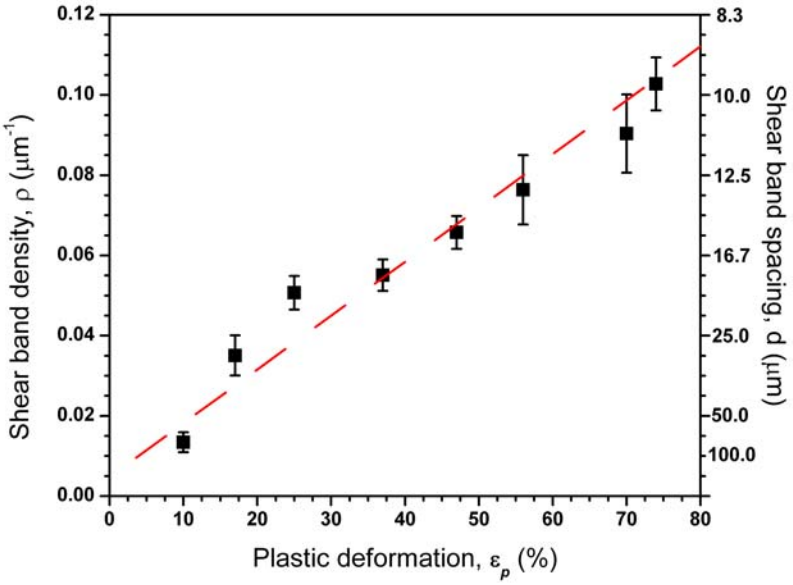

Figure 3-7. Linear increase (decrease) of shear band density (spacing) with increasing plastic strain, i.e., shear band spacing is inversely proportional to plastic strain.

where ρ is the shear-band density (units of μm^{-1}), d is the shear band spacing ($d = \rho^{-1}$), and ε_p is the plastic strain. Moreover, the linear $\rho \sim \varepsilon_p$ relation indicates that the average shear offset per shear band is a constant ~ $7\,\mu m$. To examine the reasonableness of the calculated value, shear offsets at various plastic strains were measured and plotted as a frequency distribution, as shown in Fig. 3-8. At least 50 offsets were measured on SEM images for each distribution. From Fig. 3-8, it is found that the average shear offset per shear band is about 4.5 μm regardless of the plastic strain. Although some large shear offsets appear after severe plastic deformation, such as 26 μm at 47% and 70% plastic strains, many shear bands with small offsets are also generated [Fig. 3-8 (c) and (d)], resulting in similar average value of shear offsets at various plastic strains within the margin of error. The slope of the linear relation between shear band density and plastic strain (~ 7 μm) is comparable to the measured shear offset value (~4.5 μm).

3.1.3 Softening caused by profuse shear banding

Figure 3-9 shows that the hardness decreases linearly with increasing plastic strain and decreasing shear band spacing. These hardness values (nanoindentation as well as the two sets of Vickers data obtained at different loads) reflect the composite properties of the shear bands plus the surrounding undeformed glass. This is because our hardness impressions vary in size from 2-30 μm, whereas the shear band spacing varies from 10-100 μm. As mentioned earlier, it is very difficult to measure the hardness of just the shear bands.

In order to deconvolute the hardness of the shear bands from that of the

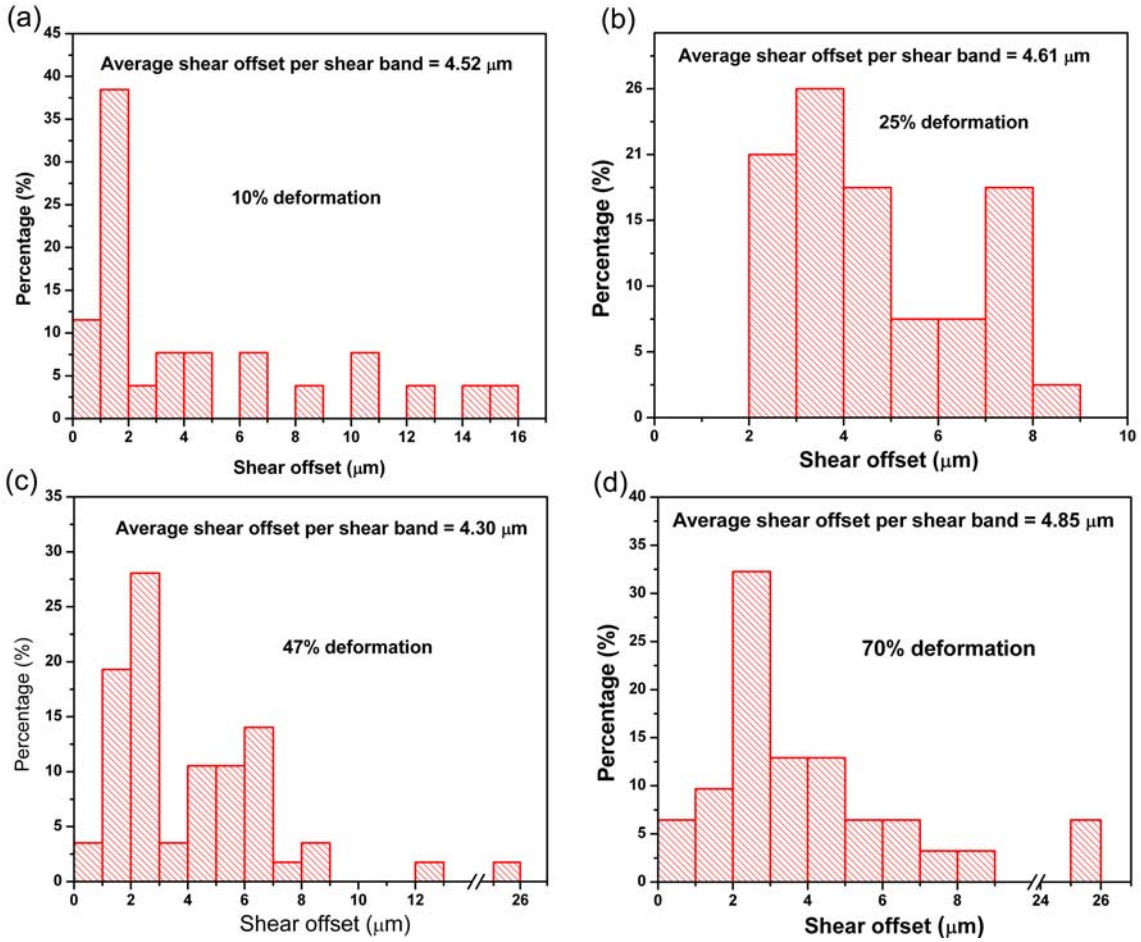

Figure 3-8. Shear offset frequency distribution plots of number fraction (expressed as percentage) versus shear offset at various plastic strains: (a) ε_p = 10%, (b) ε_p = 25 %, (c) ε_p = 47%, (d) ε_p = 70%.

undeformed glass we need a model for the composite hardness. We note that the softening associated with decreased shear band spacing is reminiscent of the inverse Hall-Petch behavior in nanocrystalline materials below a critical grain size [21,22]. The inverse behavior (strength decreasing with grain size) has been attributed to plastic deformation becoming hard within the crystalline grains but easy within the grain boundaries. In an analogous manner, we assume here that the deformed BMG consists of amorphous "grains," which are relatively hard, surrounded by soft shear-band "boundaries," which is reasonable given the grid-like pattern of the shear bands [Fig. 3-2]. The stress to shear such a composite along a plane is given by [23]:

$$\sigma = V_g \sigma_g + V_{sb} \sigma_{sb}, \qquad (3\text{-}2)$$

where V_g is the fraction of undeformed glass on the shear plane, $V_{sb} = 1\text{-}V_g$ is the shear band fraction, and σ_g and σ_{sb} are the flow stresses of the undeformed glass and shear bands, respectively. Since hardness is proportional to flow stress, and $V_{sb} = t/d$, where t and d are the thickness and spacing, respectively, of the pre-existing shear bands (which are intersected by the indentation shear bands), we obtain the following expression for the hardness of the deformed glass:

$$H = H_g - t\left(H_g - H_{sb}\right)d^{-1}, \qquad (3\text{-}3)$$

where H_g and H_{sb} are the hardnesses of the undeformed glass and the shear bands, respectively. Therefore, if H is plotted as a function of d^{-1}, as in Fig. 3-9, the intercept and slope of the linear fit yield values for H_g, and $t(H_g\text{-}H_{sb})$, respectively. Recently, Lewandowski and Greer [24] showed that the shear band thickness is on the order of 200-

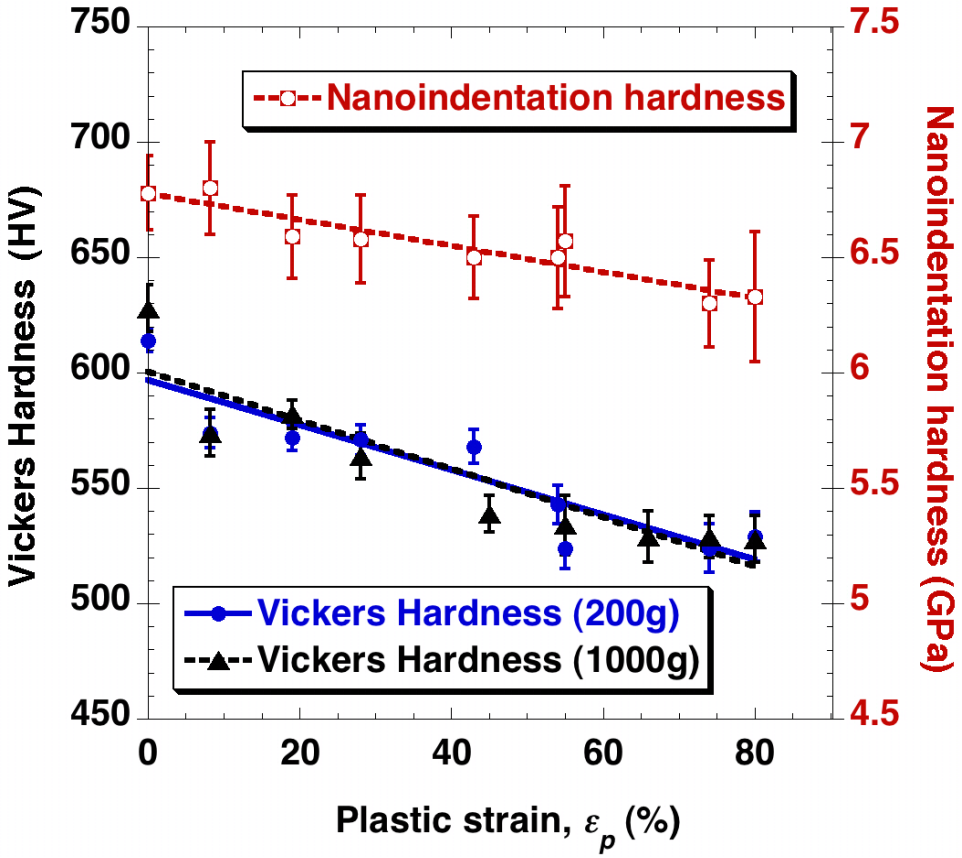

Figure 3-9. Decrease in hardness (nanoindentation and Vickers at two different loads) with increasing plastic strain.

1000 nm. Using a middle value of 600 nm for the effective shear band thickness, t, we estimate from the nanoindentation data that H_{sb} = 1.4 GPa which is considerably lower than the hardness of the undeformed glass, H_g = 6.7 GPa. As a result of this lower hardness, plasticity, rather than spreading throughout the material, will tend to stay localized in a few shear bands, leading to the commonly observed shear instability and brittle fracture of metallic glasses.

In order to investigate possible mechanisms for this softening we measured the thermal and elastic properties of the deformed glass. As demonstrated by the DSC results in Fig. 3-10 (b), a small decrease in the crystallization temperature with increasing strain was observed (~4°C at ε_p = 80%). It appears, therefore, that a portion of the work done during deformation remains stored in the BMG, perhaps as strain-induced local dilatation (increase in certain interatomic distances or the so-called free volume) [25]. A modest decrease in the Young's modulus with increasing strain (1-2% decrease at ε_p = 80%) was also observed [Fig. 3-10 (a)], which is in agreement with Chen's earlier results [26]. The above results are consistent with a shear-induced local dilatation, which may be the source of the observed deformation-induced softening. Sometimes, this dilatation is manifested as a decrease in the specimen density [27], but in this study we did not observe such a change [Fig. 3-10 (a)], either because our density measurements were not sensitive enough or because the dilation was highly localized in the shear bands and not detectable in an "average" measurement. Others have performed microstructural analysis of plastically deformed BMGs and shown that there is indeed an increase in free volume relative to the undeformed glass [28-32].

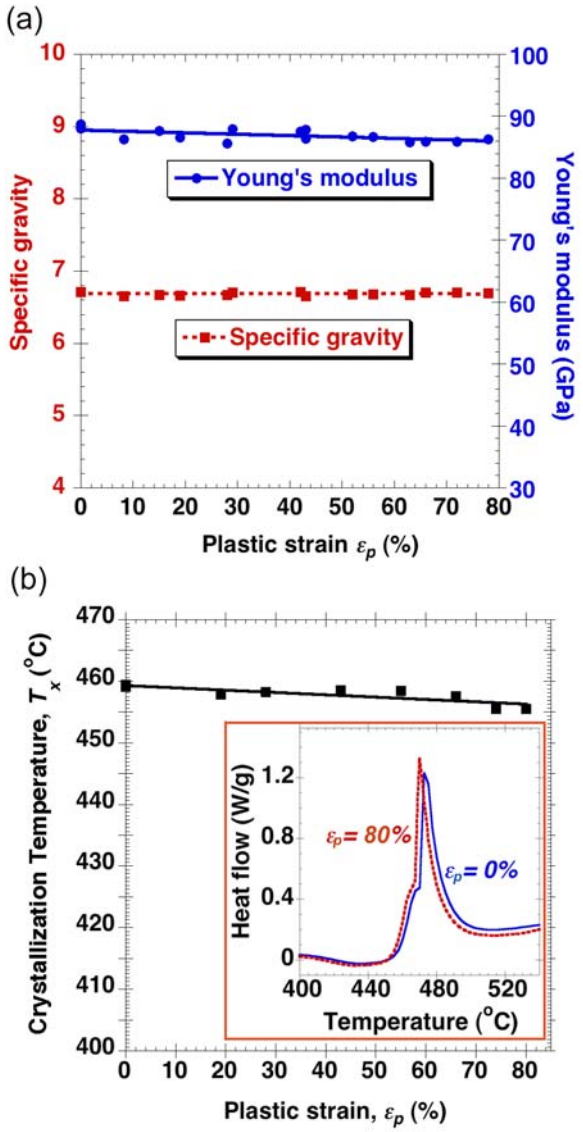

Figure 3-10. (a) Young's modulus decreases slightly with increasing plastic strain, but specific gravity remains unchanged, (b) Crystallization temperature decreases slightly with increasing plastic strain.

3.2 Indentation induced shear bands

3.2.1 Shear band behavior around Vickers indents

Figure 3-11(a) shows a typical image of a 1000g Vickers indent in the as-cast sample, indicating a regular indentation impression and incomplete circular shear bands along with the pile-ups. A laser profilometer line scan analysis from A to B, in Fig. 3-11(b), shows the obvious pile-ups, about 24% of the indentation penetration, around the edges of the indent.

3.2.2 Shear band morphology underneath Vickers indent

Figure 3-12 shows shear band morphology beneath a Vickers indent (1000g load) in the as-cast sample when the interface is parallel to the indenter diagonal. There are two sets of shear bands: semi-circular shear bands and radial shear bands. Semi-circular shear bands have higher density, and spread through the whole plastic deformation zone (~ 40μm), as shown in Fig. 3-12(a). Radial shear bands have relatively low density, intersect the semi-circular shear bands, and produce shear-offset steps on the semi-circular bands indicating that they were formed later, as shown in Fig. 3-12(b). It is also noted that the value of shear-offset decreases with increasing distance away from the indenter tip, which suggests that the radial bands propagate away from the indenter tip. The higher magnification image clearly shows that those semi-circular shear bands that are not intersected by radial bands are continuous and smooth [Fig. 3-12(c)]. The spacing between adjacent semi-circular shear bands was found to linearly increase with increasing distance from the tip of the indenter, as plotted in Fig. 3-12(d). The relation can be expressed by:

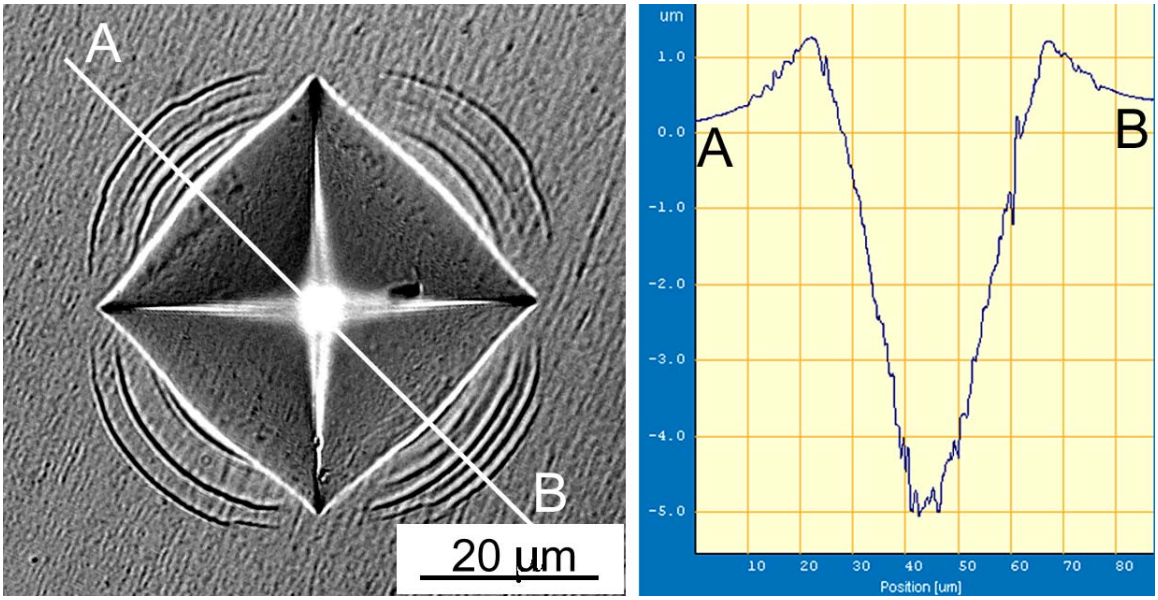

Figure 3-11. (a) Optical image showing shear bands around the perimeter of a Vickers indent and (b) the corresponding height profiles along A→B in the as-cast sample.

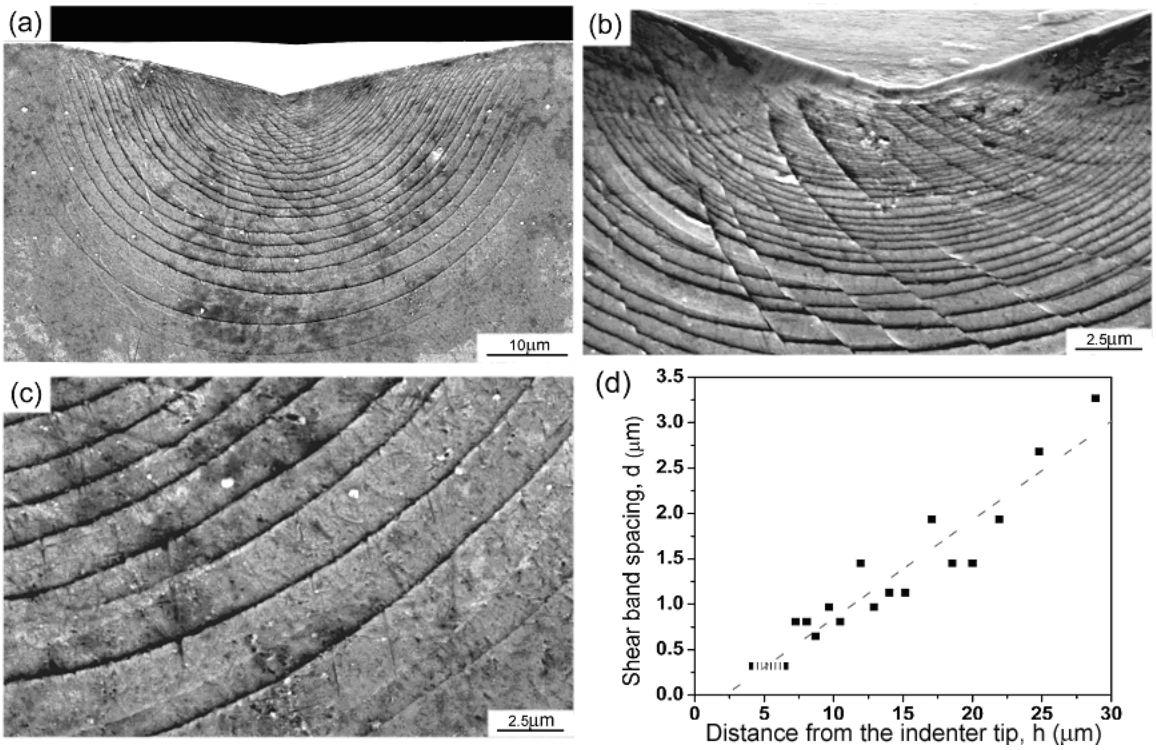

Figure 3-12. (a) Shear band morphology beneath a Vickers indent in the as-cast BMG when the interface is parallel to the indenter diagonal. Higher magnification images showing (b) radial shear bands around indenter tip intersecting the semi-circular shear bands, and (c) smooth semi-circular shear bands in regions without radial bands. The semi-circular shear band spacing increases with increasing distance from the indenter tip (d).

$$d = 0.11h - 0.24\,, \qquad (3\text{-}4)$$

where d is the shear band spacing (units of μm), and h is the distance from the indenter tip (units of μm). Note that neither the semi-circular nor the radial shear bands extend beyond the diagonal of the Vickers indent and reach the top surface of the specimen [Fig. 3-12(a)].

Figure 3-13 shows the shear band morphology beneath a Vickers indent (1000g load) when the interface is at 45° to the indenter diagonal. As before, high-density semi-circular bands appear in the whole plastic deformation zone (~ 40μm) [Fig. 3-13(a)] and low-density radial bands cut through the semi-circular bands [Fig. 3-13(b)]. Semi-circular shear bands are continuous and smooth in the regions without radial bands, as shown in the higher magnification image [Fig. 3-13(c)]. The spacing between semi-circular shear bands linearly increases with increasing distance from the tip of the indenter, as plotted in Fig. 3-13(d). The relation is similar to Equation (3-4), within the experimental error:

$$d = 0.11h + 0.04\,. \qquad (3\text{-}5)$$

However, both semi-circular and radial shear bands extend beyond the indentation impression, as indicated by white lines in Fig. 3-13(a), in contrast to Fig. 3-12(a) where no shear bands extend beyond the indentation impression.

Figure 3-14(a) and (b) are shear band patterns underneath an indent and its corresponding surface height profile, respectively. The surface height profile shows that the material is protruded out of plane and the height of the protrusion increases as one approaches the indenter. It implies that the interface acts as a free surface and allows plastic displacement of the material into the interface. However, the out-of-plane flow is

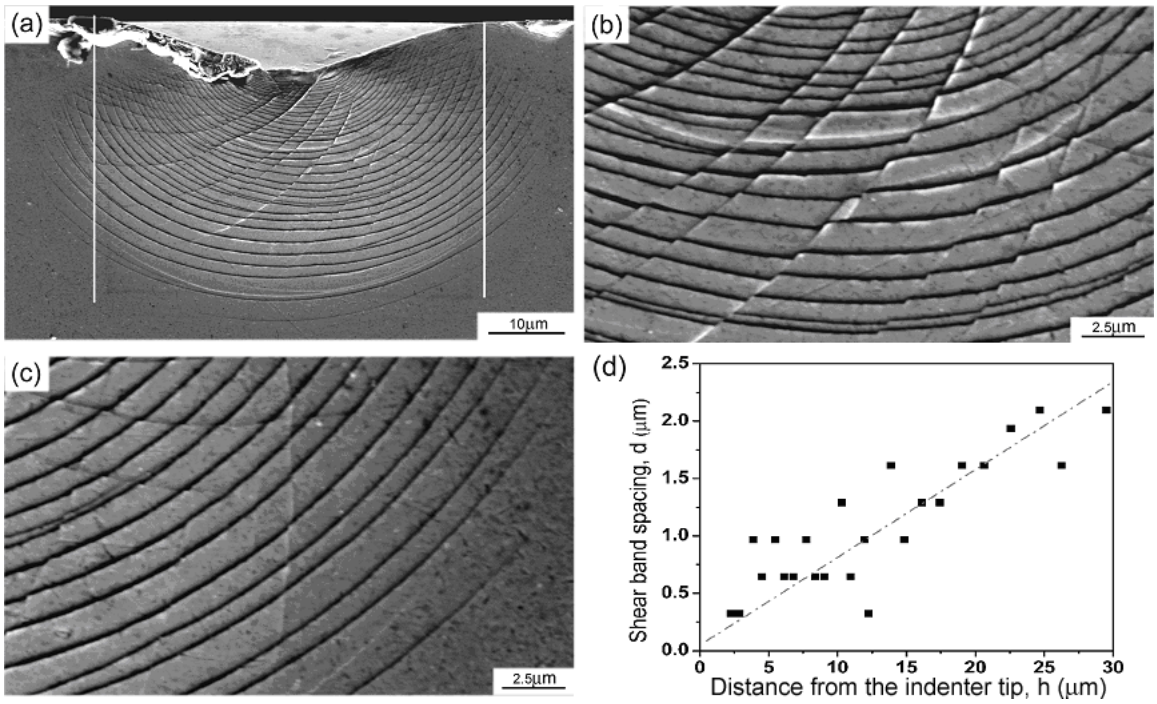

Figure 3-13. (a) Shear band morphology beneath a Vickers indent in the as-cast BMG when the interface is at 45° to the indenter diagonal. Higher magnification images showing (b) radial shear bands intersecting the semi-circular shear bands, and (c) smooth semi-circular shear bands in regions without radial bands. The semi-circular shear band spacing increases with increasing distance from the indenter tip (d).

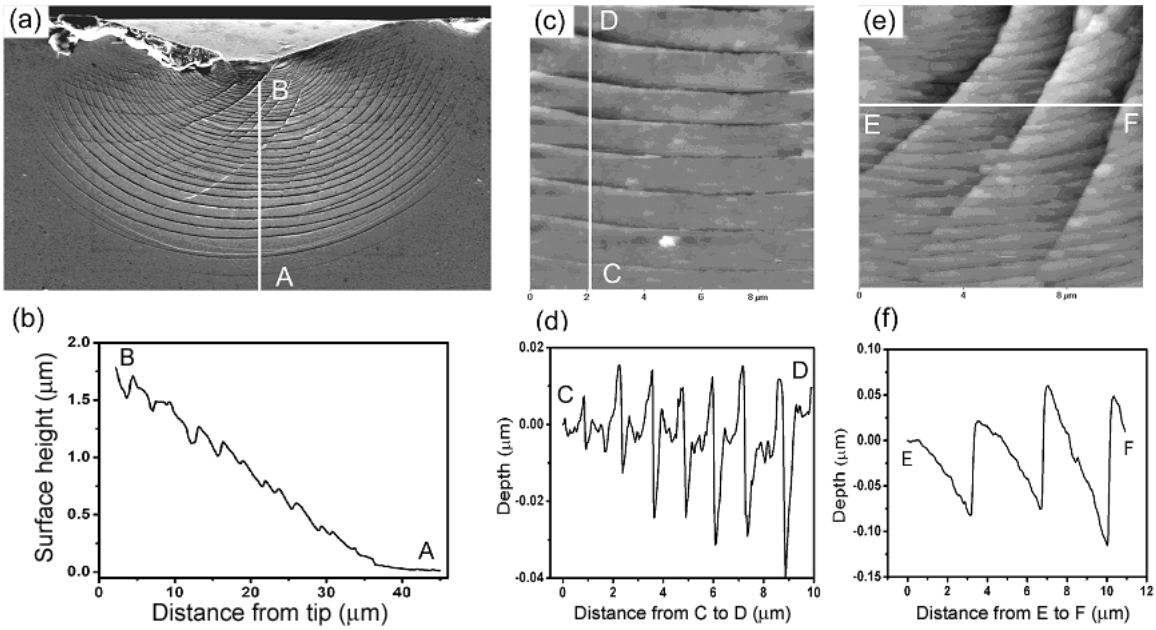

Figure 3-14. SEM/AFM images and AFM line scans showing the shear band patterns and topology beneath a Vickers indenter in the as-cast sample: (a) SEM image showing plastic zone and (b) the corresponding surface height profile from A to B indicating out-of-plane flow; (c) higher magnification AFM image showing smooth semi-circular shear bands and (d) the corresponding line scan from C to D revealing increasing out-of-plane displacement when shear bands are closer to the indenter tip; (e) AFM image showing radial shear bands and (f) the corresponding line scanning profile from E to F indicating the out-of-plane displacement of radial bands.

not homogeneous, but associated with localized shear steps, as evidenced by the serrated line-scan. Each serration corresponds to a shear band, similar to the serrations in stress-strain curves of compression tests and pop-in events in the loading curves of nanoindentation. Fig. 3-14(c) is a higher magnification AFM image of semi-circular shear bands, which has been flattened to better show the shear band features. Its AFM surface height [Fig. 3-14(d)] shows well the correspondence between shear bands and serrations. The step heights of the shear bands increase from ~ 0.01 μm to ~ 0.05 μm, as the indenter tip is approached from C to D. The thickness of the shear bands, if defined as the width of the shear band valley in Fig. 3-14(d), ranges from 150nm to 500nm, which is comparable with a recent report that the shear band thickness is in the range 200 ~ 1000nm (*3*). Similarly, the flattened AFM image of radial shear bands and the corresponding line scan are shown in Fig. 3-14(e) and (f), respectively. It can be seen that radial bands not only shift the semi-circular bands in plane, but also produce out-of-plane displacements.

In previous studies on metallic glasses with various compositions, pile-ups and slip-steps of shear bands were observed on the top surface surrounding the Vickers(*4-8*) and Berkovich (*9-11*) indents. Vaidyanthan et al. numerically simulated the location of local maximum effective stresses surrounding the Berkovich indent and found that it coincides with the location of the incomplete circular shear bands observed in the experiment. Similar pile-ups and shear-band steps were also found surrounding spherical indents (*12-14*).

In contrast to a few shear bands on the top surface, a large number of shear bands were observed underneath the indents (*4, 7, 8, 15*). The bonded interface technique was

widely used to bond two halves of samples in previous studies. In the current study, the clamped interface technique was chosen based on two considerations: (1) a relatively tighter bonding between the two halves can be obtained, as shown in Fig. 2-1; (2) our technique avoids the interaction between the adhesive and the sample in the bonded interface technique, which may affect the appearance of shear band patterns. SEM observations shown in Figs. 3-12 and 3-13 verified that semi-circular and radial shear bands obtained by our technique are much clearer than those obtained with the bonded interface techniques. It makes it possible to relate the shear bands on the top surface surrounding the indents and those underneath the indents, quantitatively study the shear band spacing and explore the interaction between semi-circular bands and radial bands. For a shear band appearing on the top surface, it has to propagate to the region beyond the indentation impression. Otherwise, they are under the indenter and invisible on the top surface. As shown in Fig. 3-13, the number of shear bands extending beyond the indentation impression is about 10, which is the maximum number of shear bands that can be observed on the top surface. In addition, some bands may not propagate to the top surface, as seen in the case of the clamped interface parallel to the indenter diagonal, Fig. 3-12(a). Therefore, only a few shear bands are visible on the top surface.

3.2.3 Plastic zone size underneath Vickers indent

The variation of the subsurface plastic zone size is plotted as a function of the square root of maximum load for the as-cast, pre-strained, and pre-strained plus annealed samples (Fig. 3-15). It can be seen that that plastic zone size is proportional to the square root of the maximum load:

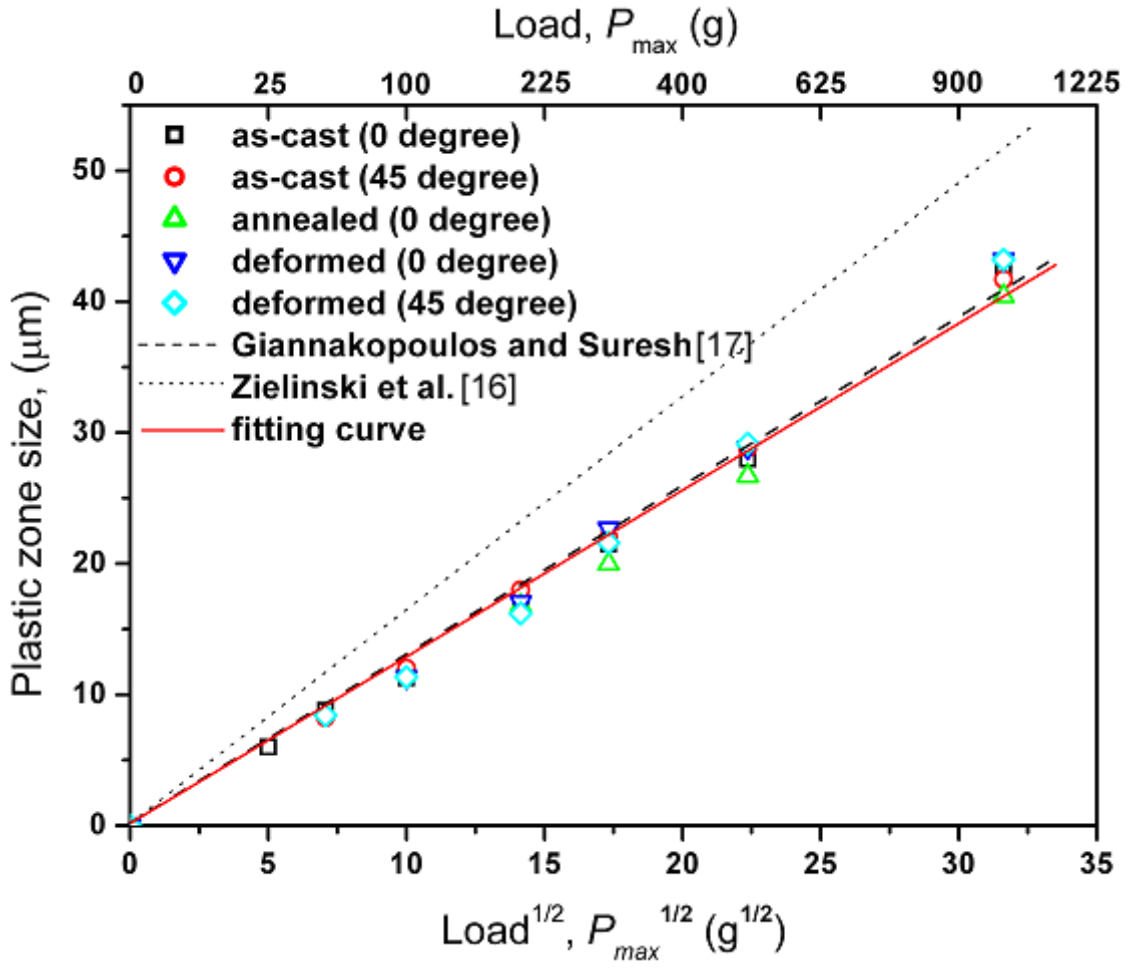

Figure 3-15. Plastic zone size underneath an indent increases linearly with the square root of the maximum load.

$$r_p = 1.27\sqrt{P_{\max}}, \qquad (3\text{-}6)$$

where r_p is plastic zone size, defined as the distance between the indenter's first contact point on the surface and the farthest shear band, $P_{\max}$ is the maximum load. The linear relation between r_p and $\sqrt{P_{\max}}$ has also been reported by Zielinski et al. (*16*) and Giannkopoulos et al. (*17*). Zielinski et al. (*16*) showed that in single crystal Fe-3 wt.% Si, the plastic zone size underneath a Vickers indenter is related to the maximum load by

$$r_p = \sqrt{(3P_{\max})/(2\pi\sigma_y)}, \qquad (3\text{-}7)$$

where r_p is obtained by measuring the size of the pile-up region, and σ_y is the yield strength. Giannkopoulos et al.(*17*) numerically simulated the elasto-plastic boundary underneath a sharp indenter, and showed that it has a hemi-spherical shape with a radius, i.e., plastic zone size, which can be expressed as:

$$r_p = \sqrt{(0.3P_{\max})/\sigma_y}, \qquad (3\text{-}8)$$

For comparison, Equation (3-7) and (3-8) are also plotted in Fig. 3-15 using a value of $\sigma_y = 1.77$ GPa (*18*). It can be seen that Equation (3-8) fits very well with our experimental data; however, Equation (3-7) overestimates the plastic zone size. Recently, Ramamurty et al. (*8*) reported that the plastic zone size (measured on both the top surface and the side interface) and the maximum load in a Pd-based metallic glass follow the $r_p \sim P_{\max}^{1/2}$ relation, comparable to our results.

Zhang et al. (*7*) also explored the r_p versus $P_{\max}$ relation in a Zr-based metallic glass, but used an analysis based on Johnson's expanding cavity model:

$$\frac{r_p^3}{a^3} = \frac{E}{6\sigma_y(1-\nu)}\tan\beta + \frac{2}{3}\frac{1-2\nu}{1-\nu}, \qquad (3\text{-}9)$$

where a is the radius of the contact area of a conical indenter, E is Young's modulus, ν is Poisson's ratio, and $\beta = 19.7^0$. In Zhang et al's study, the average Vickers hardness value $H_{average}$ was used to estimate the radius of indenter contact area a, i.e., $a = \sqrt{P_{\max}/(\pi H_{average})}$, which may be a source of deviation between the experimental data and the model because a slight decrease in hardness with increasing load is usually observed (*4, 7*). Therefore, in our present analyses, the radius of the contact area a at various loads was measured and transferred to the impression radius of the corresponding conical indenter. Figure 3-16 shows the ratio of the plastic zone radius (r_p) to the contact area radius of the corresponding conical indenter (a) at different applied loads. The r_p/a ratio calculated from Equation (3-9), i.e., $r_p/a = 1.7$, is also plotted in Fig.3-16. Comparing the experimental data and the calculated r_p/a ratio, it can be seen that although the expanding cavity model slightly overestimates r_p/a ratio at relatively low load (50g ~ 300g), our experimental data fit well with the calculation at loads of 500g and 1000g, indicating that Johnson's expanding cavity model may be useful in describing our samples' deformation behavior underneath the Vickers indenter at the loads of 500g and 1000g.

The slightly low experimental r_p/a ratio at low load but good match at high load may be explained as follows. In the expanding cavity model, it is assumed that the radial displacement of particles lying on the boundary $r = a$ during an increment of penetration

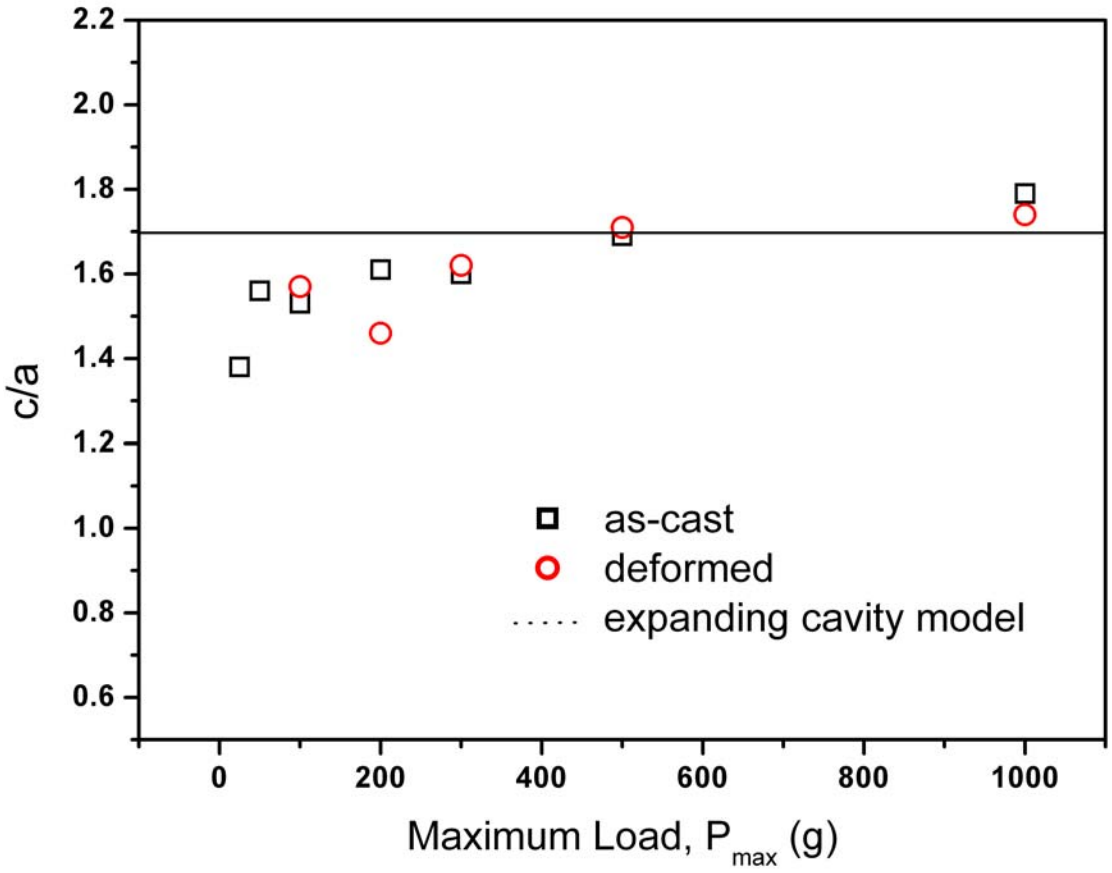

Figure 3-16. The ratio of plastic zone size to indent contact area is around 1.7 regardless of the applied load, consistent with the expanding cavity model.

dh must accommodate the volume of material displaced by the indenter (neglecting compressibility of the core). In our indentation experiments, the existence of a free surface on the top makes the material flow to the top and form pile-ups, as shown in Fig. 3-11. At the same time, the existence of a gap between the two clamped halves makes some material flow to the interface and form the protrusion, as shown in Fig. 3-14. That is, a fraction of the material volume is accommodated by the top free surface and the clamped interface. Therefore, for a given contact area radius, the radial displacement of particles lying on the $r = a$ boundary is smaller than what described in the model, leading to expanding cavity model overestimating the r_p / a ratio. With increasing applied load, the total material volume involved in the deformation increases and the relative fraction of material volume accommodated by the top free surface and the clamped interface decreases, resulting in a smaller error between the experimental data and the expanding cavity model.

3.2.4 Radial shear bands underneath Vickers indent

The above analyses of plastic zone size vs. contact radius ratio indicate that Johnson's expanding cavity model provides a reasonable description of the deformation of metallic glasses beneath a Vickers indent. Using this model, the stress distribution has been calculated (or simulated) and compared with shear band patterns by several researchers. For example, Zhang et al. (*7*), considering the Mohr-Coulomb yield criterion in metallic glasses, used the modified expanding cavity model to calculate the stress distribution underneath an indent. Their radial stress distribution fits well with the

morphology of semi-circular shear bands. However, the radial shear bands in the current study cannot be analyzed using the modified expanding cavity model as explained below.

(1) In the expanding cavity model, it is assumed that the contact surface of the indenter is encased in a hemi-spherical 'core' of radius a. However, in our experiments, the contact surface is the Vickers tip, which may result in a different stress distribution underneath the indenter and produce a deviation between the expanding cavity model and experimentally observed deformation patterns. To verify this possibility, the shear band patterns underneath a spherical indenter were examined, as shown in Fig. 3-17 (a). There are mainly semi-circular shear bands throughout the whole plastic deformation zone, along with a few radial shear bands, as shown in Fig. 3-17(b). The latter intersect the semi-circular bands, but produce no obvious shear offsets on the semi-circular bands. Comparing the radial bands under the spherical indenter with those under the Vickers indenter, the radial bands under the Vickers indenter spread across longer distances, and form obvious and large shear-offset steps. This indicates that the stress underneath a Vickers indenter favors the formation and propagation of radial shear bands.

(2) In the expanding cavity model, it is assumed that the stresses and displacements have radial symmetry and are the same as in an infinite elastic and perfectly plastic body, which contains a spherical cavity under a pressure. In the experiments, the radial symmetry is no longer satisfied due to the existence of the free top surface. A part of the material flows to the top surface, as shown in Fig. 3-2. The radial bands may be the traces of the material transported to the top, reminiscent of slip lines in the slip-field theory. Several researchers have used the slip-field theory to explain radial shear band patterns underneath the indent (*4, 19*). However, semi-circular shear bands cannot be

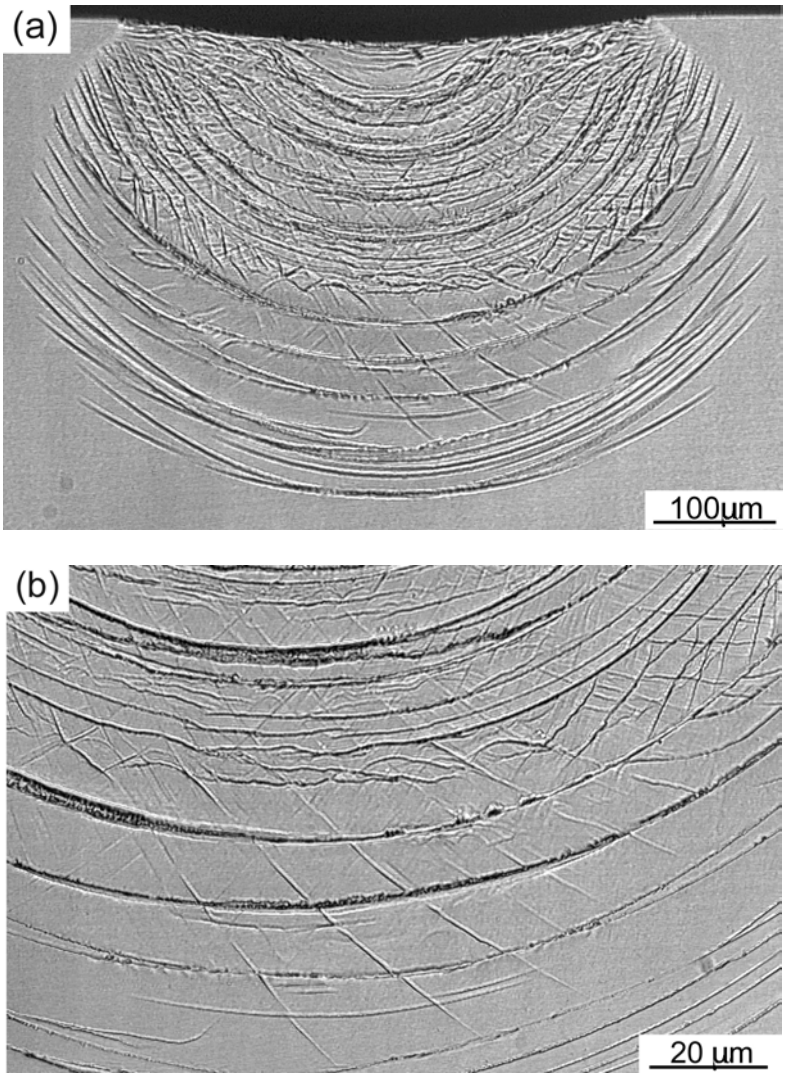

Figure 3-17. (a) Shear band morphology underneath a spherical indent and (b) higher magnification image showing radial and semi-circular bands.

explained by the slip-field theory. Therefore, shear band patterns underneath the Vickers indents cannot be explained by either model, due to the complicated stress distribution and the presence of the top free surface and interface in the experiments.

3.2.5 Softening caused by shear bands

A series of nanoindentation tests, as shown in Fig. 3-18, were made in the deformation zone underneath the Vickers indent using the MTS Nano-XP instrument, in order to study the hardness change in the deformation zone. Figure 3-19 shows the nano-hardness within and outside the plastic zone. The nano-hardness of the plastic zone is lower than that of the undeformed region. The hardness difference is ~13%, which is larger than the experimental scatter and comparable to the strain softening observed in metallic glasses plastically strained by constrained compression [Fig. 3-9]. Even within the plastic zone, the regions closer to the indenter tip, i.e., with smaller shear band spacing [as shown in Fig. 3-12(f)], are relatively softer than the regions away from the indenter tip, i.e., with larger shear band spacing [as shown in Fig. 3-12(f)]. This is also consistent with the relation between degree of softening and shear band spacing, i.e., the hardness decreases with decreasing shear band spacing [equation (3-4)].

3.3 Interaction between shear bands produced by compression and indentation

Figure 3-20(a) is the top-surface view of a Vickers indent in the 50% pre-strained sample. Compared with the as-cast specimen [Fig. 3-11(a)], the indent is slightly bigger, indicating the softening induced by the preceding compression, and the shear bands around the indent become irregular and convoluted. The line scan [Fig. 3-20(b)] shows that the pile-ups are about 12% of the indent depth, i.e. smaller than those is the as-cast

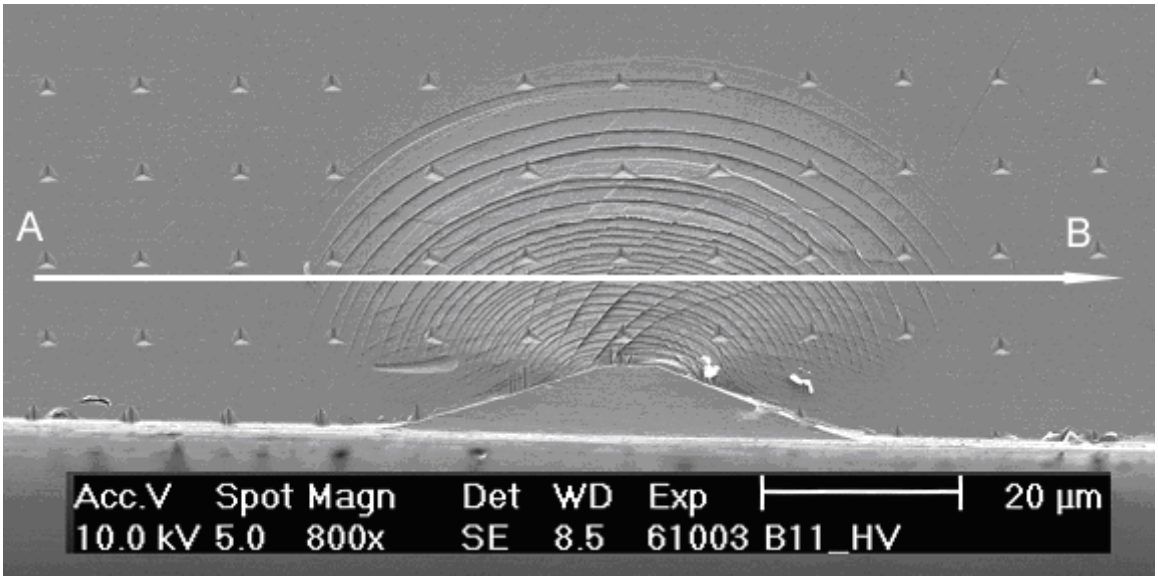

Figure 3-18. A series of nanoindents made in the plastic zone beneath a Vickers indent.

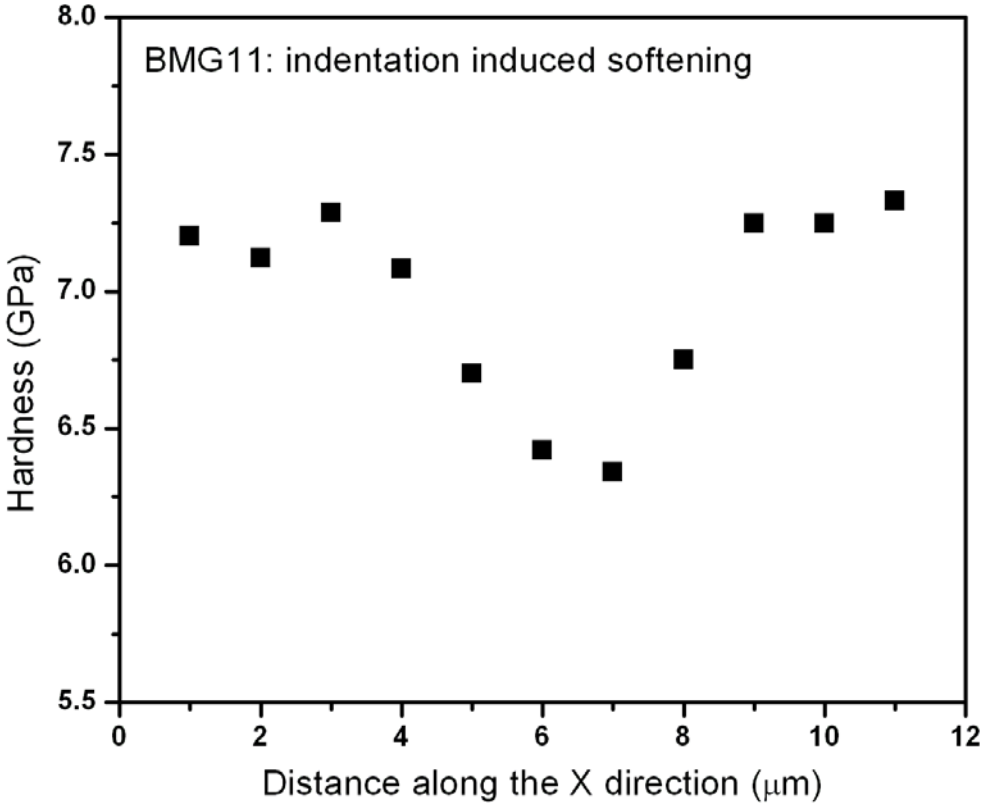

Figure 3-19. The plastic zone underneath a Vickers indent is softer than the unstrained region. Note: The first nano-indent starts on the left side of the Vickers indent in Fig. 3-18, and the X-direction corresponds to the left-to-right (A $\rightarrow$ B) direction in Fig. 3-18.

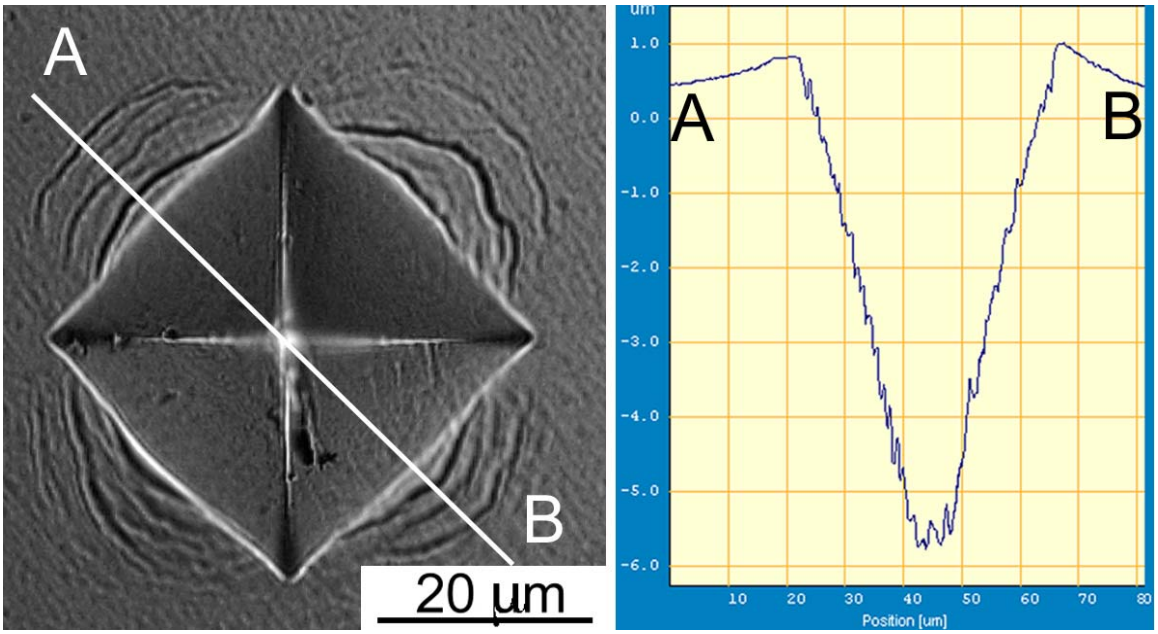

Figure 3-20. (a) Optical image showing irregular shear bands around the perimeter of a Vickers indent and (b) the corresponding height profiles along A→B in sample D50.

sample [Fig. 3-11(b)].

Typical shear band patterns beneath a Vickers indent in the 50% pre-strained sample are shown in Fig. 3-21. Shear bands do not extend beyond the diagonal of the Vickers indentation when the interface is parallel to the indenter diagonal. However, shear bands spread beyond the edge of the Vickers indentation impression when the interface is at 45° to the indenter diagonal. The plastic zone size is ~ 40 μm regardless of the orientation between the interface and the indenter diagonal, which is comparable to that in the as-cast sample (Figs. 3-12 and 3-13). A detailed examination reveals that, in some regions, both semi-circular and radial shear bands are generated, as shown in Fig. 3-21(c). However, some shear bands are wavy or even totally deviated from the semi-circular shape, as shown in Fig. 3-21(d), which is quite different from the smooth semi-circular shear bands seen throughout the whole plastic zone in the as-cast samples. Fig. 3-21(e) plots the variation of shear band spacing with distance from the tip of the indenter. It shows that the values of shear band spacing are more scattered than in the as-cast sample. Fig. 3-21(f) shows the line scan profile in the plastic zone from A to B in Fig. 3-21(b). It is seen that the material flows out of the plane, and in the region closer to the indenter tip, more material flows out. The serrations in the line scan indicate the inhomogeneous nature of plastic deformation in metallic glasses. Note that the wavy or convoluted bands are associated with bigger shear steps [pointed out by arrows in Fig. 3-21(f)] than smooth semi-circular bands.

Recently, several researchers showed that the pre-deformed metallic glasses exhibited smaller pile-ups and fewer shear bands surrounding the indents than the as-cast glass (*11, 14*). For example, pile-ups to a height of 37% of the indent depth were

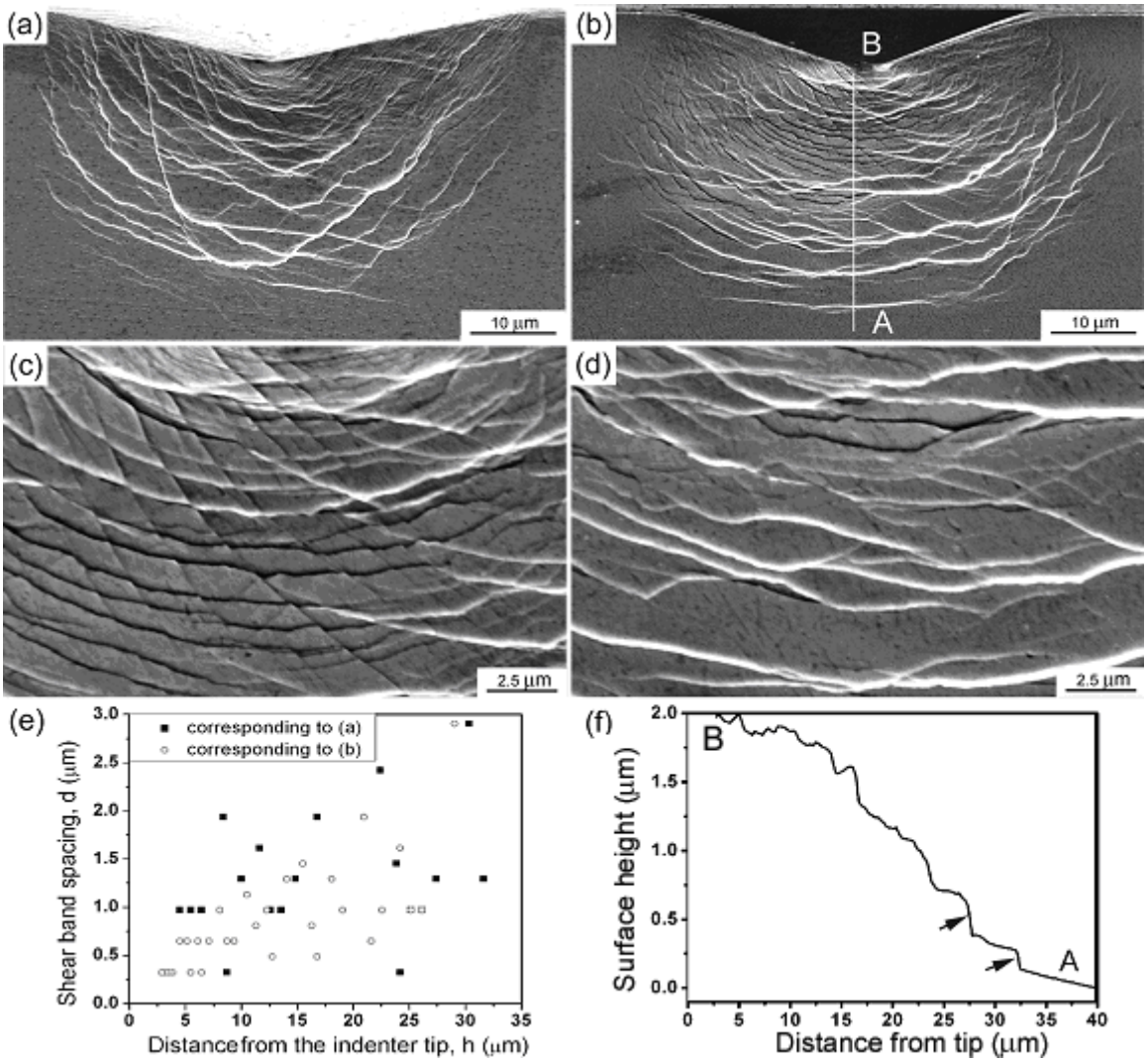

Figure 3-21. Shear band morphologies beneath a Vickers indent in the 50% plastically deformed BMG: (a) interface parallel to the indenter diagonal, (b) interface at 45° to the indenter diagonal, (c) higher magnification image showing the semi-circular and radial bands, and (d) higher magnification image showing the pre-existing shear bands reactivated during the indentation. (e) Variation of shear band spacing with distance from the indenter tip, and (f) the line scan profile from A to B in (b).

observed in as-spun $Al_{86.8}Ni_{3.7}Y_{9.5}$ metallic glass ribbon, whereas, the pile-up is only 12% of the indent depth after the ribbon was cold rolled to 44.5% reduction in thickness (*11*). This is consistent with our observations shown in Figs. 3-11 and 3-20, i.e., the smaller pile-ups were observed in the 50% pre-strained samples. Jiang et al.(*11*) attributed the smaller pile-ups in the rolled sample to few new shear bands being generated during indentation and the predominant deformation mode being accommodation by the pre-existing shear bands produced during rolling; however, no direct experimental evidence was presented. Our examination of shear band morphologies beneath the indents in the pre-strained sample [Fig. 3-19] revealed that, besides the propagation of pre-existing shear bands, high density of new semi-circular bands and several radial bands are also generated, indicating that newly generated bands also play an important role in accommodating the deformation, in contrast to Jiang et al.'s suggestion.

The wavy or convoluted shear bands in the pre-strained samples appear to be a mixture of the shear bands produced during pre-straining by uniaxial compression [Fig. 3-22 (c)] and those in virgin material [Fig. 3-22 (a)]. The reason for the irregular shape is that the shear bands in the pre-strained glass cannot simply follow the maximum stress contours because they tend to get diverted along some of the preexisting shear bands which are softer (*20*) and have a different geometry [rectangular grids, Fig. 3-22 (c)]. Preexisting shear bands have previously been shown to be preferred locations at which subsequent deformation occurs (*21*). However, only a few of the pre-existing bands, rather than the whole net-shaped pattern, are reactivated during the subsequent indentation. This is due to the competition between pre-existing bands and newly generated bands. If the stress at any location exceeds the critical resolved shear stress,

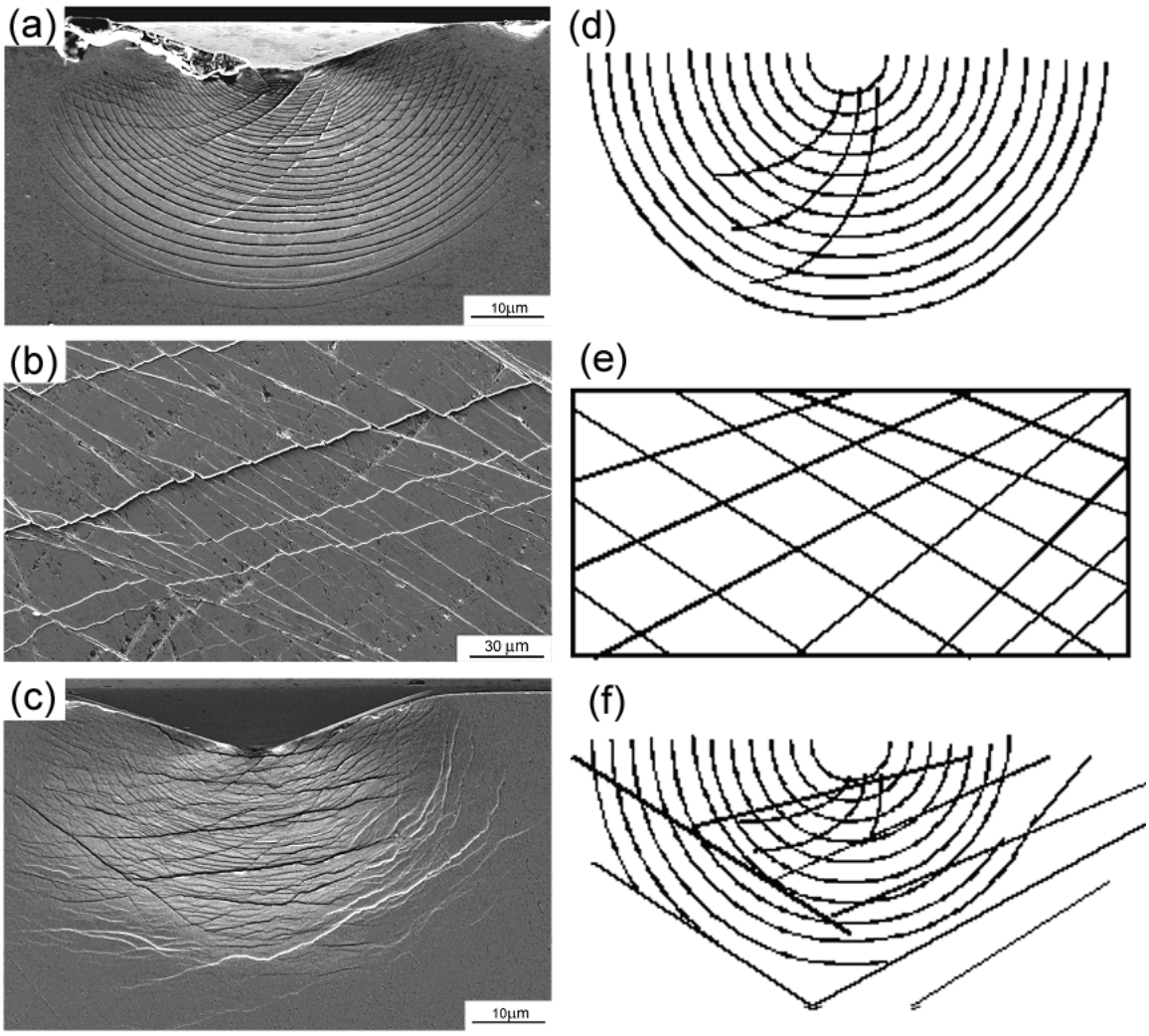

Figure 3-22. Shear bands underneath a Vickers indenter (1000 g load): (a) semi-circular and radial bands in as-cast glass; (b) Rectangular grid-shaped shear bands on the side surface of a uniaxially compressed specimen (50% strain); (c) irregular, convoluted shear bands in deformed glass (50% uniaxial compressive strain). Sketches in (d), (e) and (f) illustrate schematically the shear band patterns shown in (a), (b) and (c).

shear bands will be generated or reactivated whether there is a pre-existing band there or not. As the pre-existing bands are the weaker layers (*20*), they are easier to be deformed than virgin material at the same stress. However, since the maximum stress distribution underneath the indent is not along the pre-existing bands (*7*), most pre-existing bands cannot be reactivated even though they are weaker. That is, only portions of pre-existing bands, where the stress exceeds their resolved shear stress, are reactivated during the subsequent indentation.

3.4 Conclusions

By controlling the specimen aspect ratio and strain rate, compressive strains as high as 80% were obtained in an otherwise brittle metallic glass. Profuse shear banding was observed. Statistical analyses showed that the average angle between different groups of shear bands decreases with increasing plastic strain. Shear band density linearly increases with increasing plastic strain, i.e., shear band spacing is inversely proportional to plastic strain. The average shear offset per shear band is ~ 4.5 μm regardless of plastic strain, which is comparable to the calculated shear offset value from the $\rho \sim \varepsilon_p$ relation.

In compressively strained glasses, a systematic strain-induced softening was observed which contrasts sharply with the hardening typically observed in crystalline metals. If the deformed glass is treated as a composite of hard amorphous grains surrounded by soft shear-band boundaries, analogous to nanocrystalline materials that exhibit inverse Hall-Petch behavior, the correct functional form for the dependence of hardness on shear band spacing is obtained.

Plastic strain and multiple shear bands were also obtained by indentation. Incomplete circular shear bands were observed along with pile-ups on the top surfaces. Underneath the indent, semi-circular shear bands induced by the plane stress, spread through the whole plastic zone. The shear band spacing linearly increases with increasing distance from the tip of the indenter. Radial shear bands intersect semi-circular bands, resulting in shear offsets that decrease away from the indenter tip. The expanding cavity model can be used to describe the appearance of semi-circular bands but not radial bands.

Nanoindentation results reveal that the hardness in the plastic zone is lower than in the undeformed region. Even within the plastic zone, the region closer to the indenter tip, i.e., with smaller shear band spacing are softer than the region away from the indenter tip, i.e., with larger shear band spacing. This is consistent with the relation obtained between degree of softening and shear band spacing, i.e., the hardness decreases with decreasing shear band spacing. Deformation-induced softening leads naturally to shear localization and brittle fracture in unconstrained conditions.

The strain softening was correlated with shear band patterns around/underneath Vickers indents. Shear bands in the pre-strained glass were irregular and convoluted, and appear to be a mixture of shear bands produced during the preceding compression and those in as-cast glass. This indicates that shear band regions are softer than the surrounding undeformed matrix and act as preferred sites for subsequent deformation during indentation, consistent with the macroscopic strain softening observed after plastic deformation.

References

1. D. Hull, *Introduction to dislocations*, 149 (1975).
2. Z. F. Zhang, G. He, H. Zhang, J. Eckert, *Scripta Mater.* **51**, 945 (2005).
3. J. J. Lewandowski, A. L. Greer, *Nature Mater.* **5** (2006).
4. S. Jana, U. Ramamurty, K. Chattopadhyay, Y. Kawamura, *Mater. Sci. Eng. A* **375-377**, 1191 (2004).
5. A. Inoue, B. L. Shen, H. Koshiba, H. Kato, A. R. Yavari, *Acta Mater.* **52**, 1631 (2004).
6. K. Hajlaoui, T. Benameur, G. Vaughan, A. R. Yavari, *Scripta Mater.* **51**, 843 (2004).
7. H. Zhang, X. Jing, G. Subhash, L. J. Kecskes, R. J. Dowding, *Acta Mater.* **53**, 3849-3859 (2005).
8. U. Ramamurty, S. Jana, Y. Kawamura, K. Chattopadhyay, *Acta Mater.* **53**, 705-717 (2005).
9. R. Vaidynathan, M. Dao, G. Ravichandran, S. Suresh, *Acta Mater.* **49**, 3781-3789 (2001).
10. J. J. Kim, Y. Choi, S. Suresh, A. S. Argon, *Science* **295**, 654 (2002).
11. W. H. Jiang, F. E. Pinkerton, M. Atzmon, *Acta Mater.* **53**, 3469-3477 (2005).
12. M. N. M. Patnaik, R. Narasimhan, U. Ramamurty, *Acta Mater.* **52**, 3335-3345 (2004).
13. P. E. Donovan, *J. Mater. Sci.* **24**, 523 (1989).
14. C. Tang, Y. Li, K. Y. Zeng, *Mater. Sci. Eng. A* **384**, 215 (2004).
15. C. Su, L. Anand, *Acta Mater.* **54**, 179-189 (2005).

16. W. Zielinski, H. Huang, W. W. Gerberich, *J. Mater. Res.* **8**, 1300-1310 (1993).

17. A. E. Giannakopoulos, S. Suresh, *Scripta Mater.* **40**, 1191-1198 (1998).

18. C. T. Liu *et al.*, *Metall. Mater. Trans.* **29A**, 1811-1820 (1999).

19. C. A. Schuh, T. G. Nieh, *J. Mater. Res.* **19**, 46-57 (2003).

20. H. Bei, S. Xie, E. P. George, *Phys. Rev. Lett.* **96**, 105503 (2006).

21. K. D. Krishnanand, R. W. Cahn, in *Scripta Mater.* (1975), vol. 9, pp. 1259-1261.

4 Annealing induced hardening and re-deformation induced reversible softening in a Zr-based metallic glass

4.1 Effect of annealing on shear band morphology

In crystalline metals, dislocations can be produced by plastic deformation and relaxed by subsequent annealing (*1*). In metallic glasses, profuse shear bands are generated during constrained compression, as described in section 3.1.2. So an obvious question is: could annealing relax these shear bands? To answer this question, 50% pre-strained $Zr_{52.5}Al_{10}Ti_5Cu_{17.9}Ni_{14.6}$ BMG were annealed in vacuum at 373 ~ 633K (all lower than T_g) and times to 24 hours, as described in Section 2.4. To reveal changes within the shear bands, these annealed samples were electro-chemically etched at 5V in a solution of 33 vol% dilute nitric acid in methanal (*2*).

Figure 4-1 shows the optical micrographs of sample D50, sample D50A373, and sample D50A473 after electroetching. Due to the preferential etching in shear bands, they exhibit lower contrast than the undeformed matrix. Comparing (a), (b) and (c), it is noted that the contrast difference between shear bands and the undeformed matrix decreases with increasing annealing temperature, which indicates structural relaxation of shear bands (i.e. shear bands tend to recover to the as-cast state).

As discussed before (Fig. 3-22), shear bands underneath the indent in the pre-strained sample can be treated as a mixture of the shear bands produced during pre-straining by uniaxial compression and those in virgin material. How about the shear bands underneath the indent in pre-strained/annealed samples?

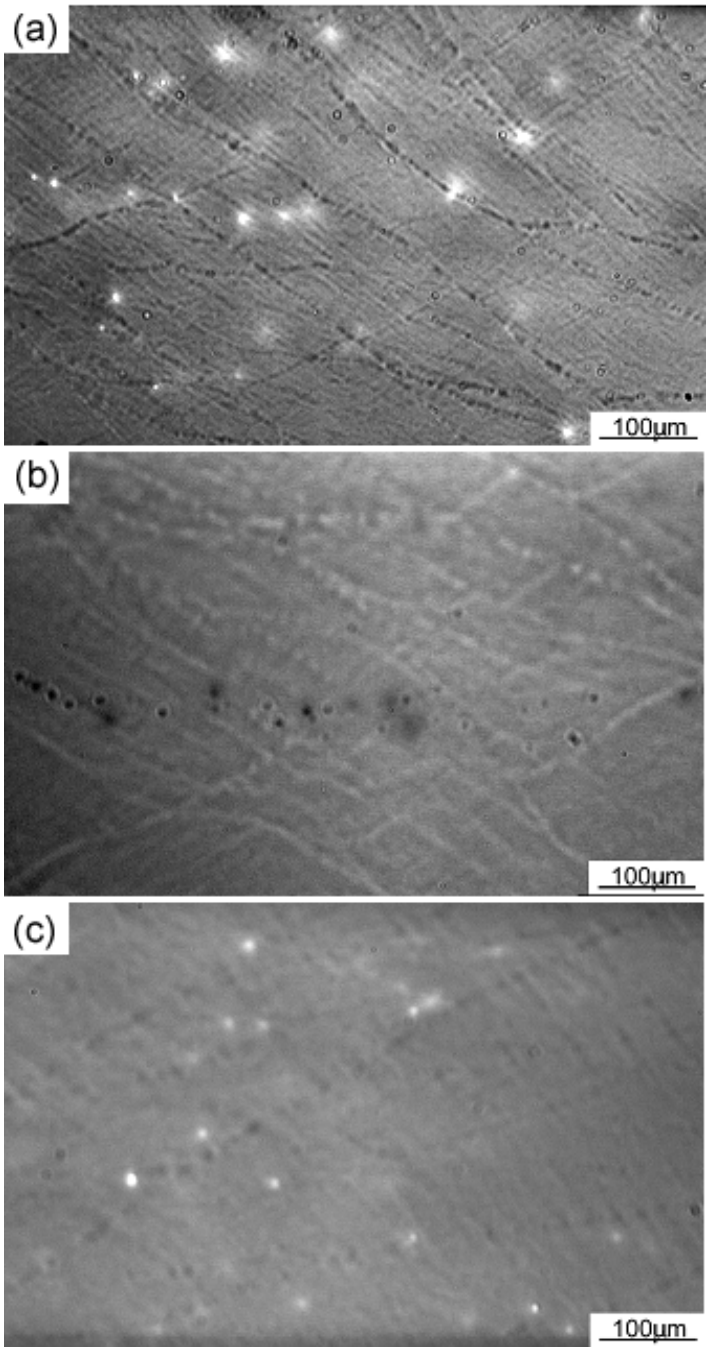

Figure 4-1. Preferential etching of shear bands in (a) sample D50, (b) sample D50A373, and (c) sample D50A473. The contrast between shear bands and undeformed matrix decreases with increasing annealing temperature.

Figure 4-2 is the top-surface view of a Vickers indent in sample D50A633. There

are smooth incomplete circular shear bands around the edges of the indent, similar to those in as-cast sample and no irregular bands were observed, as in the pre-strained samples. The height of the pile-ups recovers to a similar value as in the as-cast sample, ~ 25% of indent depth. Figure 4-3 shows shear band patterns beneath a Vickers indent in D50A373, D50A473, and D50A633. Irregular and convoluted shear bands were observed in both D50A373 and D50A473; the shear bands are more convoluted in sample D50A373 [Fig. 4-3(a)] than in sample D50A473 [Fig. 4-3(b)], indicating greater structural relaxation in shear bands after annealing at 473K compared to 373K. Figure 4-3(c-f) show shear band patterns in sample D50A633, which are remarkably similar to those in as-cast glass (Fig. 3-12 and 3-13): (1) there are semi-circular primary and radial secondary shear bands, which do not extend beyond the indentation impression on the top surface when the interface is parallel to the indenter diagonal [Fig. 4-3(c)], but extend beyond the indent impression when the interface is at 45° to the indenter diagonal [Fig. 4-3(d)]; (2) the plastic zone size is ~ 40 μm for both orientations, indicating a hemispherical plastic zone shape under the indenter; (3) the propagation of radial bands forms offset steps in the semi-circular bands [Fig. 4-3(e)]; (4) semi-circular bands are continuous and smooth if not cut by radial bands, as shown in Fig. 4-3(f). Comparing Figs. 4-1 and 4-3, it is noted that the lower contrast between shear bands and undeformed matrix correlate with the smoother shear bands underneath the indent.

A higher magnification image (Fig. 4-4) shows that a scratch (black arrows) in the deformation zone has not been displaced by the semi-circular shear bands, but is shifted by the radial bands. This indicates that the semi-circular shear bands are purely out of

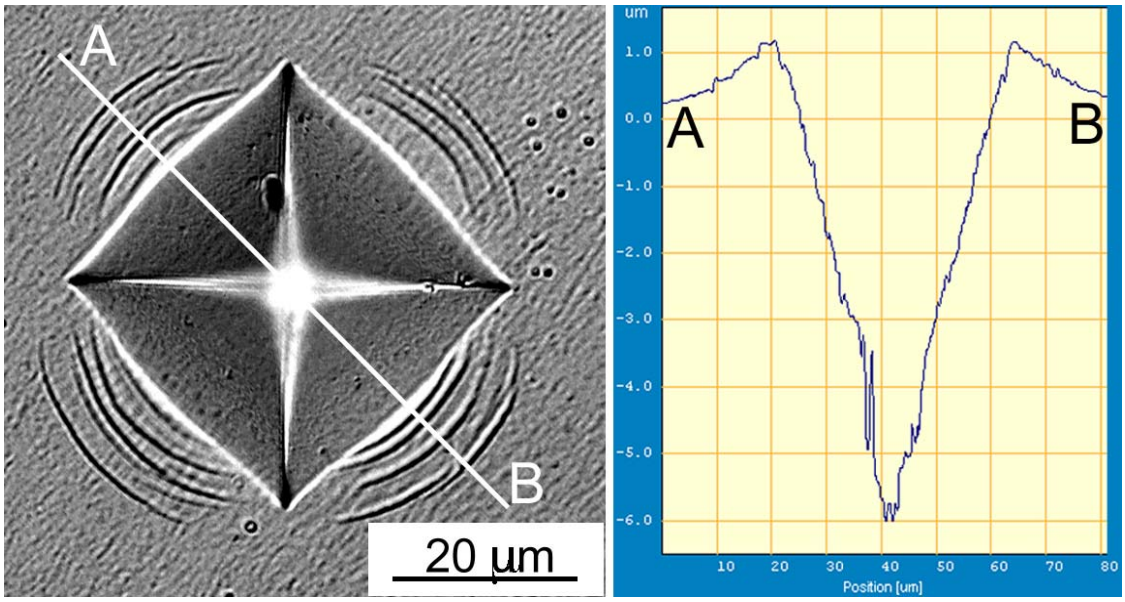

Figure 4-2. (a) Optical image showing circular shear bands recovered around the perimeter of a Vickers indent and (b) the corresponding height profiles along A→B in sample D50A633.

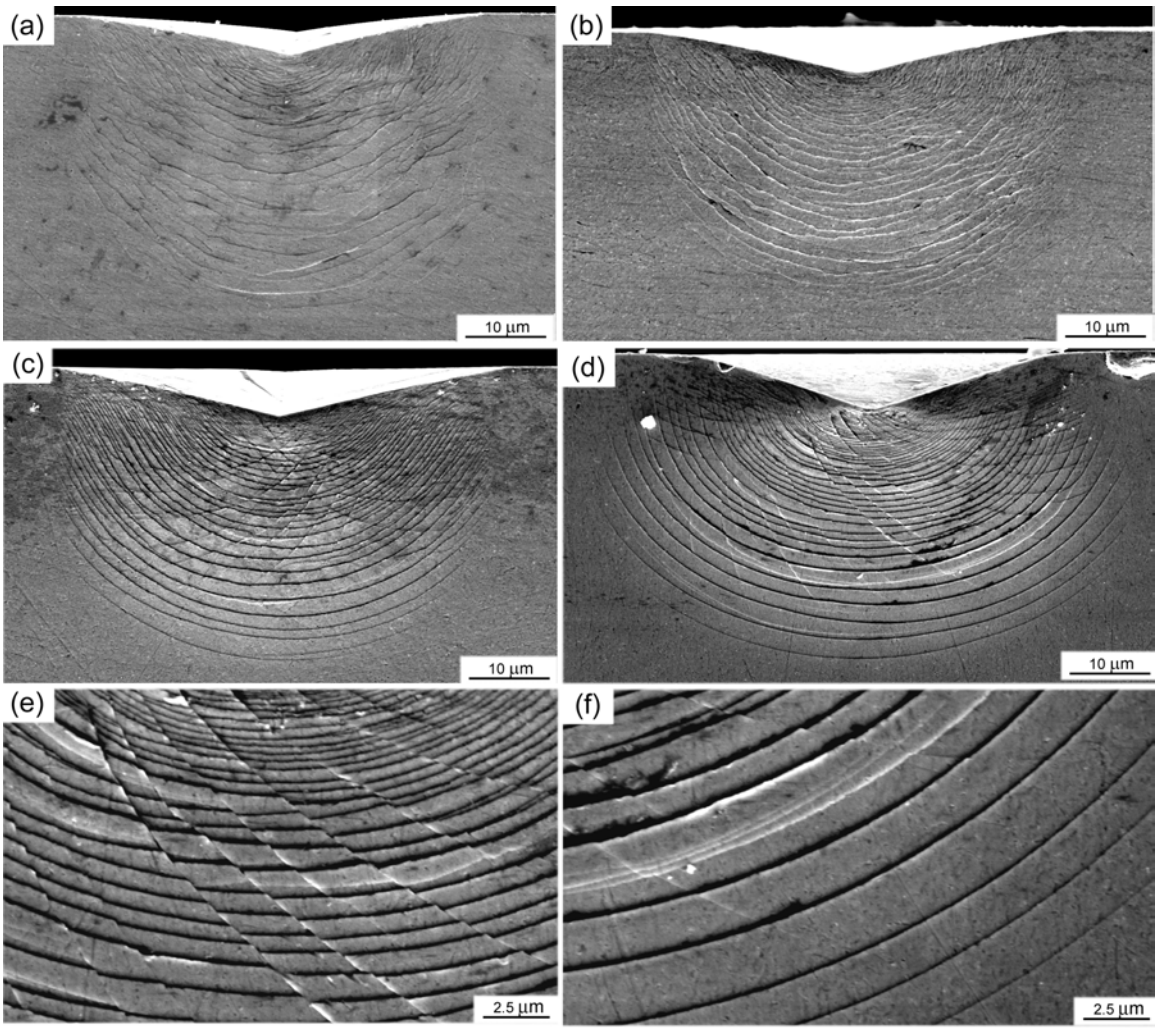

Figure 4-3. Shear band morphologies beneath a Vickers indent in (a) sample D50A373, (b) sample D50A473, (c) and (d) sample D50A633 with the interface parallel to the indenter diagonal and at 45° to the indenter diagonal, respectively, (e) higher magnification image showing the interaction between radial and semi-circular bands, and (f) smooth semi-circular bands in regions without radial bands.

plane shear displacements, i.e., the results of plane stress, which also is confirmed by AFM observations [Fig. 3-14(a) and (b)]. Radial bands have both the out-of-plane and in-plane displacements based on AFM and SEM observations.

4.2 Effect of annealing on mechanical properties

4.2.1 Effect of annealing on compressive strain to failure

Table 4-1 shows the effect of annealing time and temperature on compressive strain to failure of $Zr_{52.5}Al_{10}Ti_5Cu_{17.9}Ni_{14.6}$ bulk metallic glass with aspect ratio 0.5 at a strain rate of 1×10^{-3} s^{-1}. The compressive strain to failure decreases with increasing annealing time and temperature. A similar embrittlement was observed based on Charpy impact values, i.e., a loss of impact toughness with annealing (*3-5*), and it is thought that the reduction of free volume due to annealing is the primary mechanism responsible for the embrittlement (*5-9*). Therefore, the loss of compressive strain to failure may be also associated with the reduction of free volume.

4.2.2 Effect of annealing on hardness of pre-strained BMG

The effects of subsequent annealing on the hardness (*H*) of various strained samples are shown in Fig. 4-5, and compared to the hardness of deformed but not annealed BMG (square symbols). From section 3.1, we know that the hardness of plastically strained BMG can be expressed as a function of shear band spacing as follows:

$$H = H_g - A_1 \cdot \left(\frac{1}{d}\right), \qquad (4\text{-}1)$$

where T_g is the hardness of as-cast BMG, and A_1 is a proportionality constant equal to the softening induced by shear bands that are spaced 1 μm apart. Upon annealing, the

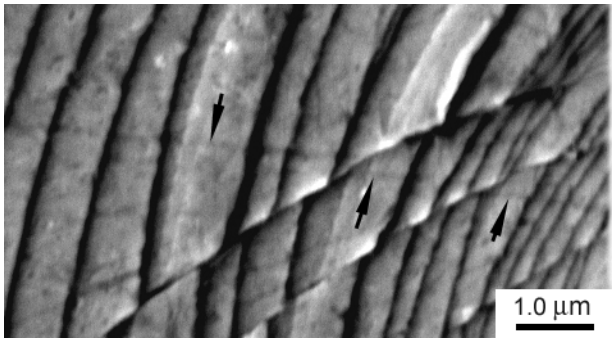

Figure 4-4. High magnification image showing a scratch (black arrows) not shifted by semi-circular bands, but shifted by radial bands, indicating that semi-circular bands have no in-plane displacement, but radial bands do.

Table 4-1. Effect of annealing on compressive strain to failure

Temperature / Annealing time	473K	573K	633K
2h	-	-	< 5%
4h	> 50%	~ 50%	-
16h	~ 50%	< 5%	-

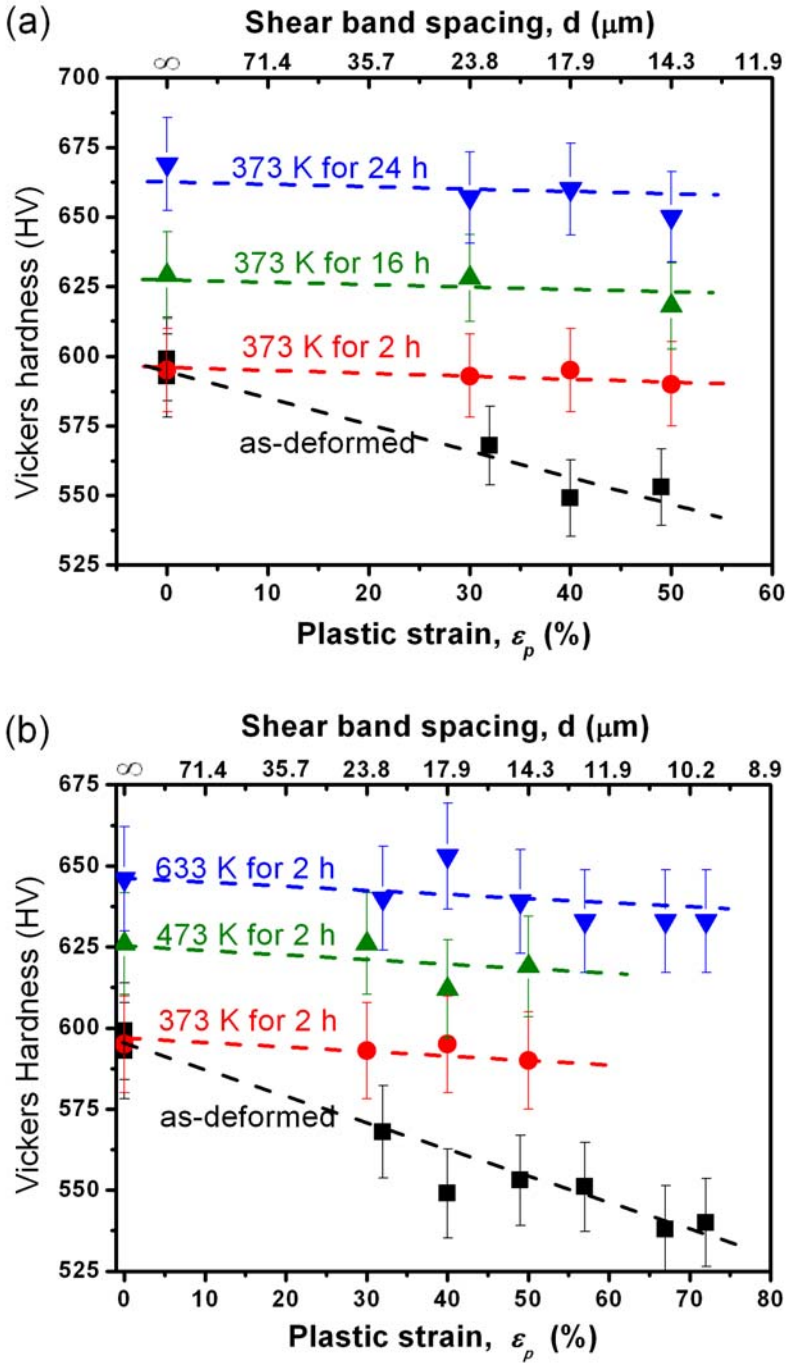

Figure 4-5. Effect of annealing on the Vickers hardness of $Zr_{52.5}Al_{10}Ti_5Cu_{17.9}Ni_{14.6}$ bulk metallic glass as a function of (a) time, and (b) temperature.

hardness of the deformed BMG increases, which may be expressed as follows:

$$H_{anneal} = H_{anneal\_0} - A_2 \cdot \left(\frac{1}{d}\right), \qquad (4\text{-}2)$$

where H_{anneal_0} is the hardness of the as-cast glass after annealing, and A_2 is a proportionality constant (as shown in Fig. 4-5, $A_1 > A_2$). Combining equations (1) and (2), the change in hardness upon annealing may be written as follows:

$$\Delta H = H_{anneal} - H = (H_{anneal\_0} - H_g) + (A_1 - A_2) \cdot \left(\frac{1}{d}\right). \quad (4\text{-}3)$$

After annealing at 373 K for 2 hours, $H_{anneal\_0} \approx H_g$ and, therefore, $\Delta H \propto \frac{1}{d}$. That is, hardness recovers much faster in the more heavily deformed specimens (containing closely spaced shear bands) than in the lightly deformed ones. The hardness recovery can occur at a relatively low temperature (373 K) compared to the T_g for this BMG (~663 K) and at rather short times (2 h). With increasing annealing time [Fig. 4-5 (a)], and temperature [Fig. 4-5 (b)], there is a further increase in H_{anneal_0}, but no substantial change in A_2. This means that shear band density of pre-strain have little effect on hardness in this regime, in contrast to the $\Delta H \propto \frac{1}{d}$ relation obtained for annealing at 373 K for 2 hours.

4.3 Free volume annihilation model

Figure 4-3 shows that shear bands underneath Vickers indents tend to recover smooth semi-circular shape after annealing, in general becoming smoother after

annealing at higher temperature. This recovery of shear band patterns is consistent with the annealing-induced hardness increase (Fig. 4-5). To better understand the relaxation of the pre-existing bands during annealing, free volume is chosen as a parameter to characterize the structural changes in shear bands. This does not rule out other structural changes that may occur such as short-range disordering. If the hardness recovery associated with annealing is related to the annihilation of free volume (*10*), then an obvious question is what causes the faster free volume annihilation in plastically deformed samples?

To answer this question, Spaepen's free volume annihilation model (*11*) is used here. In Spaepen's model, free volume annihilation is due to a diffusion process and the amount of free volume annihilated per second ($\Delta\upsilon$) is expressed as:

$$\Delta\upsilon = \frac{\upsilon^*}{n_D} N\gamma \exp(-\frac{\gamma\upsilon^*}{\upsilon_f}) \exp(-\frac{\Delta G}{kT}), \quad (4\text{-}4)$$

where $\frac{\upsilon^*}{n_D}$ is the amount of free volume annihilated per jump, υ^* is the atomic volume, n_D is the number of diffusion jumps needed to annihilate free volume equal to υ^*, $N\gamma \exp(-\frac{\gamma\upsilon^*}{\upsilon_f}) \exp(-\frac{\Delta G}{kT})$ is the number of jumps per second, N is the total number of atoms, γ is a geometry factor between 1 and ½, υ_f is the average free volume of an atom, ΔG is the activation energy for atomic motion, k is Boltzmann's constant, and T is the absolute temperature.

Since plastic deformation is highly localized in shear bands, we assume that: (1)

the free volume created during plastic deformation is concentrated in shear bands, which results in more free volume in shear bands than in the undeformed matrix, and (2) the free volume in the undeformed matrix is the same as that configurationally frozen in at T_g (*12*). Using parameters appropriate for shear-band regions, equation (4-4) yields the following expression for the amount of free volume annihilated per second in the shear bands:

$$\Delta\upsilon_{sb} = \frac{\upsilon^*}{n_D} N_{sb}\, \gamma \exp(-\frac{\gamma\upsilon^*}{\upsilon_{f\_sb}}) \exp(-\frac{\Delta G_{sb}}{kT}), \qquad (4\text{-}5)$$

where the subscript "*sb*" refers to shear bands. In the above expression, N_{sb} = (number of atoms per unit volume in shear bands) × (total volume of shear bands), can be written as:

$$N_{sb} = V_{total} \cdot \left(\frac{t}{d}\right) \cdot \left(\frac{1}{\upsilon^* + \upsilon_{f\_sb}}\right), \qquad (4\text{-}6)$$

where V_{total} is the total volume of glass (shear bands plus undeformed matrix), $\frac{t}{d}$ is the volume fraction of shear bands, t is the average thickness of shear bands, d is the shear band spacing, and $\frac{1}{\upsilon^* + \upsilon_{f\_sb}}$ is the number of atoms per unit volume in shear bands. Similarly, the amount of free volume annihilated per second in the undeformed matrix $(\Delta\upsilon_m)$ is given by:

$$\Delta\upsilon_m = \frac{\upsilon^*}{n_D} N_m\, \gamma \exp(-\frac{\gamma\upsilon^*}{\upsilon_{f\_m}}) \exp(-\frac{\Delta G_m}{kT}), \qquad (4\text{-}7)$$

where the subscript "*m*" refers to the undeformed matrix. N_m is the number of atoms in the undeformed matrix and can be expressed as:

$$N_m = V_{total} \cdot \left(1 - \frac{t}{d}\right) \cdot \left(\frac{1}{\upsilon^* + \upsilon_{f\_m}}\right). \qquad (4\text{-}8)$$

Therefore, the total amount of free volume annihilated per second in plastically deformed samples ($\Delta\upsilon_{total}$) is given by:

$$\Delta\upsilon_{total} = \Delta\upsilon_{sb} + \Delta\upsilon_m$$

$$= \frac{\upsilon^*}{n_D} V_{total}\gamma\Bigg[\underbrace{\left(\frac{t}{d}\right)\cdot\left(\frac{1}{\upsilon^* + \upsilon_{f\_sb}}\right)\cdot\exp\left(-\frac{\gamma\upsilon^*}{\upsilon_{f\_sb}}\right)\cdot\exp\left(-\frac{\Delta G_{sb}{}^m}{kT}\right)}_{I}$$

$$+\underbrace{\left(1-\frac{t}{d}\right)\cdot\left(\frac{1}{\upsilon^* + \upsilon_{f\_m}}\right)\cdot\exp\left(-\frac{\gamma\upsilon^*}{\upsilon_{f\_m}}\right)\cdot\exp\left(-\frac{\Delta G_m{}^m}{kT}\right)}_{II}\Bigg]. \qquad (4\text{-}9)$$

Since we assumed that the free volume in the shear bands is greater than that in the undeformed matrix, i.e., $\upsilon_{f\_sb} > \upsilon_{f\_m}$, the activation energy for atomic motion (or free volume motion) in the shear bands is lower than that in the undeformed matrix (*13*), i.e., $\Delta G_{sb} < \Delta G_m$. The density of a plastically deformed metallic glass containing 1% by volume of shear bands (i. e., $\frac{t}{d} \approx 0.01$) was found to be lower than that of the undeformed glass (10.118 g/cm^3 vs. 10.132 g/cm^3) (*14*). Assuming that this density decrease is concentrated in the shear bands, and if $\frac{\gamma\upsilon^*}{\upsilon_{f\_m}} \approx 37.4$ (*11, 12*) and $\gamma = 1$, the excess free volume in the shear bands (υ_{f_sb}) relative to that in the undeformed matrix is: $\upsilon_{f\_sb} \approx 7.3\upsilon_{f\_m}$. Under these conditions, $\frac{\gamma\upsilon^*}{\upsilon_{f\_sb}} \approx 5.2$, making term *I* in equation (4-9)

much greater than term *II,* even if the contribution due to a lower activation energy (ΔG) in the shear bands is neglected. That is, the free volume annihilation rate in shear bands is much faster than in the undeformed matrix, analogous to the significantly enhanced diffusivity in dislocation cores and grain boundaries in crystalline materials (*15*). Moreover, the faster free volume annihilation is consistent with the studies on the diffusion coefficient: the more the structure of a given glass departs from a fully relaxed structure, the higher the diffusion coefficient (*16-19*). As the free volume is annihilated, υ_{f_sb} decreases, thus slowing down further annihilation. According to equation (4-9), the free volume annihilation rate increases approximately linearly with decrease in shear band spacing, resulting in faster free volume annihilation in severely deformed samples compared to less deformed ones. Note that hardness recovery [equation (4-3)] and free volume annihilation rate [equation (4-9)] have similar dependencies on shear band spacing (d), both inversely proportional to d, suggesting that their kinetics are closely related. However, the exact relation between hardness and free volume remains unknown.

The faster annihilation of free volume in shear bands will eventually result in similar free-volume densities in both shear bands and undeformed matrix, i.e., the eradication of pre-strain effects. This scenario is consistent with micrographs of shear bands observed underneath the indents [Fig. 4-3] and revealed by preferential etching [Fig. 4-1] in the deformed/annealed glasses. As shown in Fig. 4-1, the contrast between shear bands and undeformed matrix decreases with increasing annealing temperature leading eventually to a complete lack of preferential etching in sample D50A633 which was annealed at 633K.

4.4 Reversible softening caused by re-deformation

If the deformed/annealed metallic glass is plastically deformed again, is it possible to observe reversible softening? Table 4-2 shows the hardness change of metallic glasses after a deformation-annealing-deformation process. Sample D33A100D exhibits the same hardness value as sample D33 within experimental error. The degree of softening induced by subsequent deformation (decrease in hardness) in sample D33A200 is also comparable to that in the as-cast glass, i.e., ~5% for $\varepsilon_p = 33\%$. Therefore, both sets of data revealed reversible softening. To our knowledge, this is the first time that reversible softening in metallic glasses is reported.

Table 4-2. Hardness change of BMG11 after the deformation-annealing-deformation processes

Specimen	Hardness (HV)
as-cast	596
33% plastic strain	569
33% plastic strain + annealed at 373K for 2 hours	593
33% plastic strain + annealed at 373K for 2 hours + 33% plastic strain	567
33% plastic strain + annealed at 473K for 2 hours	627
33% plastic strain + annealed at 473K for 2 hours + 33% plastic strain	598

4.5 Conclusions

Plastically deformed crystalline metals usually soften when they are annealed. In contrast, when annealed below its glass transition, a plastically deformed amorphous metal becomes harder and the compressive strain to failure decreases with increasing annealing time and temperature. During annealing, hardness initially recovers more rapidly in heavily deformed specimens than in lightly deformed ones, at a rate that varies inversely as the shear band spacing. With increasing annealing time and temperature, hardness further increases, but at the same rate whether the samples are pre-strained or not. If the deformed and annealed metallic glass is plastically deformed again, reversible softening is observed. To our knowledge, this is the first time that such reversible softening in metallic glasses has been observed. These hardness changes were correlated with shear band patterns around and underneath a Vickers indent. Pile-ups and incomplete circular shear bands on the top surface recover after annealing. Shear bands produced during indentation in the deformed and annealed sample also tend to recover their originally semi-circular and radial shapes consistent with the hardness increase.

Based on Spaepen's free volume model, the structural relaxation upon annealing can be explained as follows: initially, the free volume annihilation rate per unit volume is faster in the shear bands than in the undeformed matrix; this faster free volume annihilation eventually results in similar free-volume densities in both shear bands and undeformed matrix, i.e., the eradication of pre-strain effects.

References

1. G. E. Dieter, *Mechanical Metallurgy (McGraw-Hill, New York)* (1986).
2. Y. Zhang, W. H. Wang, A. L. Greer, in *Nature Mater.* (2006), vol. 5, pp. 857.
3. U. Ramamurty, M. L. Lee, J. Basu, Y. Li, *Scripta Mater.* **47**, 107-111 (2002).
4. Y. Yokoyama *et al.*, *Mater. Trans.* **46**, 2755-2761 (2005).
5. P. Murali, U. Ramamurty, *Acta Mater.* **53**, 1467 (2005).
6. F. Spaepen, S. S. Tsao, T. W. Wu, Proceedings of the EPRI-Acta Metallurgica Workshop on Amorphous Metals and Semiconductors (USA: Pergamon Press, 1986).
7. F. Spaenen, A. I. Taub. L. FE, Ed., Amorphous metallic alloys (Butterworth, London, 1983).
8. T. W. Wu, F. Spaenen, Mechanical behavior of rapidly solidified metals (USA: The Metallurgical Society of AIME, 1986).
9. E. P. Barth, F. Spaepen, R. Bye, S. K. Das, *Acta Mater.* **45**, 423 (1997).
10. W. H. Jiang, F. E. Pinkerton, M. Atzmon, *Acta Mater.* **53**, 3469-3477 (2005).
11. F. Spaepen, *Acta Metall.* **25**, 407-415 (1975).
12. H. S. Chen, M. Goldstein, *J. Appl. Phys.* **43**, 1642 (1971).
13. A. Vandenbeukel, *Acta Metall. Mater.* **42**, 1273-1278 (1994).
14. R. W. Cahn, N. A. Pratten, M. G. Scott, H. R. Sinning, L. Leonardsson, *Mat. Res. Soc. Symp. Proc.* **28**, 241-252 (1984).
15. P. Shewmon, *diffusion in solids*, 191 (1989).
16. H. S. Chen, L. C. Kimerling, J. M. Poate, W. L. Brown, *Appl. Phys. Lett.* **32**, 461 (1978).

17. T. Masumoto, R. Maddin, *Mater. Sci. Eng.* **19**, 1 (1975).

18. G. C. Chi, H. S. Chen, C. E. Miller, *J. Appl. Phys.* **49**, 1715 (1978).

19. R. S. William, T. Egami, *Trans. on Magnetics* **12**, 927 (1976).

5 Profuse shear bands and softening induced by constrained deformation in $Cu_{60}Zr_{30}Ti_{10}$ BMG

In section 3.1.1 we showed that large plastic strain can be obtained by carefully controlling the aspect ratio and strain rate. Is this approach limited to just one glass composition? To answer this question, we performed constrained compression on another BMG, $Cu_{60}Zr_{30}Ti_{10}$.

5.1 Shear bands produced by constrained compression

Figure 5-1 shows the change in height of low-aspect-ratio $Cu_{60}Zr_{30}Ti_{10}$ metallic glass specimens after plastic straining at room temperature. It can be seen that $Cu_{60}Zr_{30}Ti_{10}$ metallic glass can be deformed to 75% plastic strain without failure. Therefore, severe plastic strain using constrained compression is not limited to just one glass composition ($Zr_{52.5}Al_{10}Ti_5Cu_{17.9}Ni_{14.6}$).

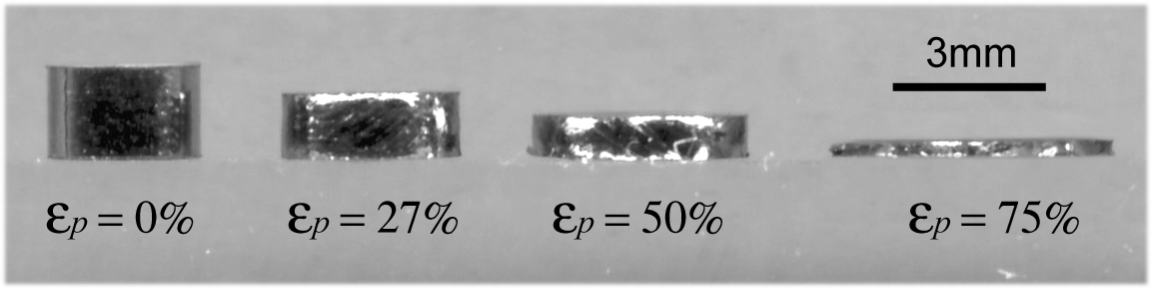

Figure 5-1. Change in height of 0.67-aspect-ratio $Cu_{60}Zr_{30}Ti_{10}$ metallic glass specimens after plastic straining at room temperature at a strain rate of 1×10^{-3} s^{-1}.

Figure 5-2 shows shear bands on a free surface parallel to the loading direction at (a) $\varepsilon_p = 27\%$ and (b) $\varepsilon_p = 50\%$. Depending on the orientation of shear bands, they can be roughly divided into two groups: one is at ~ 45° to the loading axis (45° shear bands), the other is approximately parallel to the loading axis (parallel shear bands). Most 45° shear bands are continuous; however, parallel shear bands are often displaced along the 45° shear bands at the sites where the two types of bands meet. With increasing plastic strain, the number of 45° shear bands increases rapidly, in contrast to the small increase in the number parallel shear bands. This is probably due to the fact that the parallel shear bands are generated relatively early in the deformation process, whereas the 45° shear bands are formed later.

In order to quantitatively characterize the multiplication of shear bands during deformation, the shear band density was measured as a function of the overall plastic strain. Figure 5-3 shows a linear increase in the density of shear bands with increasing strain:

$$\rho = 0.14\varepsilon_p, \text{ or } d^{-1} = 0.14\varepsilon_p, \qquad (5\text{-}1)$$

where ρ is the shear band density (units of μm), d is the shear band spacing, and ε_p is the plastic strain. From these results, the average shear offset per shear band is calculated to be 7 μm. For comparison, the shear offsets caused by the 45° shear bands on the parallel bands were measured and plotted as a statistical distribution, as shown in Fig. 5-4. It is interesting to note that average shear offset per shear band is ~ 4.5 μm regardless of plastic strains, which is in agreement with the linear $\rho \sim \varepsilon_p$ relation, and comparable to

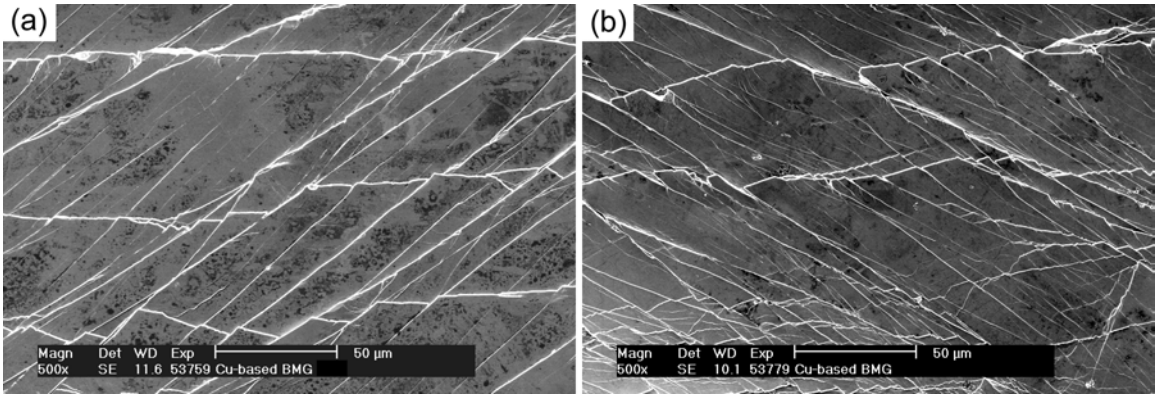

Figure 5-2. Typical shear band patterns on a free side surface parallel to the loading direction (a) $\varepsilon_p = 30\%$ and (b) $\varepsilon_p = 50\%$.

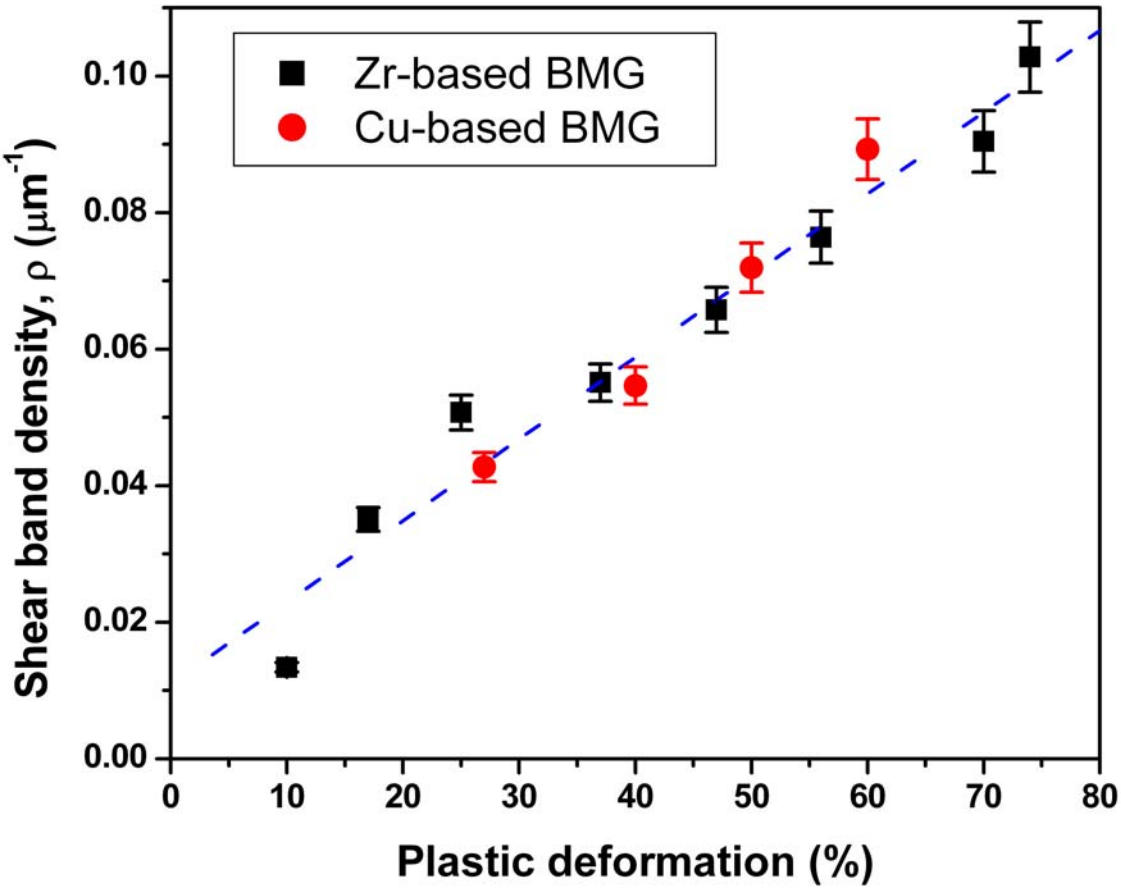

Figure 5-3. Linear increase in the shear band density with increasing plastic strain

the calculated shear offset.

5.2 Softening caused by profuse shear banding

Figure 5-5 shows that the hardness (at a load of 1000gf) decreases linearly with increasing plastic strain and decreasing shear band spacing. Analogous to the Zr-based metallic glass(*1*), these hardness values can be expressed as:

$$H = H_g - k_1\varepsilon_p \text{ or } H = H_g - k_2 / d\,, \qquad (5\text{-}2)$$

where H_g is the hardness of the undeformed glass. If the average thickness of shear bands is defined as t, the volume fraction of shear bands $V_{sb} = t/d$, and the volume fraction of undeformed matrix $V_g = 1 - V_{sb}$. Therefore, equation (2) may be rearranged as:

$$H = H_g V_g + (H_g - k_2 / t)V_{sb}\,, \qquad (5\text{-}3)$$

which indicates that the deformed metallic glasses can be assumed as a composite including two phases: shear bands with a hardness of $(H_g - k_2/t)$ and the surrounding undeformed matrix with a hardness of H_g. Since both k_2 and t are positive, regardless of their exact values, the hardness of shear bands will be lower than that of undeformed glass. As a result, plastic deformation, rather than spreading through the whole sample, will be localized in soft shear bands once these bands are formed, leading to catastrophic failure.

5.3 Shear band morphology around Vickers indent

The top-surface view of indents produced at a maximum load of 1000g in as-cast and 50% plastically strained samples are shown in Fig. 5-6(a) and (b), respectively.

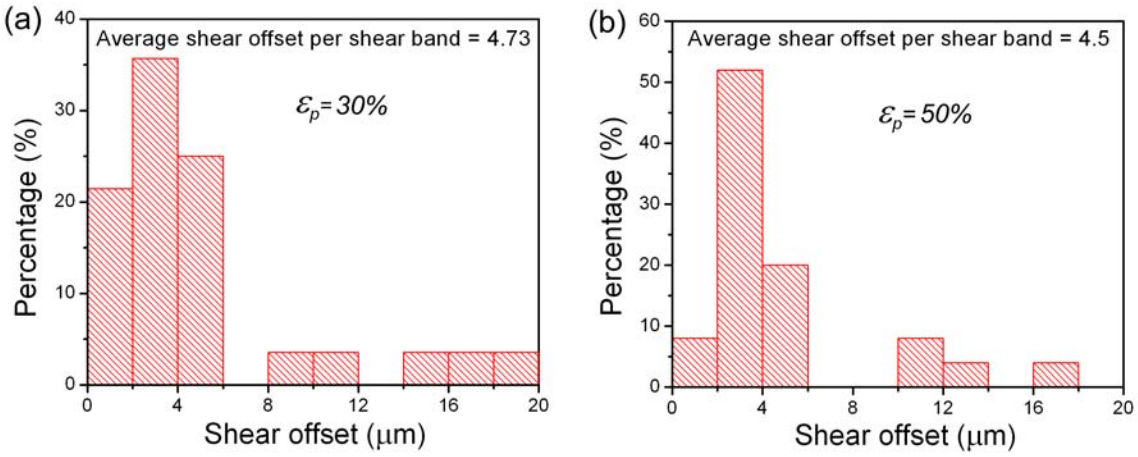

Figure 5-4. Statistical distribution of shear offset values: (a) $\varepsilon_p = 30\%$ and (b) $\varepsilon_p = 50\%$.

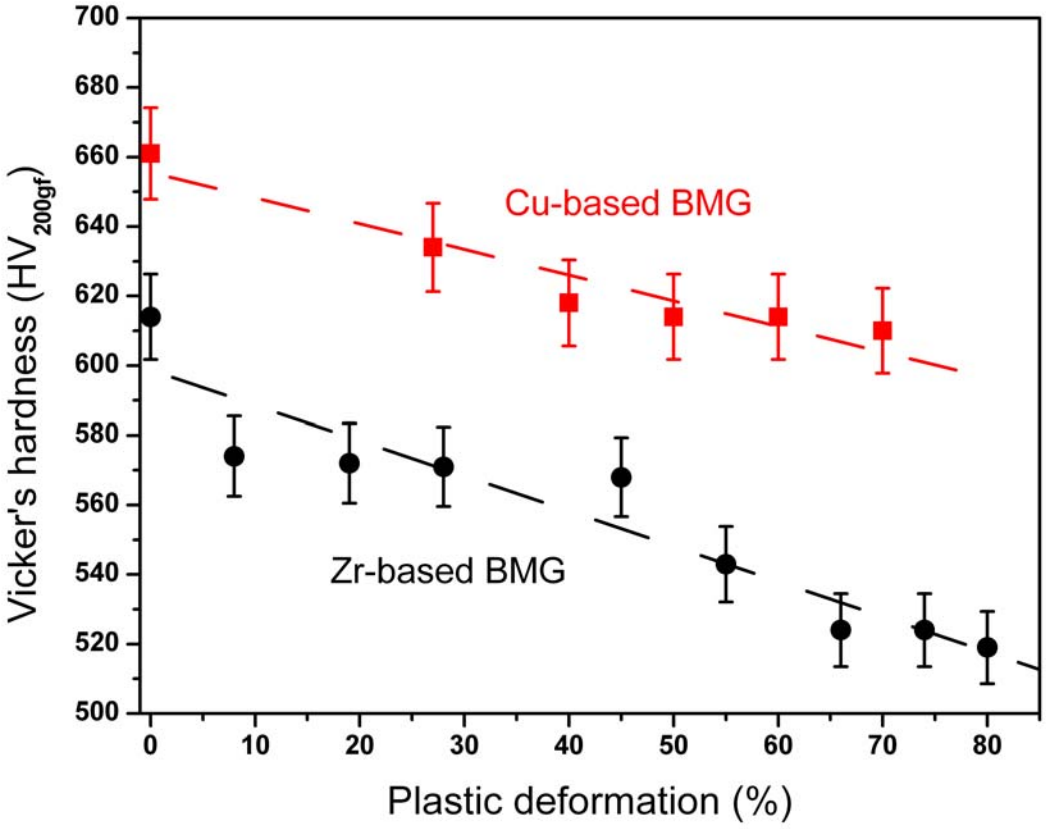

Figure 5-5. Decrease in hardness with increasing plastic strain.

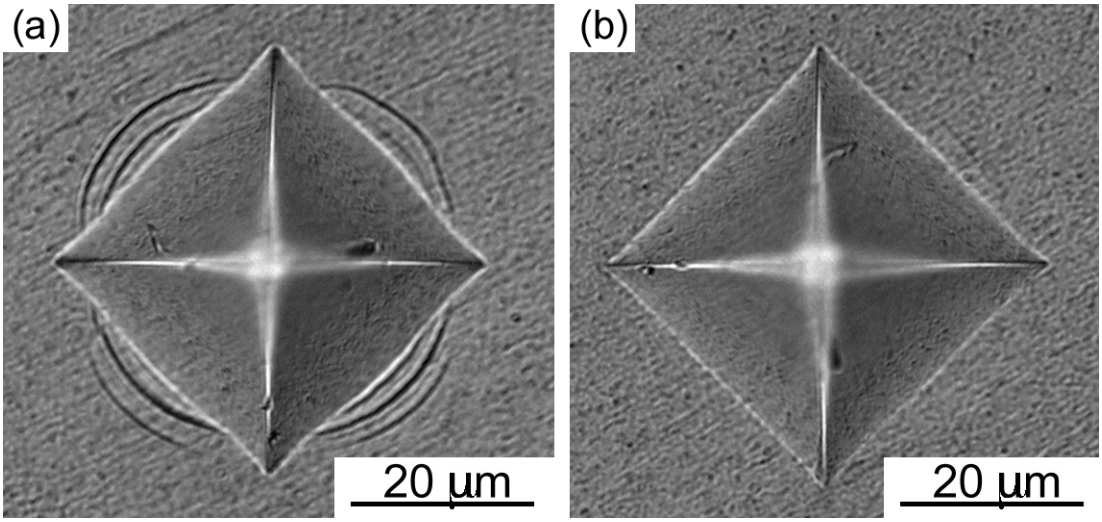

Figure 5-6. Vickers indent impressions at a maximum load of 1000g (a) in the as-cast sample, and (b) in the 50% pre-strained sample.

Semi-circular shear bands surrounding the indents are formed in the as-cast sample, in contrast to no shear bands in the 50% plastically strained sample.

Figure 5-7(a), (b), and (c) show typical shear band patterns underneath the indents in the as-cast sample at maximum loads of 50g, 200g, and 1000g, respectively, when the interface is parallel to the indenter diagonal. Plastic zone size increases with increasing maximum load. Semi-circular shear bands spread throughout the whole plastic zone, but no shear bands extend beyond the indent contact radius, a. Higher magnification image, Fig. 5-7(d), reveals that besides semi-circular shear bands, there are radial shear bands, which cut through the semi-circular bands, resulting in shear offsets on the semi-circular bands. This is analogous to the intersections between 45° and parallel shear bands during compression [Fig. 5-2], and indicates that the semi-circular bands were generated first. These shear offsets on the semi-circular bands decrease with increasing distance from the indenter tip, implying that the propagation direction of radial bands is away from the indenter. Fig. 5-7(e) is a line-scan profile from A to B in Fig. 5-7(c), showing the out-of-plane displacement in the plastic zone. Due to the presence of a non-rigid interface, the material flows into the interface, leading to the out-of-plane protrusion. The protrusion increases along the direction A$\rightarrow$B, but stabilizes at a value of $\sim 1.8\,\mu m$ (which is the half width of the interface gap) in the regions where a rigid constraint is provided by the other half of the sample. In addition, the protrusions are not smooth, as indicated by the serrations in the line-scan profile. These serrations are associated with the shear bands in Fig. 5-7(c), revealing the inhomogeneous nature of plastic deformation in metallic glasses. Other researchers have observed serrations, i.e., pop-in events, in the $P \sim h$ curves

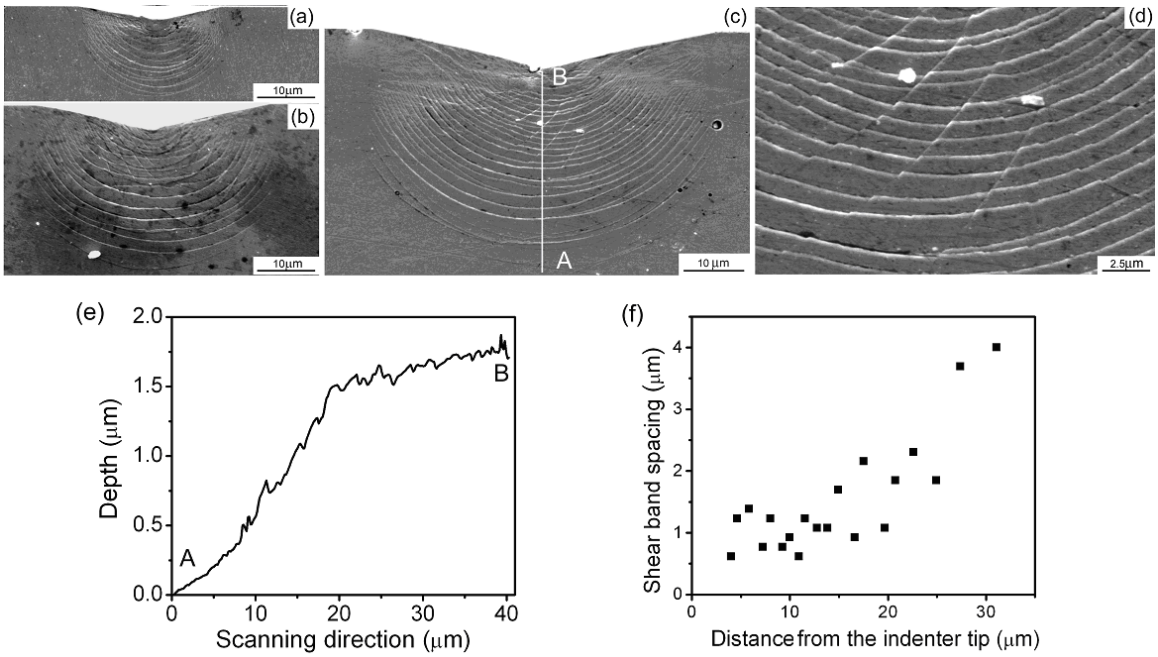

Figure 5-7. Shear band morphology beneath Vickers indents in as-cast Cu-based metallic glass at maximum loads of (a) 200g, (b) 500g, and (c) 1000g. (d) High magnification image showing semi-circular shear bands intersected by radial shear bands; (e) line scan profile from A to B in image (b); and (f) variation of shear band spacing with distance from the indenter tip.

obtained by nanoindentation and attributed them to the generation and propagation of shear bands (*3-5*). However, no direct experimental evidence has been presented to show the correspondence between shear bands and pop-in events, due to the difficulties in examining the plastic zone underneath the nano-indents.

Figure 5-8 plots the plastic zone size as a function of the square root of the maximum load. The relation can be expressed as:

$$r_p = 1.32 P_{\max}^{1/2}, \qquad (5\text{-}4)$$

where r_p is the plastic zone size and $P_{\max}$ is the maximum applied load. A similar $r_p \propto P_{\max}^{1/2}$ relation has also been observed in Zr- and Pd-based metallic glasses (*2, 6, 7*). The hemi-spherical plastic zone and semi-circular shear bands underneath the indents inspired some researchers to use the expanding cavity model to characterize the plastic zone size. In the expanding cavity model, the plastic zone is given by

$$\frac{r_p}{a} = \left[\frac{E}{6\sigma_y (1-\nu)} \tan\beta + \frac{2}{3} \frac{1-2\nu}{1-\nu} \right]^{1/3}, \qquad (5\text{-}5)$$

where a is the radius of conical indenter contact area, E is the Young's modulus, ν is the Poisson's ratio, and $\beta = 19.7^0$. For $Cu_{60}Zr_{30}Ti_{10}$ metallic glasses, $E = 114GPa$, $\sigma_y = 1.785GPa$ and $\nu = 0.35$, therefore, the right hand side of Equation (5-5) is equal to 1.83, which is plotted as a blue dashed line in Fig. 5-8. For comparison, the values of r_p at various maximum loads were directly measured. Because the Vickers indenter was used in the current study, a at various loads were obtained by measuring the diagonal of the contact area (a_v) and transforming a_v to the corresponding a. The values of the ratio

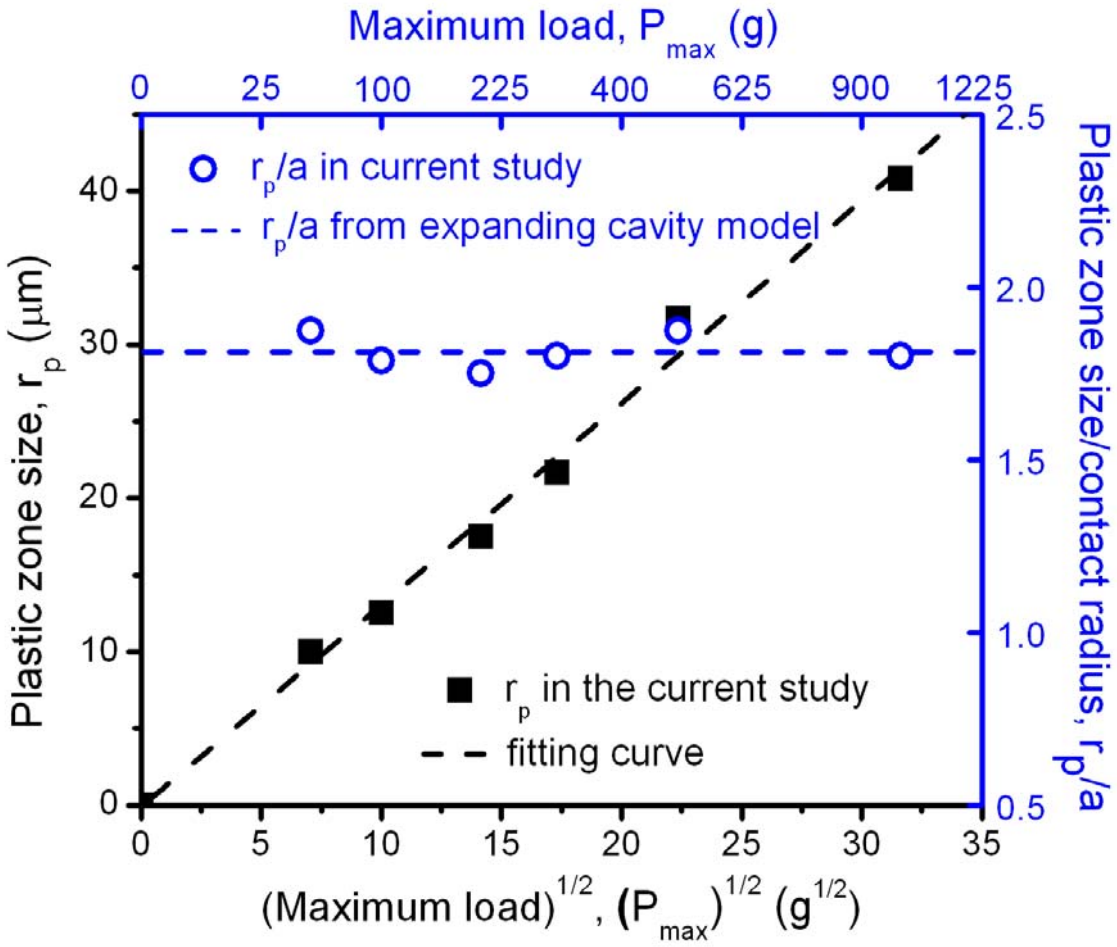

Figure 5-8. Plastic zone size underneath the indents increases linearly with increasing square root of the maximum load, however, the r_p / a ratio is around 1.83 regardless of the maximum load, comparable to the calculated value based on the expanding cavity model.

r_p / a, represented as open circles in Fig. 5-8, lie along the calculated value of 1.83. A similar behavior has also been observed in several Zr-based metallic glasses (*8*), indicating that the expanding cavity may provide a good description of the plastic zone underneath the indents in metallic glasses.

5.4 Softening caused by Vickers shear bands

Figure 5-9 shows the nano-hardness within and outside the plastic zone, and the inset shows the locations where nanoindentation tests were performed. The nano-hardness of the plastic zone is lower than that of the undeformed region. The hardness difference between these two regions is ~13%, which is larger than the experimental scatter and comparable to the strain softening observed in the plastically strained metallic glasses by constrained compression [Fig. 5-5]. Even within the plastic zone, the regions closer to the indenter tip, i.e., with smaller shear band spacing [as shown in Fig. 5-7(f)], are relatively softer than those far from the indenter tip, i.e., with larger shear band spacing [as shown in Fig. 5-7(f)]. This is also consistent with the observed relationship between degree of softening and shear band spacing, i.e., the hardness decreases with decreasing shear band spacing [equation (5-2)].

A similar softening induced by plastic deformation was also observed in Zr-(*9*), Al-(*10*), and Pd-based metallic glasses. Jiang et al. (*10*) attributed the softening to the presence of retained excess free volume after nanovoid formation in the shear bands. The pre-existing shear bands form weak links and are preferred sites for further deformation. Bhowmick et al. (*9*) attributed their results to the formation of nanovoids due to the coalescence of the excess free volume, which lowers the stress required for plastic

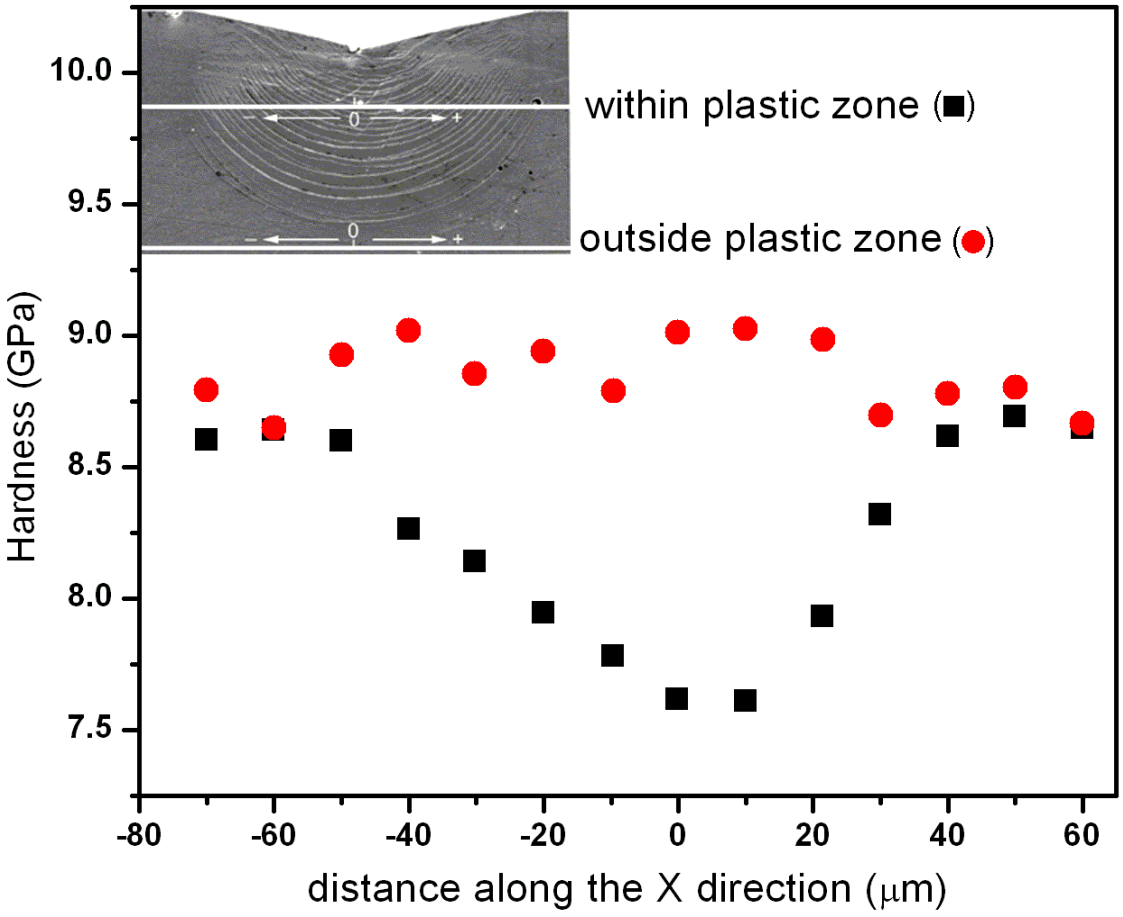

Figure 5-9. Hardness in the plastic zone is lower than that in the undeformed region.

deformation through shear bands. Yavari et al. (*11*), using in-situ X-ray diffraction, showed that free volume in deformed metallic glass ribbons is twice that in as-cast glass.

However, the experiments showing the role of softer shear bands in subsequent deformation are quite limited. Therefore, shear band morphologies underneath the indent in the 50% pre-strained sample were also examined, as shown in Fig. 5-10. The semi-circular shear bands within the plastic zone are irregular and convoluted, in contrast to the smooth semi-circular bands in the as-cast sample. Several shear bands, rather than following the semi-circular pattern, exhibit shapes similar to those of the compressive shear bands (i.e., the pre-existing shear bands) as shown in Fig. 5-2(b). As discussed before in the case of the Zr-based BMG, these shear bands can be assumed to be a mixture of the shear bands produced during the preceding compression [Fig. 5-3(b)] and those in the as-cast glass [Fig. 5-7(c)]. However, not all compressive shear bands reappear during subsequent indentation. It may be a result of competition between the pre-existing shear bands and newly generated shear bands. For clarity, we make the following definitions: τ_{r-0} is the critical resolved shear stress of undeformed glass; τ_{r-sb} is the critical resolved shear stress of the pre-existing shear bands; τ_0 is the maximum shear stress in undeformed glass; τ_{sb} is the shear stress in the pre-existing shear bands. The pre-existing shear bands are the weak links in the deformation (*12*), i.e., $\tau_{r-0} > \tau_{r-sb}$. However, as shown in previous publications *(7, 8)*, the maximum stress distribution underneath a Vickers indenter has a semi-circular shape, i.e., $\tau_0 > \tau_{sb}$. Shear bands appear only if the local shear stress exceeds the local resolved shear stress. As a result, in

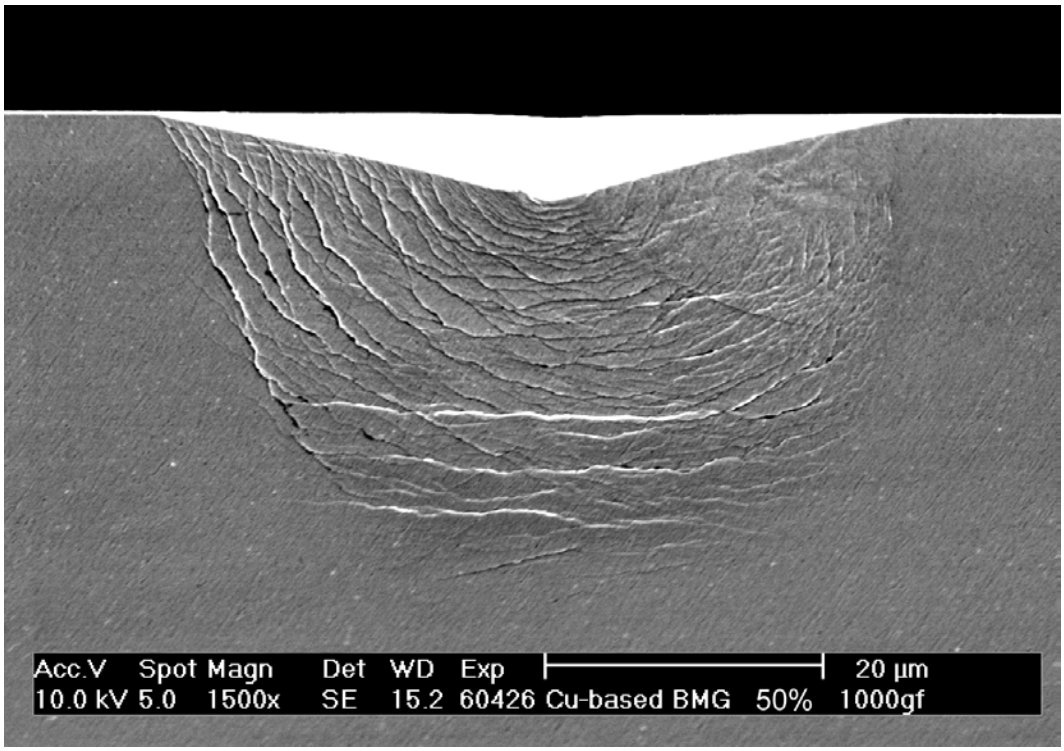

Figure 5-10. Shear band patterns underneath an indent at a maximum load of 1000g in the 50% pre-strained sample.

some regions whether $\tau_0 \geq \tau_{r-0}$, new shear bands are generated; whereas in other regions where $\tau_{sb} \geq \tau_{r-sb}$, the preexisting bands are reactivated. Both pre-existing and newly generated shear bands play a role in accommodating the subsequent indentation deformation.

5.5 Conclusions

In the constrained condition (samples with an aspect ratio of 2/3), a Cu-based metallic glass was compressed up to 70% plastic strain. A large number of shear bands were generated, whose density increases linearly with increasing plastic strain, i.e., $\rho = 0.14\varepsilon_p$. The increase in plastic strain corresponds to a systematic strain softening, i.e., $H = H_g - k_1\varepsilon_p$ $(k_1 > 0)$, in contrast to the strain hardening typically observed in crystalline metals. For comparison, plastic deformation was also obtained by micro-indentation. Underneath the micro-indent, semi-circular and radial shear bands were observed in the plastic zone, which can be explained by the expanding cavity model. The plastic zone exhibited a lower hardness than the undeformed zone, consistent with the strain softening observed in constrained compression.

In order to further investigate the role of pre-existing shear bands in subsequent deformation, shear band patterns underneath the indent in the 50% pre-strained glass were examined, which appeared to be a mixture of the shear bands produced during the constrained compression and those in the as-cast glass. Therefore, although the softer shear bands produced during the constrained compression acted as preferred sites for

subsequent deformation, newly generated shear bands also played an important role in accommodating plastic deformation.

References

1. H. Bei, S. Xie, E. P. George, *Phys. Rev. Lett.* **96**, 105503 (2006).
2. S. Xie, E. P. George, *to be submitted*.
3. A. L. Greer, I. T. Walker, *Mater. Sci. Forum* **386-388**, 77 (2002).
4. C. A. Schuh, T. G. Nieh, *Acta Mater.* **51**, 87 (2003).
5. W. J. Wright, R. Saha, W. D. Nix, *Mater. Trans. JIM* **42**, 42 (2001).
6. H. Zhang, X. Jing, G. Subhash, L. J. Kecskes, R. J. Dowding, *Acta Mater.* **53**, 3849-3859 (2005).
7. U. Ramamurty, S. Jana, Y. Kawamura, K. Chattopadhyay, *Acta Mater.* **53**, 705-717 (2005).
8. H. Zhang, X. Jing, G. Subhash, L. J. Kecskes, R. J. Dowding, in *Acta Mater.* (2005), vol. 53, pp. 3849-3859.
9. R. Bhowmick, R. Raghavan, K. Chattopadhyay, U. Ramamurty, in *Acta Mater.* (2006) pp. 2006.
10. W. H. Jiang, F. E. Pinkerton, M. Atzmon, in *Acta Mater.* (2005), vol. 53, pp. 3469-3477.
11. A. R. Yavari *et al.*, *Acta Mater.* **53**, 1611-1619 (2005).
12. C. A. Pampillo, *J. Mater. Sci.* **10**, 1194 (1975).

6 Response of a Zr-based metallic glass composite to constrained compression and indentation

6.1 Constrained compression induced shear bands and hardness change

A Zr-based composite, $(Zr_{70}Ni_{10}Cu_{20})_{82}Ta_8Al_{10}$, was compressed to 50% plastic strain without failure at room temperature at a strain rate of 1×10^{-3} s^{-1}. Figure 6-1(a-c) shows typical shear band patterns on free surfaces parallel to the loading direction at various plastic strains, revealing multiple shear bands generated after the constrained compression. For comparison, the amorphous matrix $(Zr_{70}Ni_{10}Cu_{20})_{90}Al_{10}$ was deformed to the same amount of plastic strain, and the corresponding shear band patterns are shown in Fig. 6-1(d-f). It is noted that shear band density increases with increasing plastic strain in both the composite and the single-phase BMG. However, the shear band density in the composite is much higher than that in the corresponding matrix (especially at low strains), indicating that the Ta particles act as nucleation sites for shear bands.

The shear band density, ρ, (defined as the number of shear bands per unit length along the compressive direction) in both the composite and the single phase glass were measured and expressed as a function of the plastic strain, as shown in Fig. 6-2. In both materials the shear band density increases linearly with plastic strain, i.e., the shear band spacing, d, (defined as the average distance between two nearest shear bands) decreases with increasing plastic strain:

$$\rho \approx A + 0.14\varepsilon_p, \text{ i.e., } d^{-1} \approx A + 0.14\varepsilon_p \qquad (6\text{-}1)$$

where A is the intercept on the axis of shear band density. It is interesting to note that the $\rho \sim \varepsilon$ relation for both the glassy matrix and the composite have similar slopes, but

different intercepts. Two factors contribute to the multiplication of shear bands in the composite: Ta particles and the mechanical constraint provided by the compression platens. In contrast, only the latter factor exists in the glassy matrix. This implies that Ta particles have no obvious effect on the slope when the plastic strain is higher than 10%, but play an important role in generating multiple shear bands at the start of deformation (< 10% plastic strain). In contrast, the mechanical constraint provided by the compression platen effectively activates the formation of shear bands over a wide plastic strain range and dominates the slope of $\rho \sim \varepsilon$ relation.

The achievement of severe plastic strain in otherwise brittle metallic glasses makes it possible for us to study the effect of plastic strain on their mechanical properties. In sections 3.1.3 and 5.1.2, it was known that the hardness of $Zr_{52.5}Al_{10}Ti_5Cu_{17.9}Ni_{14.6}$ and $Cu_{60}Zr_{30}Ti_{10}$ BMG decreases linearly with increasing plastic strain and decreasing shear band spacing. We now address the change in hardness of the composite with plastic strain. Nanoindentation was used to measure the hardness of the individual phases in the as-cast and 50% strained composite. Twenty-four nanoindentations were performed in an 8 x 3 array with indent spacings of 10 μm. By chance, several indents fell entirely within a Ta particle or in the glassy matrix, as shown in Fig. 6-3. The typical load-displacement (*P-h)* curves for the Ta phase in the undeformed and 50% strained composites are shown in Fig. 6-4. It is found that for a given maximum load (10 mN), the penetration in the Ta phase of the undeformed composite (about 375 nm) is slightly deeper than that in the 50% strained composite (about 310 nm), as shown in Fig. 6-4(a). The indenter impression in the Ta particle of the undeformed composite [Fig. 6-4(b)] is slightly larger

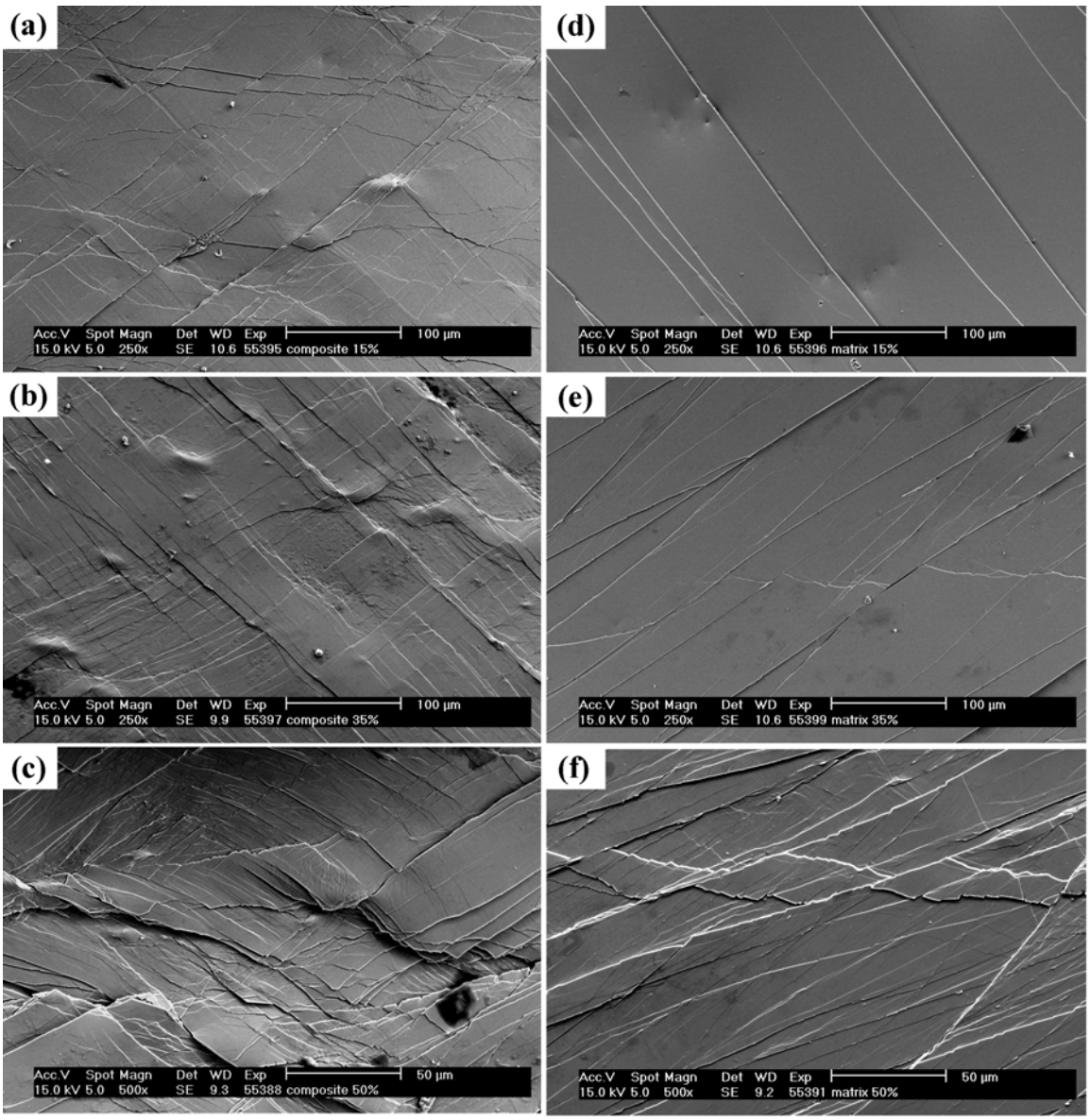

Figure 6-1. Typical shear band patterns in a BMG composite[$(Zr_{70}Ni_{10}Cu_{20})_{82}Ta_8Al_{10}$] (a), (b), (c), compared with those in a single-phase BMG with approximately the same composition as the matrix in the composite [$(Zr_{70}Ni_{10}Cu_{20})_{90}Al_{10}$] (d), (e), (f). (a) and (d) ε_p = 15%; (b) and (e) ε_p = 35 %, (c) and (f) ε_p = 50%.

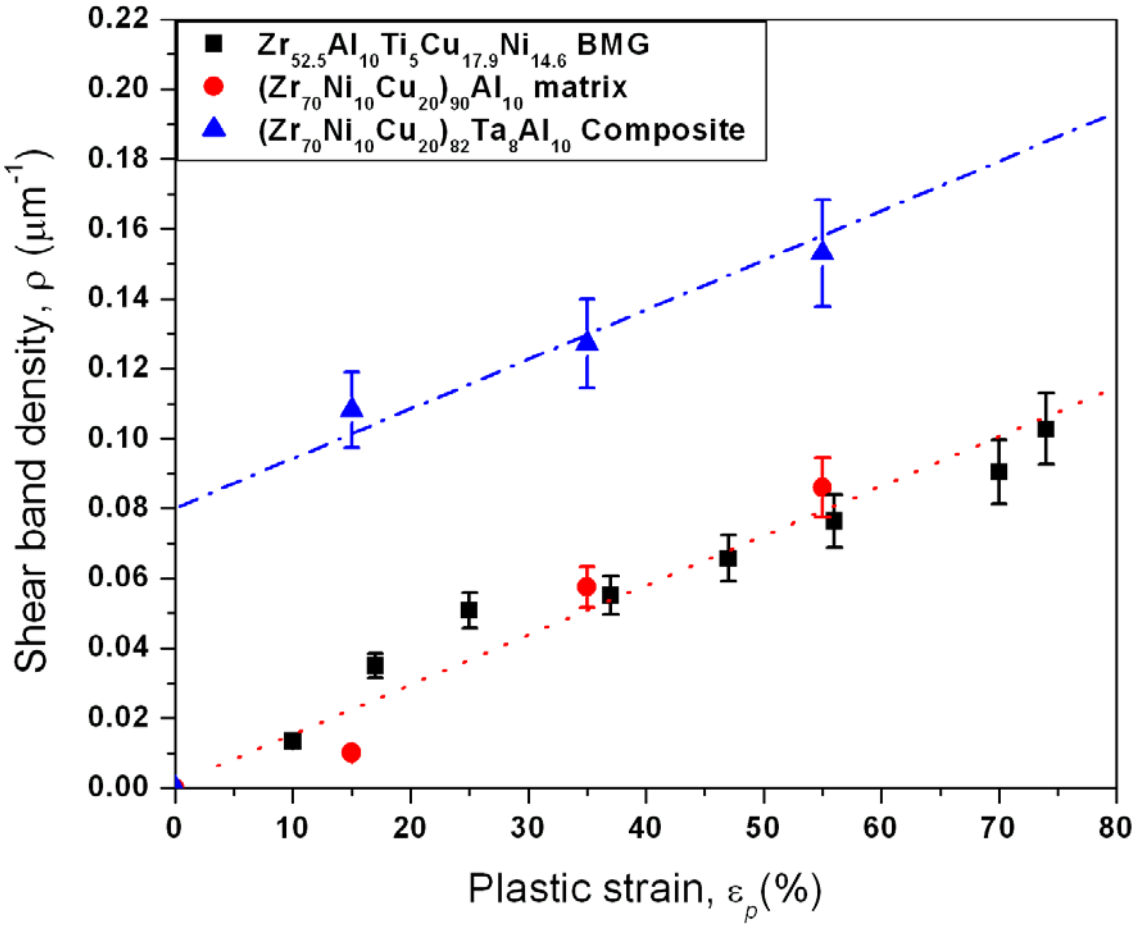

Figure 6-2. Shear band density linearly increases with increasing plastic strain in a metallic glass composite. For comparison, the relation between shear band density and plastic strain of the corresponding matrix and $Zr_{52.5}Al_{10}Ti_5Cu_{17.9}Ni_{14.6}$ BMG is included.

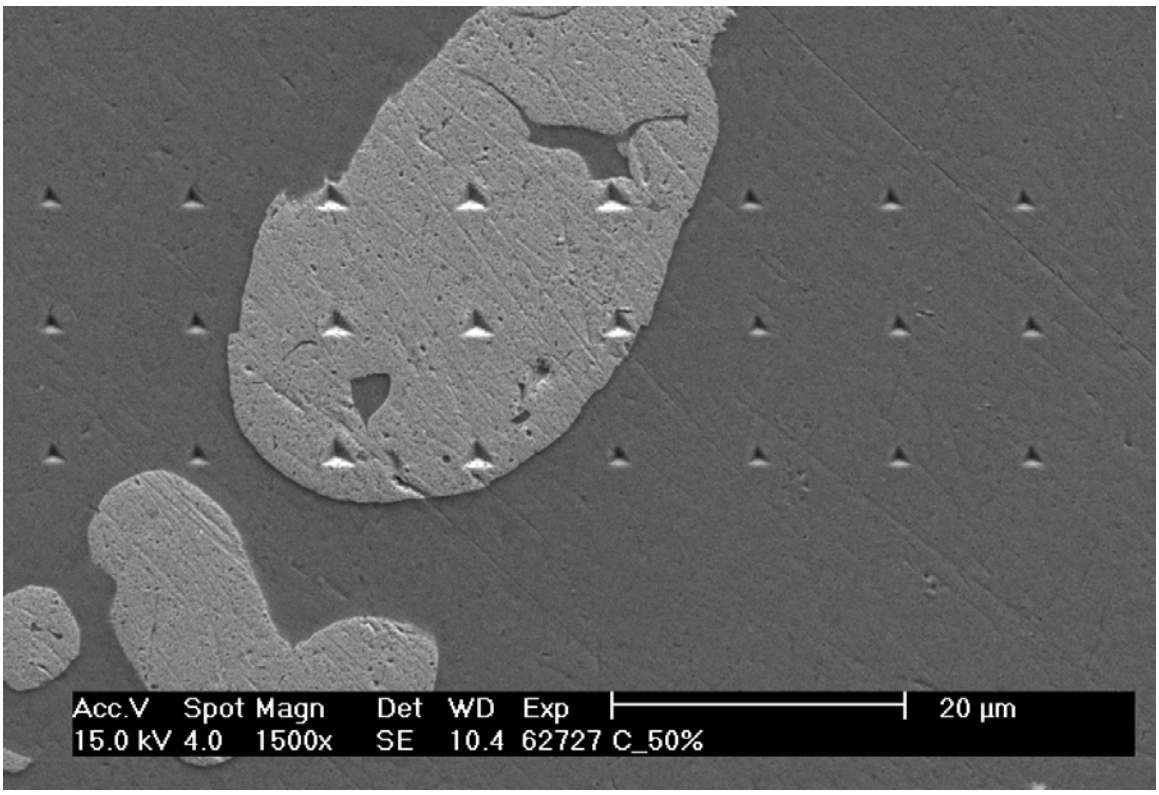

Figure 6-3. Micrographs of nanoindentation impressions in the composite, showing several indents fell entirely within the Ta particles or the glassy matrix.

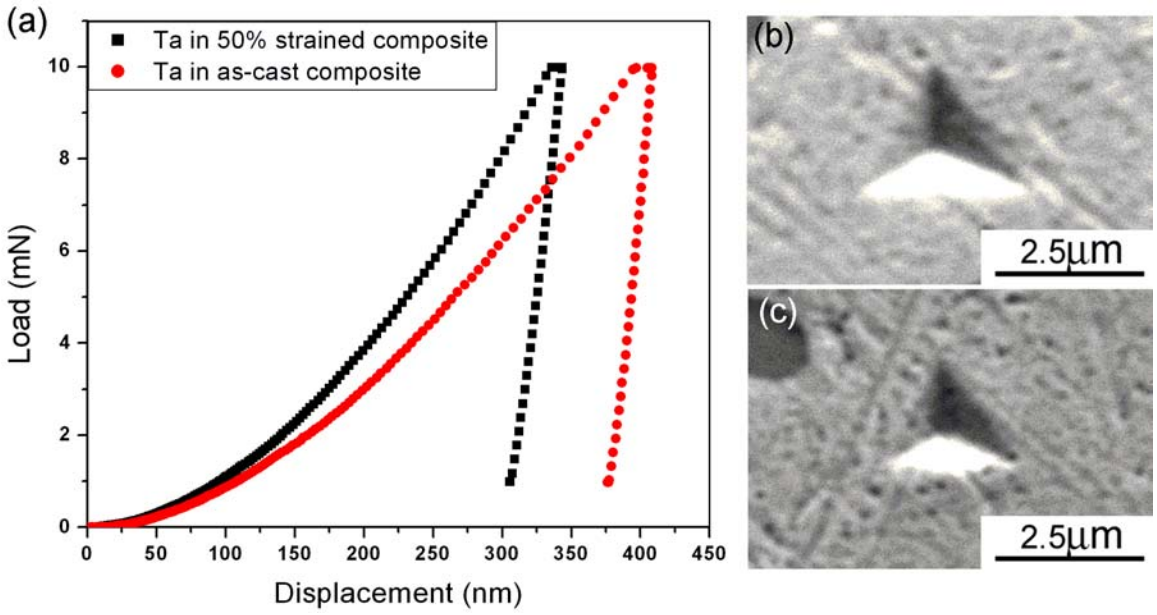

Figure 6-4. Hardness of the Ta phase in $(Zr_{70}Ni_{10}Cu_{20})_{82}Ta_8Al_{10}$ composite increases after plastic deformation: (a) typical load vs. displacement ($P \sim h$) curves, (b) indentation impression on Ta phase in the as-cast composite, and (c) indentation impression on Ta phase in the 50% strained composite.

than that in the 50% strained composite [Fig. 6-4(c)], which indicates that the Ta phase is harder in the 50% strained composite. The hardness values of the two phases before and after deformation were calculated from the unloading *P-h* curve using the Oliver-Pharr method (*1*) and are listed in Table 6-1. It is found that after 50% plastic strain in the composite, the hardness of the Ta particles increases from 2.74 GPa to 3.97 GPa, however, the hardness of glassy matrix decreases from 7.82 GPa to 7.55 GPa, which indicates strain hardening in the Ta particles and strain softening in the glassy matrix. The hardening of the Ta particles explains the work hardening observed in the engineering stress vs. strain curve of the composite (*2*).

Table 6-1. Hardness change of the individual phases in $(Zr_{70}Ni_{10}Cu_{20})_{82}Ta_8Al_{10}$ composite upon plastic deformation

	Hardness of Ta phase (GPa)	Hardness of BMG matrix (GPa)
As-cast ($\varepsilon_p = 0\%$)	**2.74 ± 0.24**	**7.82 ± 0.32**
Strained ($\varepsilon_p = 50\%$)	**3.97 ± 0.24**	**7.55 ± 0.42**

6.2 Indentation induced shear bands and hardness change

Figures 6-5(a) and (b) show typical shear band patterns underneath the indents in the composite and matrix, respectively, at a maximum load of 1000g, when the interface is parallel to the indenter diagonal. Two sets of shear bands (semi-circular and radial) were observed. Semi-circular shear bands have high density and, spread through the whole plastic zone (~ 40μm). Radial shear bands have relatively low density, intersect the semi-circular shear bands, and produce shear-offset steps on the semi-circular bands indicating that they formed later in the deformation process. This observation is similar to the shear band morphologies in $Zr_{52.5}Al_{10}Ti_5Cu_{17.9}Ni_{14.6}$ and $Cu_{60}Zr_{30}Ti_{10}$ BMG, discussed in sections 3.2.1.2 and 5.2.1. However, when comparing Fig. 6-5(a) with (b), it is noted that the shear band density in the composite is higher than that in the matrix, consistent with what was reported earlier for constrained compression (Fig. 6-2).

The higher magnification image of shear bands in the composite reveals that shear bands bypass the Ta particles, as shown in Fig. 6-5(c) and (d), and no new shear bands were observed around the Ta particles, in contrast to the samples subjected to the constrained compression where many shear bands were seen to be generated around the Ta particles [Fig. 6-1(a-c)]. This difference may be due to the existence of a non-rigid interface in the clamped interface technique, which makes the Ta particles near the interface flow into the interface rather than act as shear-band generating sources. However, the Ta particles located away from the interface (i.e., in the interior of the specimens) can activate the formation of new shear bands. Therefore, the composite generally exhibits higher shear band density than the corresponding matrix.

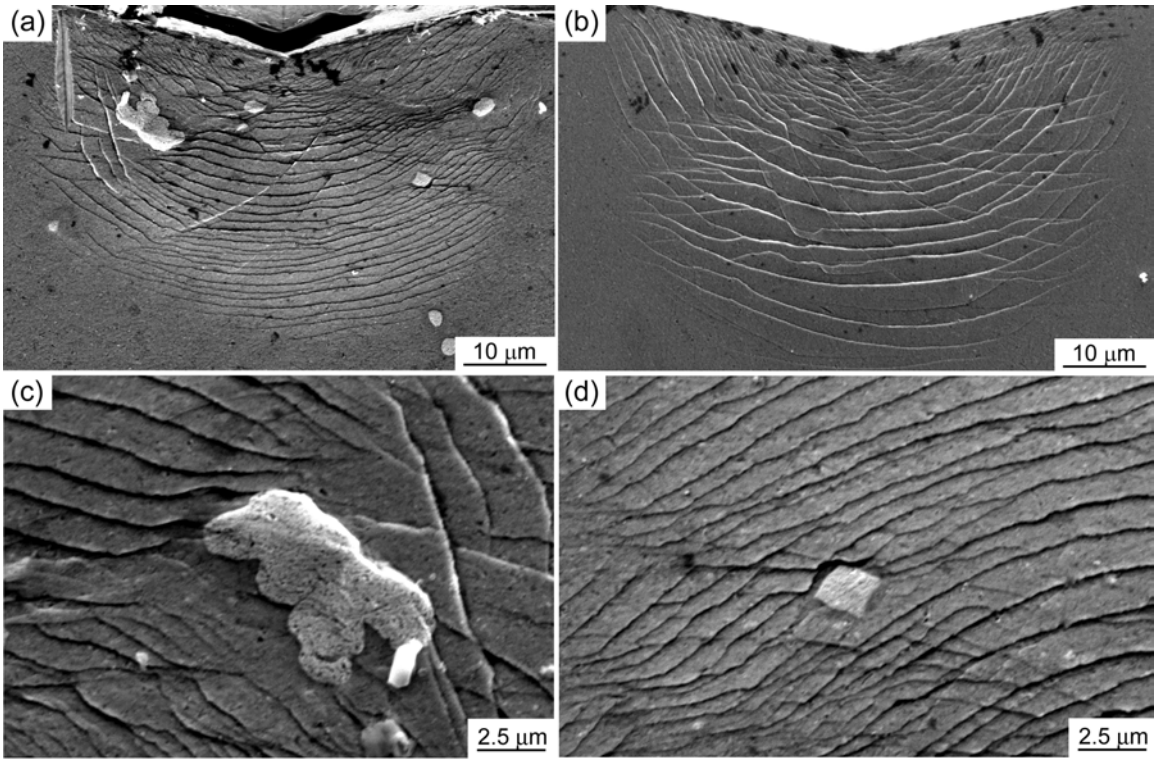

Figure 6-5. Shear band morphology underneath a Vickers indent in (a) Zr-based metallic glass composite $(Zr_{70}Ni_{10}Cu_{20})_{82}Ta_8Al_{10}$, and (b) glassy matrix $(Zr_{70}Ni_{10}Cu_{20})_{90}Al_{10}$. (c) and (d) are higher magnification images of (a) showing shear band morphology around Ta particles.

6.3 Conclusions

A Zr-based composite, $(Zr_{70}Ni_{10}Cu_{20})_{82}Ta_8Al_{10}$, was successfully compressed to 50% plastic strain without failure at room temperature, indicating that constrained compression is not limited to monolithic metallic glasses. Shear band density increases with increasing plastic strain in both composite and glassy matrix. At the same plastic strain, shear band density in the composite is much higher than that in the corresponding matrix, indicating that Ta particles act as nucleation sites for shear bands. Shear bands in the composite are a mixture of the shear bands produced due to Ta particles and mechanical constraint of the compression platen. After 50% plastic strain in the composite, the hardness of Ta particles increases from 2.74 GPa to 3.97 GPa, however, the hardness of the glassy matrix decreases from 7.82 GPa to 7.55 GPa, which indicates a strain-hardening effect in the Ta particles and a strain-softening effect in the glassy matrix.

Shear band density underneath the indents in the composite is also higher than in the corresponding matrix. Due to the existence of non-rigid interface in our experiments, Ta particles near the interface tend to flow into the interface rather than act as shear-band generating sources. Therefore, shear bands bypass Ta particles, and no new shear bands were observed around Ta particles.

References

1. W. C. Oliver, G. M. Pharr, *J. Mater. Res.* **7**, 1564 (1992).

2. C. Fan, R. T. Ott, T. C. Hufnagel, in *App. Phys. Lett.* (2002), vol. 81, pp. 1020.

7 Summary and future work

The present research was intended to provide a scientific understanding of plastic deformation in bulk metallic glasses and their composites at room temperature, and the effect of subsequent annealing on structure and mechanical properties of pre-strained metallic glasses.

A constrained compression method was employed to deform otherwise brittle bulk metallic glasses up to 80% plastic strain, which made it possible to systematically study plastic deformation behavior (i.e., shear band behavior) of bulk metallic glasses. Shear band density linearly increases with increasing plastic strain, i.e., shear band spacing is inversely proportional to plastic strain. A systematic strain-induced softening was observed in both Zr- and Cu-based metallic glasses, which contrasts sharply with the hardening typically observed in crystalline metals. Moreover, the strain softening was correlated with shear band patterns around/underneath a Vickers indent. Shear bands in the pre-strained glass were irregular and convoluted, and appeared to be a mixture of shear bands produced during the preceding compression and those in as-cast glass. This indicates that shear band regions are softer than the surrounding undeformed matrix and act as preferred sites for subsequent deformation during indentation, consistent with the macroscopic strain softening observed after plastic deformation.

Another method used to obtain plastic strain in bulk metallic glasses is micro-indentation, where the surrounding elastic region constrains the propagation of shear bands. Incomplete circular shear bands are formed on the top surface of a Vickers indent; and semi-circular and radial shear bands underneath a Vickers indent. The spacing of semi-circular shear bands linearly increases with increasing distance from the tip of the

indenter. Radial shear bands intersect semi-circular bands, resulting in shear offsets that decrease with increasing distance from the indenter tip. Nanoindentation results reveal that the hardness of the plastic zone is lower than that of the undeformed region; consistent with the strain softening observed in constrained compression.

The strain softening can be recovered after annealing, i.e., annealing makes the plastically strained metallic glasses harder, in sharp contrast to the annealing-induced softening typically observed in crystalline metals. During annealing, hardness initially recovers more rapidly in heavily deformed specimens than in lightly deformed ones, at a rate that varies inversely as the shear band spacing. With increasing annealing time and temperature, hardness further increases, at the same rate in all samples whether they are pre-strained or not. If the deformed and annealed metallic glass is plastically deformed again, reversible softening is observed. To our knowledge, this is the first time that such reversible softening in metallic glasses has been reported. These hardness changes were correlated with shear band patterns around and underneath a Vickers indent. Pile-ups and incomplete circular shear bands on the top surface recover after annealing. Shear bands produced during indentation in the deformed and annealed sample also tend to recover their originally semi-circular and radial shapes consistent with the hardness increase.

A Zr-based composite was successfully compressed to 50% plastic strain without failure at room temperature, indicating that constrained compression is not limited to monolithic metallic glasses. Shear band density in the composite also increases with increasing plastic strain. For a given plastic strain, shear band density in the composite is much higher than that in the matrix, indicating that Ta particles nucleate shear bands. Shear bands in the composite are a mixture of the shear bands produced by the Ta

particles and those due to the mechanical constraint of the compression platen. After 50% plastic strain in the composite, the hardness of the Ta particles increases from 2.74 GPa to 3.97 GPa, however, the hardness of the glassy matrix decreases from 7.82 GPa to 7.55 GPa, which indicates a strain-hardening effect in the Ta particles and a strain-softening effect in the glassy matrix.

Although profuse shear bands, resulting in strain softening, have been successfully obtained by constrained compression and indentation techniques, the atomic structure of the shear bands is still unknown. Therefore, further study on the microstructure of shear bands is required by advanced structure characterization techniques such as fluctuation TEM. The direct correlation between pop-in events and shear bands underneath an indent is still lacking due to the difficulties in observing shear bands underneath a nanoindent while collecting high-resolution load-displacement data during the tests.

VITA

Sujing Xie was born in Jiangxi, China on February 21, 1978. She entered the Department of Materials Science and Engineering at Nanchang University in 1995 and received her Bachelor degree in Materials Science and Engineering in 1999. In the same year, she entered the Master's program in Institute of Metal Research, Chinese Academy of Sciences, where she received her Master's degree in 2002. She came to the University of Tennessee and enrolled in the doctoral program in Materials Science and Engineering department in 2003. The Doctor of Philosophy degree was received in May 2007.